

# A Superthermal Ultra-Cold Neutron Source

Chen-Yu Liu

A DISSERTATION  
PRESENTED TO THE FACULTY  
OF PRINCETON UNIVERSITY  
IN CANDIDACY FOR THE DEGREE  
OF DOCTOR OF PHILOSOPHY  
  
RECOMMENDED FOR ACCEPTANCE  
BY THE DEPARTMENT OF  
PHYSICS

June 2002

© Copyright by Chen-Yu Liu, 2002.

All rights reserved.

# Abstract

Experiments with Ultra-Cold Neutrons (UCN) can offer an order-of-magnitude improvement in the precise measurement of neutron properties which are sensitive to physics beyond the standard model. These experiments, however, are limited by presently available UCN densities. This dissertation describes our efforts to understand and characterize the performance of cryogenic solids (solid deuterium and solid oxygen) as superthermal UCN sources, which may produce UCN densities much higher than what current facilities can provide.

The large neutron downscattering cross section via phonon creation in solid deuterium and the small nuclear absorption probability endow solid deuterium with the capability for intense UCN production via the superthermal process. The existence of the spin 1 deuterium molecules (para-D<sub>2</sub>), however, hinders full UCN yield. We mitigated this problem by implementing an ortho/para conversion apparatus. The para-D<sub>2</sub> fraction was reduced from 33.3% to  $1.4\% \pm 0.2\%$ . Raman spectroscopy was applied to perform a 0.2% measurement of the ortho-D<sub>2</sub> purity. A comprehensive set of measurements of the production and lifetime parameters found that the limiting dimension of a solid deuterium UCN source is half of the incoherent nuclear scattering length and also determined that the para-D<sub>2</sub> upscattering lifetime is roughly 1.4 ms. Both results are consistent with our theoretical calculations. With an UCN extracting and trapping method incorporating the timing scheme of a pulsed cold neutron spallation source, we have achieved the highest UCN density ( $98 \pm 5$  UCN/cm<sup>3</sup>) ever stored.

A novel UCN source using solid oxygen is also presented. The spin-wave excitations in

the anti-ferromagnetic  $\alpha$ -phase of solid oxygen provide neutrons with additional inelastic scattering channels; the electromagnetic coupling to the neutron magnetic moment predicts a large UCN production rate comparable with solid deuterium. Solid oxygen may be a better UCN source than solid deuterium.

We conclude by presenting an implementation of a UCN spin flipper using a bird cage resonator which will be useful for future polarized UCN experiments. Experimental tests with UCN measured a spin flip efficiency of  $\sim 99.6\%$ .

# Acknowledgements

First of all, I would like to thank my advisor, Albert Young, for his efforts in educating me to be an independent, responsible physicist. He offered me the utmost opportunities to broaden my scope. I especially thank Albert for not only his tolerance on my occasional fiasco, but more importantly for his efforts and encouragements in guiding me through.

Working with an experimental collaboration, I had the privilege to learn different skills from everyone: I was lucky to work closely with Steve Lamoreaux on the development of the ortho/para converter and monitor devices. He showed me how to think clearly and to be meticulous and innovative in my experimental work; I am greatly inspired by his persist, high quality research. I thank Chris Morris for the intuitive insights and the frantically hard-working attitude he has shown me; without Chris, the source development could have never produced fruitful results in such a short period of time. I thank Tom Bowles for his efforts in providing the resources, and I thank Sue Seestrom for her efforts in removing administrative obstacles. I thank Roger Hill for his efforts on our tedious simulations, and Gary Hogan for his expertise and serious attitude in maintaining the data acquisition system. I was fortunate to work closely with postdocs. They were Douglas Smith, Klaus Kirch, Andy Saunders and Axel Pichlmaier. Klaus Kirch is a living model, giving me the faith that it is possible to balance one's physics career with other aspects of life. I thank Andy Saunders for his relentless efforts on our experimental apparatus and for all the generous help he offered. As for the technician group I would like to thank Bill Teasdale, Mel Anaya and Russ Mortensen. I would also like to thank the Caltech group: Brad Filippone, Takeyasu Ito, Jeff Martin, Bryan Tipton and Junhau Yuan for their help. Our shifts together in the

counting houses were unforgettable experiences. I also thank Masahiro Hino; his optimistic views made me laugh during my dull single year in Los Alamos.

I thank Warren Griffith in showing me the Raman spectroscopy setup in the Princeton physics department. I thank Mark Makela and Bruce Vogelaar at Virginia Tech. Bruce's career advice was most enlightening. I also thank Peter Geltenbort for his generosity and the help he offered at essential moments.

I am extremely lucky to have Seth Hoedl as not only my fellow but also my best friend. We not only shared our puerile frivolity and princetonian snobbery but also carried each other through hardship during graduate school. I also want to acknowledge Seth for his tremendous efforts in helping editing this dissertation.

Finally, I would like to thank the physics department at Princeton University for the best support one can ever hope to obtain from graduate schools. In particular, I thank Joe Horvath for his patience and enthusiasm in solving every material preparation problem that came up. I thank John Washington for helping with the massive shipments we required between institutions. I thank Ted Griffith and Lazlo for their professional machining skill and advice.

# Contents

<b>Abstract</b>	<b>iii</b>
<b>Acknowledgements</b>	<b>v</b>
<b>1 Introduction</b>	<b>1</b>
1.1 Ultra-Cold Neutrons . . . . .	1
1.2 Motivation – Neutron Physics . . . . .	2
1.2.1 Neutron $\beta$ -decay . . . . .	3
1.2.2 Neutron Anti-neutron Oscillation . . . . .	6
1.2.3 The Neutron Electrical Dipole Moment . . . . .	7
1.3 UCN Sources . . . . .	9
<b>2 Theory of Superthermal UCN Source</b>	<b>11</b>
2.1 Conventional Sources . . . . .	11
2.2 Superthermal Principles for UCN Production . . . . .	13
2.2.1 Superfluid $^4\text{He}$ . . . . .	13
2.2.2 Incoherent Scattering and Pulsed Mode of UCN Production . . . . .	17
2.3 Neutron Scattering in Solid $\text{D}_2$ . . . . .	20
2.3.1 Anisotropy of the Solid Lattice . . . . .	20
2.3.2 The Incoherent Approximation . . . . .	22
2.3.3 Neutron Scattering from $\text{D}_2$ Molecules . . . . .	24
2.4 Comparison of the S- $\text{D}_2$ and superfluid $^4\text{He}$ . . . . .	26

<b>3</b>	<b>Ortho/Para-D<sub>2</sub> Conversion</b>	<b>29</b>
3.1	Motivation . . . . .	29
3.2	Ortho/Para-D <sub>2</sub> Physics . . . . .	30
3.3	Conversion of Para-D <sub>2</sub> into Ortho-D <sub>2</sub> . . . . .	32
3.3.1	Catalyzed Conversion . . . . .	32
3.3.2	Design of the Converter . . . . .	35
3.4	Measurement of the Ortho/Para-D <sub>2</sub> Ratio . . . . .	36
3.4.1	Raman Spectroscopy . . . . .	37
3.4.2	Thermal Conductivity Measurements – Hot Wire Method . . . . .	46
3.5	Discussions on the Converter Performance . . . . .	50
<b>4</b>	<b>The S-D<sub>2</sub> UCN Source Experiment</b>	<b>57</b>
4.1	Experimental Setup . . . . .	57
4.1.1	Cryostat Design . . . . .	57
4.1.2	Spallation Target . . . . .	59
4.1.3	Beryllium Neutron Flux Trap and Neutron Flux Amplifier . . . . .	60
4.1.4	Polyethylene Neutron Moderator . . . . .	60
4.1.5	Heat Load and Thermometry . . . . .	61
4.1.6	UCN Guide and Bottle . . . . .	61
4.1.7	UCN Detector and Data Acquisition System . . . . .	63
4.2	Data Analysis . . . . .	63
4.2.1	The Cold Neutron Spectrum . . . . .	63
4.2.2	The UCN Detection . . . . .	66
4.2.3	The Volume Dependence of UCN Production . . . . .	69
4.2.4	UCN Lifetime in Solid D <sub>2</sub> . . . . .	71
4.2.5	Stored UCN – World Record . . . . .	76
<b>5</b>	<b>Solid Oxygen as a Superthermal Source</b>	<b>81</b>
5.1	Introduction . . . . .	81



<i>CONTENTS</i>	ix
5.2 Neutron-Magnon Scattering Theory . . . . .	82
5.2.1 Magnetic Scattering Length . . . . .	82
5.2.2 Treatment of Coherent Scattering . . . . .	83
5.2.3 Anti-ferromagnetic Magnons . . . . .	85
5.2.4 Phonon Scattering . . . . .	91
5.3 Solid O <sub>2</sub> vs. Solid D <sub>2</sub> for UCN Production . . . . .	93
5.4 Experiment on UCN Production in S-O <sub>2</sub> . . . . .	96
<b>6 An UCN Spin Flipper</b>	<b>99</b>
6.1 Introduction – AFP Spin Flip . . . . .	99
6.2 The Bird cage Resonator . . . . .	101
6.2.1 Theory of the Resonator . . . . .	102
6.2.2 Fabrication of the Resonator . . . . .	103
6.2.3 The Field Profile . . . . .	105
6.2.4 Discussion . . . . .	107
6.3 UCN Spin Flip Experiment . . . . .	109
6.3.1 Experimental Setup . . . . .	109
6.3.2 Experimental Scheme and Procedure . . . . .	110
6.3.3 Analysis of the Spin Flip Efficiency . . . . .	112
6.3.4 Discussion . . . . .	114
<b>7 Conclusion</b>	<b>119</b>
7.1 Conclusions of This Work . . . . .	119
7.2 A Dedicated UCN Source for the “A” Measurement . . . . .	120
7.3 Other Superthermal Source Candidates . . . . .	121
<b>A Neutron scattering from D<sub>2</sub> Molecules</b>	<b>123</b>
<b>B Para-D<sub>2</sub> Neutron Upscattering</b>	<b>131</b>
<b>C The Incoherent Approximation</b>	<b>137</b>

<b>D Polyethelene Scattering Kernel</b>	<b>143</b>
D.1 Density of States in Polyethylene . . . . .	143
D.2 Comparison of the Scattering Kernel with Experimental Data . . . . .	146
D.3 Effect of Polyethylene Temperature on Cold Neutron Scattering . . . . .	147
<b>E Proton Source – LANSCE Proton Accelerator</b>	<b>153</b>
<b>F Bird Cage Field Profile</b>	<b>157</b>

# Chapter 1

## Introduction

### 1.1 Ultra-Cold Neutrons

Ultra-Cold Neutrons (UCN) are neutrons with kinetic energy smaller than the material potential (the effective Fermi potential), due to the short range strong nuclear force, which is often represented as an array of delta functions on the atomic scale, and whose strength is characterized by the nuclear scattering length,  $b$ , and the number density,  $\rho$ , of scatterers,

$$\overline{V} = \frac{2\pi\hbar^2}{m_n} \sum_i b_i \delta(r - r_i) = \frac{2\pi\hbar^2}{m_n} b_{coh} \rho. \quad (1.1)$$

This leads to a frequency dependent index of refraction,  $n_R$ , in the representation of the manifest wave property of very slow neutrons,

$$n_R = \sqrt{1 - \frac{4\pi b_{coh} \rho}{k_0^2}}. \quad (1.2)$$

As a result, UCN will experience total internal reflection because its index of refraction is smaller than unity, or in other words, the kinetic energy of the UCN is smaller than the material potential. The typical material potential for neutrons is a few hundred neV. This corresponds to UCN with temperatures cooler than  $\sim 4$  mK. In contrast to cold neutrons, UCN can thus be guided and stored in bottles. The novel properties of UCN permit new neutron physics experiments some of which are described below.

## 1.2 Motivation – Neutron Physics

The neutron was first discovered by Chadwick and Goldhaber[1] in 1932. Its charge is measured to be  $(-0.4 \pm 1.1) \times 10^{-21}$  e (effectively neutral) and it has a magnetic moment of  $-1.913\mu_N$ . Its intrinsic spin and parity are  $I(J^P) = \frac{1}{2}(\frac{1}{2}^+)$ . It consists of the lightest valence quarks  $udd$  and a sea of gluons and mesons. The net mass of neutron is 939.56 MeV. The free neutron decays into a proton, electron and anti-neutrino with a lifetime of  $886.7 \pm 1.9$  seconds[2]. Neutron  $\beta$ -decay is a mirror decay with in which its isospin  $I_z$  is changed by 1. The decay is an allowed transition (S-wave interaction) with no parity change, with no spin change between the parent( $n$ ) and daughter( $p$ ) nuclide. The neutron decay is described by a sum of the Fermi vector interaction (with spins of the decayed electron and neutrino anti-aligned) and the Gamow-Teller axial-vector interaction (with spins of electron and neutrino aligned). The ratio of Fermi to Gamow-Teller decay amplitude is  $0.467 \pm 0.003$ [3].

Despite their composite nature, neutrons provide experimentalists with a simple but intriguing system to study quantum chromodynamics and electroweak interactions. High precision measurements of physical observables in neutron systems provide a sensitive probe of physics beyond the Standard Model. Searches for physics beyond the Standard Model are motivated by an observational fact and a theoretical need: The cosmological observation of a large matter anti-matter asymmetry indicates that a fundamental process, which violates baryon number conservation and also breaks CP symmetry, took place in the baryogenesis phase of the universe. Such a process is built into the structure of the Standard Model but at too small a level to account for the observed remanet from the baryogenesis. Moreover, the Standard Model can not predict the mass of particles or the strength of different coupling constants; instead, it simply takes them as input parameters. A more encompassing theory which unifies the forces and generates the observed particle masses through mechanism like spontaneous symmetry breaking is needed.

The neutron has a relatively long lifetime and can be abundantly generated in reactors. Thus, neutron physics is a readily available, medium energy system that provides probes of

fundamental theory that complement those of high energy experiments. In the following, we give a brief overview of the three categories of neutron experiments: neutron  $\beta$ -decay measurements, neutron anti-neutron oscillation searches and the neutron electric dipole moment searches.

### 1.2.1 Neutron $\beta$ -decay

The formalism of neutron decay was first developed by Fermi[3] who used the most general Lorentz invariant Hamiltonian. This Hamiltonian has 20 free parameters: vector, axial-vector, scalar, pseudo-scalar, and tensor couplings for both left-handed and right-handed currents. These coupling constants can in general be complex numbers. The decay amplitude is a sum of left-handed and right-handed terms[15]:

$$\begin{aligned} M &= M_L + M_R \\ &= 2\frac{G_F}{\sqrt{2}} \sum_j L_j (\bar{\psi}_p \Gamma_j \psi_n) (\bar{u}_e \Gamma_j (1 - \gamma_5) v_\nu / 2) \\ &\quad + 2\frac{G_F}{\sqrt{2}} \sum_j R_j (\bar{\psi}_p \Gamma_j \psi_n) (\bar{u}_e \Gamma_j (1 + \gamma_5) v_\nu / 2). \end{aligned} \quad (1.3)$$

The  $j$  summation indices run over S, P, V, A and T, for scalar, pseudo-scalar, vector, axial-vector and tensor interactions, which have the following form:  $\Gamma_S = 1, \Gamma_P = \gamma_5, \Gamma_V = \gamma_\mu, \Gamma_A = i\gamma_\mu \gamma_5, \Gamma_T = i[\gamma_\mu, \gamma_\nu] / 2\sqrt{2}$ . A modern and rigorous formalism (Weinberg-Salam model) confirms Eq.(1.3) and relates the Fermi coupling constant,  $G_F$ , to the mass of the W gauge boson and the weak coupling constant,  $g$ :

$$\frac{G_F}{\sqrt{2}} = \frac{g^2}{8M_W^2}. \quad (1.4)$$

Based on experimental evidence to date, the standard model simplifies the above Hamiltonian to the pure left-handed V–A form. (Searches for physics beyond the standard model, however, attempt to measure additional coupling constants which we will come to later.) The leptonic current is simply  $\frac{1}{2}\bar{u}_e \gamma_\mu (1 - \gamma_5) v_\nu$ , while the hadronic sector has the following form (ignoring small, nuclear recoil order terms induced by the strong interactions.):

$$\frac{1}{2} \bar{\psi}_p \gamma_\mu (c_V + c_A \gamma_5) \psi_n. \quad (1.5)$$

Where  $c_V$  and  $c_A$  are the renormalizations of the relativistic wavefunctions considering the fact that neutron/proton are bound states of the fundamental objects of which they are composed – quarks[4]. We introduce  $g_V$  and  $g_A$  in terms of  $c_V$ ,  $c_A$ ,  $G_F$  and  $V_{ud}$ , the first element of the Cabibbo-Kabayashi-Maskawa (CKM) matrix[7], to parameterize the neutron decay:

$$g_V = c_V V_{ud} G_F \quad \text{and} \quad g_A = c_A V_{ud} G_F. \quad (1.6)$$

In this case, the coefficients in Eq.(1.3) are  $L_V = c_V V_{ud}$ ,  $L_A = c_A V_{ud}$  and  $L_{S,T} = R_{S,V,A,T} = 0$ .

Neglecting radiative corrections and pseudo-scalar couplings (only present for relativistic nucleons), Eq.(1.3) leads to a general decay probability distribution in terms of the neutron spin and lepton momenta [5]:

$$\begin{aligned} & \omega(\langle J \rangle | E_e, \Omega_e, \Omega_\nu) dE_e d\Omega_e d\Omega_\nu \\ &= \frac{1}{(2\pi)^5} p_e E_e (E^0 - E_e) dE_e d\Omega_e d\Omega_\nu \xi \left( 1 + a \frac{\mathbf{p}_e \cdot \mathbf{p}_\nu}{E_e E_\nu} + b \frac{m}{E_e} \right. \\ & \quad \left. + \frac{\langle \mathbf{J} \rangle}{J} \cdot \left[ A \frac{\mathbf{p}_e}{E_e} + B \frac{\mathbf{p}_\nu}{E_\nu} + D \frac{\mathbf{p}_e \times \mathbf{p}_\nu}{E_e E_\nu} \right] \right). \end{aligned} \quad (1.7)$$

Each of these coefficients is algebraically related to the coupling constants  $L_j$  and  $R_j$ . With a comprehensive set of measurements of the asymmetries and correlations between the observable vectors, one can extract the values of the fundamental coupling constants. These techniques provide a powerful way to test the V–A structure of the standard model. These experiments include the following:

- One can measure the neutron  $\beta$ -decay lifetime,

$$\tau = \left( m_e^5 \frac{G_F^2 \xi}{2\pi^3} f \bar{f}_b \right)^{-1}, \quad (1.8)$$

where  $\xi$  is the sum of the squares of the right-handed and left-handed coupling constants. By comparing the neutron lifetime with the muon lifetime, one can extract  $V_{ud}$ .

- By measuring the proton spectrum, one can extract the electron-neutrino correlation  $a$ .

- By measuring the  $\beta$  spectrum, one can extract the Fierz interference coefficient  $b$ .
- By measuring the angular correlation between the emitted electron and the neutron polarization, one can extract the parity violating coefficient  $A$ .
- By measuring the angular correlation between the recoil proton and the neutron polarization, one can extract the neutrino asymmetry coefficient  $B$ .
- By measuring the triple correlation between the electron momentum, proton momentum and the neutron spin, one can measure the time violating coefficient  $D$ .

Note that in the standard model  $b$  is zero unless scalar or tensor interactions are present and  $D$  is zero unless either the tensor coupling constant is complex and the scalar coupling constant is non-zero or the axial-vector coupling constant is complex<sup>1</sup>.

- In addition, an even more challenging measurement of the triple correlation of the electron momentum, electron polarization and neutron polarization allows one to extract the parity and time-reversal violating term  $R^2$ , which also probes the complex phase of the coupling constants.

If one assumes that the standard model is valid and ignores nuclear recoil order terms,

---

<sup>1</sup>There are also electromagnetic final state effects which provide a non-zero value for the  $D$  coefficient[4]. It thus puts a limit on the level to which one can probe the complex coupling constants in the Standard Model by measuring the  $D$  coefficient.

<sup>2</sup> $R$  does not appear in Eq.(1.7) because the polarizations of the electron are summed over. See Ref.[5] for the  $R$  term in the electron polarization dependent decay rate.

the lifetime and coefficients are reduced to[2]

$$\begin{aligned}
\tau^{-1} &= |V_{ud}|^2(1 + 3\lambda^2)1.89 \times 10^{-4} \text{sec}^{-1} (= 1/(886.7 \pm 1.9 \text{sec})) \\
a &= \frac{1 - \lambda^2}{1 + 3\lambda^3} (= -0.102 \pm 0.005) \\
b &= 0 \quad \quad \quad \because \text{No scalar and tensor couplings} \\
A &= -2 \frac{\lambda(\lambda + 1)}{1 + 3\lambda^2} (= -0.1162 \pm 0.0013) \\
B &= 2 \frac{\lambda(\lambda - 1)}{1 + 3\lambda^2} (= 0.984 \pm 0.004) \\
D &= R = 0 \quad \quad \because \text{No imaginary parts for the coupling constants.}
\end{aligned} \tag{1.9}$$

All of these depend only on a single parameter  $\lambda \equiv g_A/g_V (= -1.2670 \pm 0.0035)$ . In the parentheses are quoted the current experimental values. A set of measurements of the angular correlations provide an over-constrained determination of  $\lambda$  and can serve to test the standard model.

Note that  $V_{ud}$  can also be obtained from the  $ft$  values of the super-allowed  $0^+ \rightarrow 0^+$  nuclear decays (assuming the conserved vector current (CVC) hypothesis), however, it is  $2 \sigma$  lower than  $V_{ud}$  derived from the unitarity requirement of the three quark generation CKM matrix[2, 7]: The high precision unitary  $V_{ud} = \sqrt{(1 - V_{us}^2 - V_{ub}^2)}$  is derived from less precise measurements of small  $V_{us}$  from analysis of  $K^+ \rightarrow \pi^0 e^+ \nu$  and  $V_{ub}$  from analysis of  $B \rightarrow \pi(\rho) l \bar{\nu}$ . Combining the neutron lifetime and  $\lambda$  extracted from one of the angular correlation measurements, one can independently extract  $V_{ud}$  to test the validity of other values of  $V_{ud}$ . The neutron decay experiments, thus, offer a sensitive probe to extensions to the standard model.

Neutron experiments can potentially elucidate new physics such as the manifest left-right symmetric model which constructs the picture of right handed currents coupling through a right-handed higgs boson. It provides a framework for the understanding of the origin of parity violation in the weak interaction. Another mechanism to induce right-handed currents (even if the electroweak gauge group is the standard  $U(1) \otimes SU(2)$  group) is by



introducing exotic fermions<sup>3</sup> or leptoquarks.<sup>4</sup> Popular supersymmetric models introduce two higgs doublets which also cause scalar couplings in the neutron  $\beta$ -decay.[6]

The novel properties of UCN permit improved neutron  $\beta$ -decay experiments. A dominant source of systematic errors in previous cold neutron experiments is the difficulty of polarizing neutrons and precisely measuring the resultant polarization. The small kinetic energy of UCN allows a full polarization with a 6 Tesla magnetic filtering field. Moreover, UCN can be guided away from the production source, where the background radiation is high, into the experimental volume located in a well-shielded environment. Thus, UCN experiments operate with low radiation backgrounds.

### 1.2.2 Neutron Anti-neutron Oscillation

A positive observation of neutron( $n$ ) anti-neutron( $\bar{n}$ ) oscillations would give the experimental verification of baryon number non-conserving interactions that is needed to account for the observed matter anti-matter asymmetry. Whereas a negative result places limits on various candidate models[8]. It would also allow a test of the CPT theorem, which predicts that the mass of a particle is equal to the mass of its anti-particle[9].

Searches for  $n\bar{n}$  oscillations have been carried out with either neutrons confined in nuclei[12, 13] or free neutron beams[10, 14]. With nuclei, one looks for annihilation events induced by the appearance of a  $\bar{n}$  transformed from one of the constituent neutrons. However, this  $n\bar{n}$  oscillation rate is highly suppressed by the removal of the mass degeneracy in the nuclear field and the large destruction rate of anti-neutrons with normal nucleons. Experiments with free neutrons, on the other hand, provide direct measurement of such an oscillation. The figure of merit for such an experiment (termed “the discovery potential”) is the product of the neutron flux in the experiment,  $N_n$ , times the square of the averaged

---

<sup>3</sup>Exotic fermion involves a new representation of quarks and leptons whose right-handed components are in non-singlet representations of SU(2), and which mix with the usual quarks and leptons.

<sup>4</sup>Leptoquarks are bosons(S=0,1) coupling lepton-quark pairs. They can introduce a tensor coupling at the tree-level diagram when exchange of spin-zero leptoquarks is involved.

neutron time-of-flight,  $\bar{t}$ , through the experimental volume:

$$D.P. = N_n \cdot \bar{t}^2. \quad (1.10)$$

A long coherence time as well as a large neutron flux are essential for a good experiment. The current lower limit on  $n\bar{n}$  oscillation time is[2]

$$\tau_{n\bar{n}} > 1.2 \times 10^8 \text{ seconds} \quad \text{with CL=90\%,} \quad (1.11)$$

which is obtained from experiments of iron nuclei. Whereas, the lower limit put by a free neutron experiment is

$$\tau_{n\bar{n}} > 8.6 \times 10^7 \text{ seconds} \quad \text{with CL=90\%.} \quad (1.12)$$

### 1.2.3 The Neutron Electrical Dipole Moment

In a magnetic and an electric field, a non-degenerate particle with non-zero spin has a Hamiltonian with interacting terms

$$\boldsymbol{\mu} \cdot \boldsymbol{B} + \boldsymbol{d} \cdot \boldsymbol{E}. \quad (1.13)$$

Just as the magnetic field,  $\boldsymbol{B}$ , acts on the particle through the particle's intrinsic spin,  $\boldsymbol{S}$ , in the form of a magnetic moment,  $\boldsymbol{\mu} = g \frac{e}{2m} \boldsymbol{S}$ , the electrical dipole moment,  $\boldsymbol{d}$ , is introduced as another intrinsic property of the particle to quantify the effect of an external electric field. The electric dipole moment, however, must lie on the spin quantization axis, because it is the only vector allowed in this non-degenerate system. As a result, unlike the magnetic interaction term,  $\boldsymbol{\mu} \cdot \boldsymbol{B}$ , the electrical interaction term,  $\boldsymbol{d} \cdot \boldsymbol{E}$ , breaks both parity and time reversal symmetry. This implies CP violation through the CPT theorem. A search for the neutron electric dipole moment thus brings new evidence for CP violation.

The standard model has explicitly incorporated a CP violating phase in its CKM matrix and predicts a neutron EDM of  $10^{-32} \sim 10^{-31} \text{e}\cdot\text{cm}$ [16]. However, the level of time reversal asymmetry predicted in the standard model can not account for the observed matter anti-matter asymmetry[17]. Measurements of the electrical dipole moment of various particles

such as the electron, the quark and the neutron place stringent limits on models which attempt to explain the origin of CP violation. Such models include the induced CP-violating  $\theta$  term in QCD[18, 19] and spontaneous CP violation in the Higgs sector inherited from multiple complex Higgs doublets of supersymmetric models[16].

One method to measure the electric dipole moment of neutrons employs neutron resonance spectroscopy[20]: the neutron frequency shift between parallel and anti-parallel  $\mathbf{B}$  and  $\mathbf{E}$  field configurations gives a direct measure of the electric dipole moment. The uncertainty in the frequency measurement is converted into an uncertainty in the electric dipole moment,

$$\delta d = \frac{\hbar \delta f}{2E} = \frac{\hbar}{2ET}. \quad (1.14)$$

This leads to a figure of merit

$$M = \alpha \beta E T \sqrt{I}, \quad (1.15)$$

where  $\alpha$  is the enhancement factor characterizing the effect of a weak polarizing external field leading to an enormous internal field for cases of some interesting molecules, and as for free neutrons,  $\alpha = 1$ .  $\beta$  takes into account inefficiencies such as imperfect polarization and dead time associated with the electrical field reversal.  $T$  is the coherence time of the neutron free precession and  $I$  is the neutron current passing through the measurement apparatus (in a neutron beam experiment). The current upper limit on the electrical dipole moment of the neutron is[2]

$$d_n < 0.63 \times 10^{-25} \text{ e-cm}, \quad \text{with CL} = 90\%, \quad (1.16)$$

which is still consistent with time-reversal invariance and the standard model.

Compared with experiments using cold neutrons, the slow motion of UCN offers a long coherence time for both the neutron EDM and the  $n\bar{n}$  oscillation measurements[11].

The present UCN experiments are currently limited by available UCN densities. Thus, the construction of an intense UCN source is the first step towards new neutron experiments using UCN. One such experiment is a high precision measurement of the angular correlation “A” of neutron  $\beta$ -decay proposed by our collaboration. It is planned to be carried out at

the Los Alamos Neutron Science Center (LANSCE) in the coming year of 2003. The “A” characterizes the asymmetry of the electron emission direction with respect to the neutron polarization vector. An order of magnitude improvement in “A” can give a better insight to the unitarity test on the CKM matrix as mentioned in Sec 1.2.1. This high precision measurement of the electron asymmetry “A” motivates the work presented in this dissertation.

### 1.3 UCN Sources

The present UCN production facilities are reactor based. A large flux of neutrons with energies on the order of 10 MeV are emitted by the reactor core and then thermalized in a cold moderator to a mean energy of meV. UCN are present in the flux of thermal neutrons as a tiny fraction of the whole energy spectrum. The UCN flux can be further intensified by either vertical extraction[55] from the cold moderator which gravitationally red-shifts the cold neutron spectrum or by mechanical deceleration which uses a moving scatterer carrying away the neutron momentum. The UCN turbine source at the Institut Laue-Langevin (ILL)[56] incorporates both schemes and achieves a UCN density of 40 UCN/c.c. in a S.S. bottle placed immediately outside the source. These UCN production methods are based on the actions of conservative fields, under which the configuration space volume is invariant, and a compression in the neutron velocity space dilutes the neutron number density. This limits the UCN intensity produced by sources of this kind.

The superthermal UCN mechanism may produce a UCN density orders of magnitude greater than existing sources. It was first proposed in 1975 by Golub and Pendelbury[24]. In a superthermal source, a neutron dissipates its energy by exciting the collective modes of condensed matter under interaction. The excited quanta of the crystal/liquid field carry away the entropy of the neutron flux. In a single scattering regime, if the downscattering rate is much larger than the upscattering rate, then a large quantity of UCN can accumulate. In principle, the density is limited by either nuclear absorption time or the neutron  $\beta$ -decay lifetime, whichever is shorter. This idea was first pursued with superfluid  $^4\text{He}$ , and only

in the past few years have breakthroughs in experiments finally verified the theoretical predictions and also demonstrated its feasibility as an intense UCN source[28].

Materials other than  $^4\text{He}$  can very effectively downscatter cold neutrons into UCN, but are limited by their finite nuclear absorption probability. Solid deuterium is one such material[26]. To compensate for the short production time, first pointed out by Golub[25], a small volume of solid deuterium is coupled to a large inert storage volume. This trick prolongs the UCN lifetime in this system to scale linearly with the ratio of the storage volume to the source volume. Our work presents the first systematic study of solid deuterium as a superthermal source.

An operation of a solid deuterium UCN source with a pulsed neutron beam can potentially further increase the UCN yield by 2-3 orders of magnitude[21]. Most pulsed neutron beams are from spallation sources. The yield enhancement is made by the following: a neutron pulse produces the UCN and fills the UCN storage volume. At the conclusion of the pulse, the solid deuterium is valved off from the storage volume. The heat on the spallation target can be removed when the beam is off, and thus, a higher peak current is possible. In addition, experiments with the stored UCN can be performed while the beam is off, hence, eliminating the continuous high backgrounds due to gammas associated with neutron production, which most of the reactor based experiments suffer.

## Chapter 2

# Theory of Superthermal UCN Source

Operated in single scattering mode, neutron moderators can produce and accumulate a large population of milli-Kelvin UCN in an environment of several Kelvin. The key is to prevent neutrons from thermally equalizing with the moderator and to suppress other neutron loss mechanisms as well. This “superthermal” process is predicted to give orders of magnitude in enhancement of the UCN density over what can be achieved by conventional schemes of neutron cooling through thermalization. We are particularly interested in the use of solid deuterium as an intense UCN source. The reasons for choosing solid deuterium over the better-understood superfluid helium are addressed, and comparisons of their performances are presented. Solid deuterium is more complicated to understand than superfluid  $^4\text{He}$ . The theoretical issues are: incoherent versus coherent scattering processes, the effect of the anisotropic dispersion relation in the solid lattice and the spin-dependent couplings to the ortho- and para- $\text{D}_2$  species.

## 2.1 Conventional Sources

Fast neutrons are abundantly produced from fission reactors and from high energy proton accelerators via nuclear reactions or spallation production. These neutrons have energies on the order of 10 MeV. They can be effectively moderated with elastic scattering in hydrogen-rich materials, where a neutron dissipates its energy through multiple collisions with the protons and comes to thermal equilibrium after approximately 10 to 20 collisions.<sup>1</sup> Their resultant energy spectrum is described by the Maxwell-Boltzmann distribution,

$$\Phi(E)dE = \Phi_0 \frac{E}{(k_B T)^2} e^{-E/k_B T} dE, \quad (2.1)$$

where  $\Phi_0$  denotes the total integrated flux. UCN are produced in the low energy tail of the thermal spectrum of the moderator with UCN energies ranging from zero to the potential energy of the surrounding material wall (335 neV for  $^{58}\text{Ni}$ , for other material see Sec 4.1.6). The integrated number of UCN increases as the temperature of the moderator decreases. The dependence of the ultimate UCN density on the moderator temperature,  $T$ , assuming a complete thermalization of the fast neutron is

$$\begin{aligned} \rho_{ucn} = \int_0^{E_{ucn}} \frac{\Phi(E)}{v} dE &= \int_0^{v_{ucn}} \frac{2\Phi_0}{\alpha} \frac{v^2}{\alpha^2} e^{-v^2/\alpha^2} \frac{dv}{\alpha} \\ &\cong \int_0^{v_{ucn}} \frac{2\Phi_0}{\alpha} \frac{v^2}{\alpha^2} (1 - O((v/\alpha)^2)) \frac{dv}{\alpha} \end{aligned} \quad (2.2)$$

$$= \begin{cases} \frac{2}{3} \frac{\Phi_0}{\alpha} \left(\frac{E_{ucn}}{k_B T}\right)^{3/2} & \propto 1/T^2 & \text{for constant } \Phi_0 \\ \frac{\bar{\rho}}{3\sqrt{\pi}} \left(\frac{E_{ucn}}{k_B T}\right)^{3/2} & \propto 1/T^{3/2} & \text{for constant } \bar{\rho}. \end{cases} \quad (2.3)$$

where  $E$  is the the neutron energy,  $v$  is the neutron velocity, and  $\alpha = \sqrt{2k_B T/m_n}$  is the mean thermal velocity. The employment of the above Taylor expansion is justified because the UCN velocity,  $v_{ucn}$ , is much smaller than the thermal velocity,  $\alpha$ .

Inside moderators, neutrons experience elastic diffusion (random walk) as well as inelastic energy dissipation. If neutrons have a short diffusion length, then the incident flux is

---

<sup>1</sup>A thermal moderator provides the first stage of neutron cooling. The spallation neutron momentum is transferred to the scatterer in the moderator through elastic scattering. Internal excitations of the scatterer are negligible in this case. Scatterers with a matching mass to a neutron offers the most efficient cooling.

quickly re-distributed to a uniform density,  $\bar{\rho}$ , throughout the moderator; if the diffusion length is long, then the flux,  $\Phi_0$ , is approximately invariant throughout the moderator. Neglecting sources of neutron loss for both cases, the ultimate UCN density is a power law function of the moderator temperature (Eq.(2.3))[22]. A room temperature moderator can produce one UCN for every  $10^8$  moderated neutrons; A 30K moderator can produce one UCN for every  $10^6$  moderated neutrons. (30K is the lower operating limit of polyethylene, see appendix D). However, the numbers quoted only holds in a very ideal situation which neglects sources of neutron loss; any nuclear absorption will preferentially eat up the low energy neutrons, distorting the energy spectrum and resulting in a much smaller yield of UCN.

## 2.2 Superthermal Principles for UCN Production

If one illuminates a sample of atoms with intense laser light, ground state electrons can be excited to a meta-stable state by absorbing a light quantum (photon), whose energy supplies the transition energy of this meta-stable state. If the spontaneous decay of this meta-stable state through the emission of a photon has a small rate, then there is a population inversion, which results in a large number of electrons in the meta-stable state. Analogously, the superthermal mechanism induces a population inversion of neutrons, with the phonons which propagate in the moderator playing the role of the photons in the atomic system. In this case, cold neutrons are downscattered into a meta-stable low energy state (the ultra-cold state), by creating a phonon whose energy and momentum matches the energy and momentum transfer of the interacting neutron. If the loss from upscattering by absorbing a phonon has a small rate, then there is a population inversion, which results in a large quantity of UCN. Thus, UCN are produced in a single scattering event, in contrast to a thermal neutron moderator which cools neutrons by multiple scattering. In the course of the superthermal process, thermal equilibrium has not yet been established between the neutron energy states. A long thermalization time (a long upscattering time for UCN) is exactly the key to make it possible to exploit this strong inequilibrium and collect a large



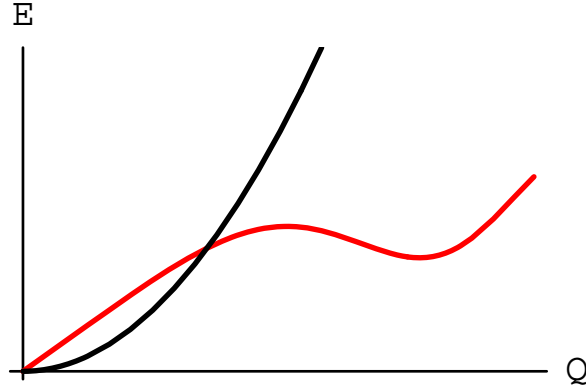


Figure 2.1: Dispersion curves of free neutrons (black curve) and the superfluid  $^4\text{He}$  (red curve). The intersecting point  $(Q, E)$  of these two curves sets the condition for inelastic one phonon neutron scattering for UCN production.

population of meta-stable particles.

### 2.2.1 Superfluid $^4\text{He}$

In 1972 Golub [23] first proposed to make superfluid  $^4\text{He}$  into a superthermal UCN source.  $^4\text{He}$  has a zero nuclear absorption probability, and thus, the UCN lifetime inside the material can be as long as the  $\beta$ -decay lifetime. It is a nuclear spin singlet ( $S = 0$ ), and thus, is a pure coherent neutron scatterer. Therefore, in the scattering process which produces UCN, a coherently created phonon carries away both the energy and the momentum of the incident neutron. Phonons in superfluid  $^4\text{He}$  are the low energy Feynmann-Landau solutions to the collective excitation. They are the eigenmodes of the translational degrees of freedom, and their dispersion relation is linear in the small momentum limit. The intersection of the neutron and phonon dispersion curves (as illustrated in Fig.2.1) shows that only 11 K neutrons can find a phonon mode with matching energy and momentum for the UCN production. Note that it is only this same phonon mode which can upscatter UCN. Figure 2.2 illustrates that only a tiny band of cold neutrons, with energy centered at 11K (9meV) and wavelength centered at  $7 \text{ \AA}$ , become UCN. The energy bandwidth of the cold neutrons

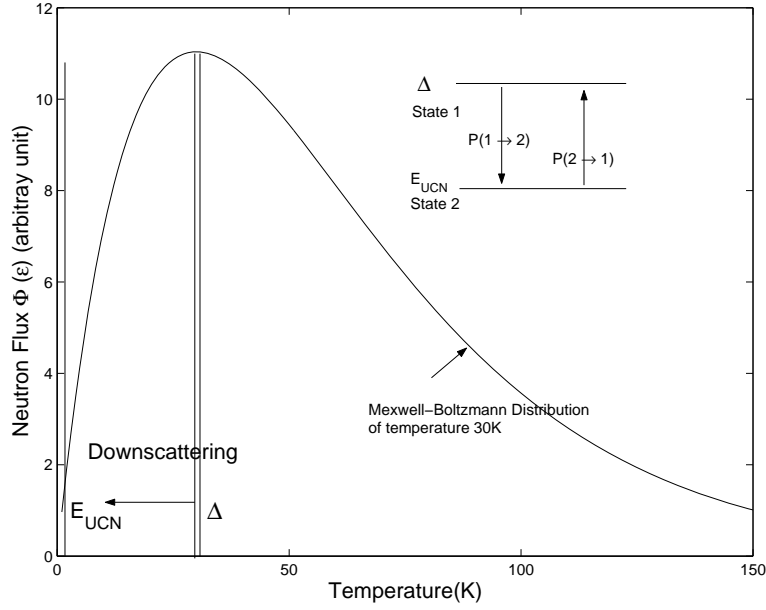


Figure 2.2: The Maxwell-Boltzmann energy distribution of 30K neutrons. This depicts the fact that only a narrow window in the energy spectrum is open for UCN production. The inset illustrates the energy transitions in the two-state model which describes the coherent superthermal UCN source, i.e., superfluid  $^4\text{He}$ .

is the maximum energy of UCN, i.e., 335 neV.

The UCN production in superfluid  $^4\text{He}$  is modeled by a two-state transition[92] (illustrated in the inset of figure 2.2). The transitions associated with UCN are between the state 1 (cold neutron state) with energy  $\Delta = 11\text{K}$  and state 2 (UCN state) with energy  $E_{ucn}$ . The change rate of the UCN number density, is the production rate,  $P(1 \rightarrow 2)$  minus the loss rate  $P(2 \rightarrow 1)$ :

$$\begin{aligned}\dot{\rho}_2 &= P(1 \rightarrow 2) - P(2 \rightarrow 1) \\ &= N\sigma(1 \rightarrow 2)\phi_1 - N\sigma(2 \rightarrow 1)v_2\rho_2.\end{aligned}\tag{2.4}$$

With a constant supply of cold neutrons, the downscattering rate is the incident neutron flux with energy  $\Delta$ ,  $\phi_1$ , times the transition cross section,  $\sigma(1 \rightarrow 2)$ , and the upscattering rate is the UCN flux,  $v_2\rho_2$ , times the upscattering cross section,  $\sigma(2 \rightarrow 1)$ . Here  $N$  is the

density of scatterers. Solving this differential equation gives the time evolution of UCN density:

$$\rho_2(t) = \frac{\phi_1 \sigma(1 \rightarrow 2)}{v_2 \sigma(2 \rightarrow 1)} \{1 - e^{-v_2 N \sigma(2 \rightarrow 1)t}\}. \quad (2.5)$$

The saturation density is thus a product of the UCN production rate,  $P$ , and the time of production,  $\tau$ , which is determined by the mean lifetime of UCN in state 1:

$$\rho_2 = P \times \tau = (\phi(1) N \sigma(1 \rightarrow 2)) \times \left( \frac{1}{v_2 N \sigma(2 \rightarrow 1)} \right). \quad (2.6)$$

Ignoring other loss mechanisms, the ultimate UCN density, therefore, scales with the ratio of the downscattering cross section to the upscattering cross section.

Even though this cross section ratio can be derived by the detailed balance condition between micro-states as discussed in Ref.[92], we take a direct approach by introducing the explicit formalism of the inelastic differential cross section, depicting neutron scattering from lattices involving one phonon exchange[33]:

$$\begin{aligned} \left( \frac{d^2 \sigma}{d\Omega dE'} \right)_{coherent}^{\pm 1 \text{ phonon}} &= \frac{N \sigma_c}{8\pi M} \frac{k'}{k} e^{-2W(\kappa)} \times \\ &\sum_j \frac{|\kappa \cdot \sigma^j(\mathbf{q})|^2}{\omega_j(\mathbf{q})} \delta(\omega \mp \omega_j(\mathbf{q})) \delta(\kappa \mp \mathbf{q} + \tau) \left\{ \mathbf{n}(\mathbf{q}) + \frac{1}{2} \pm \frac{1}{2} \right\}, \end{aligned} \quad (2.7)$$

where “+” designates single phonon creation, i.e., neutron downscattering; and “−” designates phonon annihilation, i.e., UCN upscattering. The absolute differences between these two are the weighting on the phonon occupation number,  $n(q)$ , and the kinematic dependence on the scattering phase space,  $k'/k$ . The other factors are the even functions of the momentum transfer, and are thus the same for both the creation and annihilation processes. The ratio of the downscattering to the upscattering cross section is thus,

$$\frac{\sigma^{+1 \text{ phonon}}}{\sigma^{-1 \text{ phonon}}} = \frac{\left( \frac{k_{ucn}}{k_\Delta} \right)}{\left( \frac{k_\Delta}{k_{ucn}} \right)} \left( \frac{1 + n(\Delta)}{n(\Delta)} \right) = \frac{E_{ucn}}{\Delta} e^{\Delta/k_B T}, \quad (2.8)$$

where Bose-Einstein statistics,  $n(\Delta) = 1/(e^{\Delta/k_B T} - 1)$ , are used for the phonons. Thus, we conclude that the UCN density increases exponentially as the temperature of the moderator decreases:

$$\rho_{ucn} = \frac{\phi_1}{v_{ucn}} \frac{E_{ucn}}{\Delta} e^{\Delta/k_B T}. \quad (2.9)$$

A few insights emerges from the knowledge that the phonon occupation number  $n$  is usually much smaller than unity at the temperature of operation: The neutron downscattering rate, which depends on the availability of the modes of excitation through  $(1+n) \sim 1$ , demonstrates a weak dependence on the phonon occupation number. The strength of up-scattering, on the other hand, directly scales with the number of phonons physically present. The number of phonons, and thus the upscattering rate, can be exponentially suppressed by the Boltzmann factor. This is the origin of the exponential gain in UCN density.

In superfluid  $^4\text{He}$ , the above superthermal performance stops at 0.7 K, below which the simple two state model does not hold because another upscattering mechanism starts to dominate the UCN loss: UCN can scatter with a phonon and absorb a fraction of the phonon energy instead of absorbing the full phonon energy[92]. At this temperature, the estimated UCN density with a constant 30K neutron flux is:

$$\begin{aligned}\rho_{ucn} &= \frac{\Phi_0}{v_{ucn}} \frac{\Delta E_{ucn}}{(k_B T_0)^2} e^{-\Delta/k_B T_0} \left( \frac{E_{ucn}}{\Delta} e^{\Delta/k_B T_m} \right) \\ &= 1.2 \times 10^{-4} \times \Phi_0.\end{aligned}\tag{2.10}$$

This is a significantly higher UCN yield than that seen from a thermal moderator source.

### 2.2.2 Incoherent Scattering and Pulsed Mode of UCN Production

The scattering cross section is proportional to the square of the matrix element (first Born approximation):

$$|\langle \phi_f | V | \phi_i \rangle|^2.\tag{2.11}$$

For neutron scattering from condensed matter, the interaction potential,  $V$ , is a sum of local potential of each scatterer with the scattering length,  $b_l$ , characterizing the scattering strength. The averaged scattering amplitude is proportional to

$$\begin{aligned}\sum_{l,l'} \overline{b_l^* b_l} &= \sum_{l,l'} |\bar{b}|^2 + N \sum_l (\overline{|b|^2} - |\bar{b}|^2) = \sum_{l,l'} |\bar{b}|^2 + N \sum_l \overline{(|b| - \bar{b})^2} \\ &= \sum_{l,l'} b_{coh}^2 + \sum_l b_{inc}^2\end{aligned}\tag{2.12}$$

where the relation  $\overline{b_l^* b_l} = |\bar{b}|^2 + \delta_{l,l'}(|\bar{b}|^2 - |\bar{b}|^2)$  is used. The scattering amplitude is thus separated into a “square of the sum” plus a “sum of the squares”. Neutron matter waves span over space, and scattered amplitudes from different points in space interfere according to the phase shift from different propagating distances. As a result, this “square of the sum (of the average)” causes coherent scattering from the average properties of the scattering sites. Local deviations, such as isotope, spin and even crystal defects (for example, vacancies), on the other hand, induce force fields; neutrons are scattered from this deviation from average. This leads to incoherent scattering.

Most nuclei have a significant incoherent scattering length. The incoherent part of the scattering results from deviations from the mean in the nuclear spin and isotopic mass. The random fluctuations introduce an additional scattering amplitude for which the total momentum of the scattered particles no longer inherits the initial neutron momentum, but instead the crystal as a whole compensates for the missing momentum. As a result, all neutrons with energies smaller than the Debye temperature can find a corresponding phonon mode for a total energy transfer (see figure 2.5). This significantly increases the fraction of neutrons that participate in the downscattering and contribute to the UCN production. At the same time, the upscattering probability is also enhanced as UCN can be upscattered into final states with a broad range of energies.

We can generalize the two-level model by introducing a third energy state which represents the ensemble of states in the ultimate thermal equilibrium. Cold neutrons are downscattered instantly into the UCN state, and then instead of making transitions back to the initial state, most of the UCN are brought into the third state, approaching the ultimate equilibrium. Given a single pulse of cold neutrons at time zero, the time evolution of the neutron populations of the initial cold neutron state, the intermediate UCN state, and the final thermal state are illustrated in Fig.2.3. We are interested in the UCN density evolution, which is

$$\begin{aligned} \rho_2(t) &= \frac{v_1 \sigma(1 \rightarrow 2) \rho_1(0)}{v_1 \sigma(1 \rightarrow 2) - v_2 \sigma(2 \rightarrow 3)} \{e^{-v_2 N \sigma(2 \rightarrow 3)t} - e^{-v_1 N \sigma(1 \rightarrow 2)t}\} \\ &\cong \rho_1(0) \{e^{-v_2 N \sigma(2 \rightarrow 3)t} - e^{-v_1 N \sigma(1 \rightarrow 2)t}\} \quad \text{for downscatter} \gg \text{upscatter.} \end{aligned} \quad (2.13)$$

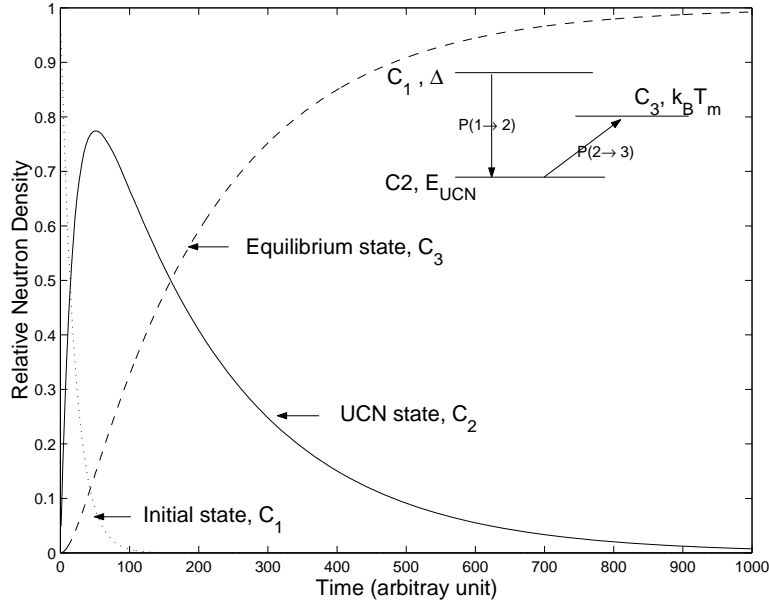


Figure 2.3: Time evolution of the states in the modified three-state model. The inset illustrates the transitions between the initial cold neutron state, UCN state and the thermal-equilibrium state.

The UCN density  $\rho_2$  increases exponentially from zero with a rate of  $v_1 N \sigma(1 \rightarrow 2)$ , and comes to a peak value of  $\sim \rho_1(0)e^{-1}$  at time

$$\frac{\ln(v_1 \sigma(1 \rightarrow 2)/v_2 \sigma(2 \rightarrow 3))}{v_1 N \sigma(1 \rightarrow 2) - v_2 N \sigma(2 \rightarrow 3)}, \quad (2.14)$$

right before the upscattering time  $1/(v_2 N \sigma(2 \rightarrow 3))$ , and then decays exponentially with a rate of  $v_1 N \sigma(1 \rightarrow 2)$ . If the design of a UCN source is such that UCN can diffuse out into a storage volume in a time shorter than the upscattering time, then the UCN yield is maximized. The above text describes the UCN production scheme in pulsed mode.

In most cases, one should also include all the loss mechanisms in addition to the UCN upscattering loss considered above. The most common source of neutron loss is the nuclear absorption in the material itself. This intrinsic property often puts the limit on the UCN lifetime in the source, whereas other source of loss can be experimentally varied and reduced, for example, the upscattering can be reduced by lowering the source temperature; the

isotope nuclear absorption can be reduced by purification.

After realizing these principles of operation, one can identify a few guidelines for choosing materials to construct a superthermal source:

- The source material should have a large bound nuclei cross section to maximize the UCN production rate.
- It should also have a very low absorption cross section to increase the UCN residence time in the source.
- Light elements are favored, because the strength of neutron coupling to the phonon field depends on the degree of nuclear recoil in the scattering events.
- The phonon density of states should greatly overlap with the cold neutron spectrum, in order to enhance the probability of downscattering.

Solid deuterium is a promising candidate that meets the above criteria.

### 2.3 Neutron Scattering in Solid D<sub>2</sub>

To investigate S-D<sub>2</sub> as a superthermal UCN source, we must first understand the neutron scattering from this material. The deuteron(D) has a nuclear spin of one. When neutrons interact with this nucleus, the neutron-deuteron wavefunction ( $S = \frac{1}{2} + \vec{1}$ ) can be decomposed into singlet ( $S = \frac{1}{2}$ ) and triplet ( $S = \frac{3}{2}$ ) channels, resulting in two different scattering modes. The average strength of these scattering modes gives a coherent scattering length,  $b_{coh}$ , of

$$\frac{2 \times \frac{1}{2} + 1}{(2 \times \frac{1}{2} + 1) + (2 \times \frac{3}{2} + 1)} b_1 + \frac{2 \times \frac{3}{2} + 1}{(2 \times \frac{1}{2} + 1) + (2 \times \frac{3}{2} + 1)} b_3 = 6.67 \text{ fm} \quad (2.15)$$

which gives  $\sigma_{coh} \equiv 4\pi b_{coh}^2 = 5.59 \text{ b}$ ; the root mean square of the spin fluctuations gives an incoherent scattering length,  $b_{inc}$ , of

$$\sqrt{\frac{2}{6}|b_1 - b_{coh}|^2 + \frac{4}{6}|b_3 - b_{coh}|^2} = 4.03 \text{ fm} \quad (2.16)$$

which gives  $\sigma_{inc} \equiv 4\pi b_{inc}^2 = 2.04\text{b}$ .

In the incoherent phonon creating process, without the explicit application of the momentum delta function, the summation in the kinematically allowed phonon momentum turns into an integration over the continuous phonon energy, i.e.,

$$\sum_q = \int dE Z(E). \quad (2.17)$$

The density of phonon states,  $Z(E)$ , is introduced to properly weight each phonon energy state. The total incoherent cross section can thus be reduced to a single energy integration. The total coherent cross section calculation, on the other hand, is tedious. It requires a scan through the four dimensional space,  $(E, q_x, q_y, q_z)$ , to search for conditions of coherent phonon creation/annihilation. An incoherent approximation applies the algorithm used for incoherent cross section to evaluate this coherent scattering cross section. This approximation is widely used in numerical calculation packages of scattering law, such as NJOY[103]. In this section, we investigate conditions which justify such an approximation for neutron scattering in solid deuterium.

### 2.3.1 Anisotropy of the Solid Lattice

The differences between the liquid and solid phase introduces a distinct feature into the coherent neutron scattering in these two phases: For superfluid  $^4\text{He}$ , the dispersion relation is isotropic, and there exists only one kinematical condition for UCN production via coherent neutron scattering as discussed before. The anisotropic solid lattice, on the other hand, has a directionally dependent dispersion relation, which leads to the fact that a phonon with a specific momentum can have a different energy when it propagates in different directions. One such dispersion curve in the x-y plane is plotted in Fig.2.4.a. If a cold neutron could scan through the crystal orientation, it would find a corresponding phonon mode to simultaneously transfer its energy and momentum (shown in Fig.2.4.b). As a result, cold neutrons with energy up to the Debye temperature can participate in this coherent downscattering and contribute to UCN production. This phenomenon in solid lattices resembles incoherent scattering. However, to isotropically sample the crystal orientation, neutrons must be



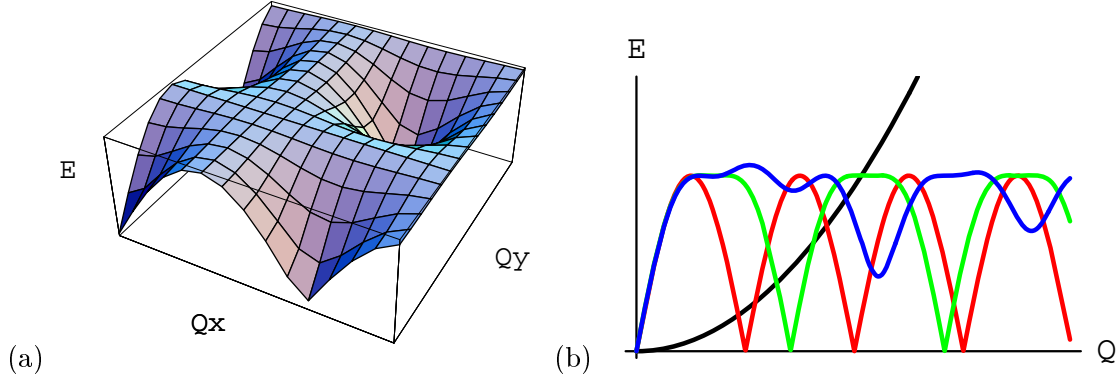


Figure 2.4: (a) The directionally dependent dispersion curve, illustrated on a normal plane. (b) The intersection of the free neutron dispersion curve (black curve) with the phonon dispersion curve at three scattering angles.

in either of these conditions: a  $4\pi$  cold neutron flux scattering from a single crystal or a directed cold neutron beam scattering from polycrystals with random orientations.

### 2.3.2 The Incoherent Approximation

The coherent inelastic cross-section involving one phonon creation is formulated as:

$$\left( \frac{d^2\sigma}{d\Omega dE'} \right)_{coherent}^{1\text{ phonon}} = \frac{\sigma_c}{8\pi M} \frac{k'}{k} e^{-2W(\kappa)} \times \frac{(2\pi)^3}{v_0} \sum_{\tau} \sum_{j, \mathbf{q}} \delta(\omega + \omega_j(\mathbf{q})) \delta(\kappa + \mathbf{q} + \tau) |\kappa \cdot \sigma^j(\mathbf{q})|^2 \frac{(\mathbf{n}(\mathbf{q}) + 1)}{\omega_j(\mathbf{q})}, \quad (2.18)$$

The incoherent approximation is formulated as:

$$\left( \frac{d^2\sigma}{d\Omega dE'} \right)_{inc.approx.}^{1\text{ phonon}} = \frac{\sigma_c}{8\pi M} \frac{k'}{k} e^{-2W(\kappa)} \times \sum_{j, \mathbf{q}} \delta(\omega + \omega_j(\mathbf{q})) |\kappa \cdot \sigma^j(\mathbf{q})|^2 \frac{(\mathbf{n}(\mathbf{q}) + 1)}{\omega_j(\mathbf{q})}. \quad (2.19)$$

In the coherent process, phonons behave as fundamental particles, and thus both energy and momentum conservation laws are strictly followed, which is represented as the energy and momentum delta functions in Eq.(2.18). In the incoherent process, the phonon excitation does not create a single, pure lattice vibrational normal mode with wavefunction,  $\psi_{\mathbf{q}}^j$ , but

a superposition of such normal modes, with a total energy and momentum

$$E = \sum_j \int \omega c_q^j \psi_{q(\omega)}^j dq(\omega) \quad (2.20)$$

$$Q = \sum_j \int q c_q^j \psi_q^j dq, \quad (2.21)$$

being equal to the energy transfer and momentum transfer from the neutron in scattering. Here  $j$  is the branch index, and  $c_q^j$  is the coefficient of each mode, and satisfies  $\sum_{j,q} (c_q^j)^2 = 1$ . In order to produce UCN by downscattering, it does not take a specific phonon from the dispersion curve to match the neutron dispersion curve, but an excitation of the partial sum in the ensemble of phonon modes. There exists different combinations of phonon modes which satisfy the kinematic constraints. In consequence, the delta function of the phonon momentum in the incoherent scattering cross section Eq.(2.19) is “relaxed”. This leads to the fact that all phonons up to the Debye momentum,  $q_\Theta$ , can be created by a neutron with the same energy as illustrated in Fig.2.5. Only scatterings involving single phonon exchange are discussed here. Higher order multi-phonon contributions are suppressed by the small momentum transfer ( $\kappa \cdot r \ll 1$ ) in our case.

Neutron scattering in solid deuterium has a substantial coherent component which accounts for 77% of the total scattering. Calculations of the total cross section rely on the incoherent approximation. According to Placzek and Van Hove[30], the interference correction, which is neglected in the incoherent approximation, is only a 10% effect in the energy range associated with UCN production. Instead of adopting their rigorous numerical calculations evaluating the effect of the zone boundary, we present in appendix C a crude, yet comprehensible treatment of coherent scattering to help us gain more insights into the coherent scattering process. We approach this with an analysis of the allowed momentum phase space for the coherent scattering, incorporating the effect of the inverse lattice momentum. We developed an expression for the density of states and a momentum dependent integration range to feed into a single analytical energy integration. We then compared the integrated result with the results from the incoherent approximation.

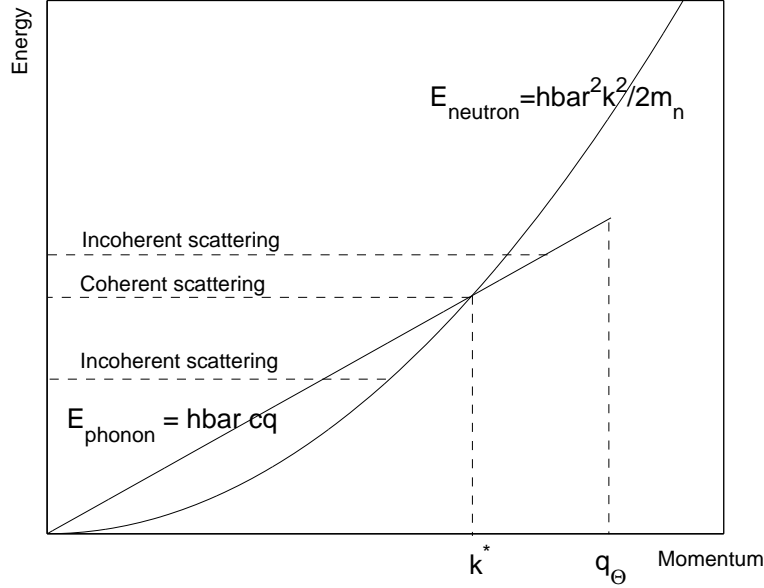


Figure 2.5: A schematic of energy and momentum conservations for phonon creation.

### 2.3.3 Neutron Scattering from D<sub>2</sub> Molecules

Analogous to hydrogen molecules, deuterium nucleus consists of two spin 1 deuterons, giving a total nuclear spin  $S$  of 0, 1 and 2. They can be categorized as ortho-deuterium ( $S=0, 2$ ) and para-deuterium ( $S=1$ ). For both species, their multiple spin states lead to significant incoherent scattering lengths. The dynamics of this two-body molecular system is described by decomposed motion along the orthogonal coordinates, which are represented as the translation of the center of mass, the inter-molecular vibration and the rotation. Its strong atomic bonding leads to hard inter-molecular vibrational modes. It takes 386meV for the first vibrational excitation, and as a result, vibrational excitations do not usually contribute to the thermal neutron scattering. On the other hand, the rotational states, which are described by a quantum number  $J$ , are relatively easy to excite<sup>2</sup>. The  $J = 0 \rightarrow 1$  transition

<sup>2</sup>In order to preserve the bosonic wave symmetry, the ortho-D<sub>2</sub> with a symmetric nuclear spin wavefunction  $S = 0, 2$  couples only to even rotational states, and the para-D<sub>2</sub> with a antisymmetric  $S = 1$  wavefunction couples to odd  $J$  states. Their different rotational energy spectrum leads to the distinctive thermodynamic properties between ortho and para species.

(ortho to para transition) requires an energy of 7.5 meV, which is comparable to the Debye temperature (110K) of solid deuterium<sup>3</sup>. Consequently, this extra intermolecular rotational degree of freedom provides neutrons with a channel for energy exchange other than the simple phonon mechanism. Following the calculation given by Koppel and Young[31], who simplified the scattering matrix into a molecular part times a center-of-mass translational part (see appendix A), we further apply the translational contribution to the case of neutron scattering from a solid (see appendix B). We perform a phonon expansion (in the case of small momentum transfer) and calculate the neutron scattering cross section incorporating different nuclear spin couplings of ortho and para-D<sub>2</sub> and all the possible energy excitations as well. The results indicate that the different spin couplings and the rotational states transitions introduce a 10% difference in the neutron downscattering cross sections between ortho and para-D<sub>2</sub>. However, the direct neutron coupling to the  $J = 1$  rotational state in para-D<sub>2</sub> induces a large UCN upscattering cross section without any phonon exchange. It has a cross section of:

$$\left(\frac{d\sigma}{d\Omega}\right)_{J=1 \rightarrow 0}^{0 \text{ phonon}} = \frac{3}{4} a_{inc}^2 \frac{k'}{k} e^{-2W(\kappa)} \times \left[ 4j_1^2\left(\frac{\kappa a}{2}\right) C^2(101; 00) \right], \quad (2.22)$$

where  $j_1(\frac{\kappa a}{2})$  is a spherical Bessel function of order one[74]. Because of the unsuppressed zeroth order phonon contribution, this upscattering loss is one order of magnitude larger than the typical phonon upscattering in ortho-D<sub>2</sub> (shown in Fig.2.6). As a result, the UCN lifetime in a pure para-D<sub>2</sub> solid is reduced from the nuclear absorption time of 150 ms to this para-D<sub>2</sub> upscattering time of 1.5 ms. A calculation of this upscattering cross section is presented in appendix B. Our solutions to mitigate this excessive UCN loss by ortho/para-D<sub>2</sub> conversion are discussed in the next chapter.

---

<sup>3</sup>Because of the strong atomic binding energy of the deuterium molecule, the Van der Waals interactions between D<sub>2</sub> molecules are relatively weak, leading to a small Debye temperature in solid D<sub>2</sub>.

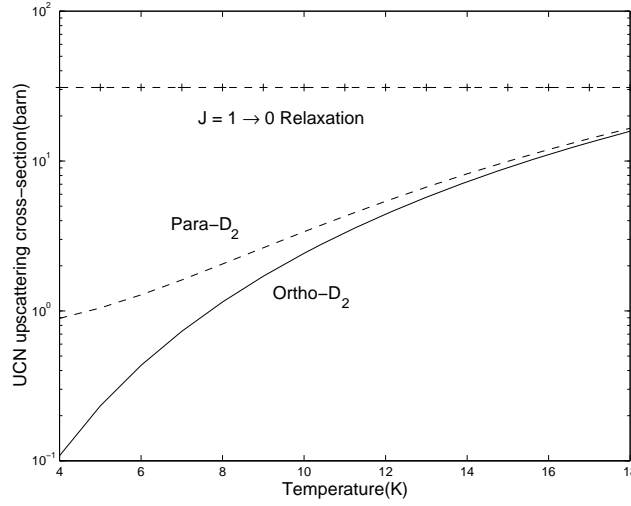


Figure 2.6: The UCN upscattering cross-section vs. the temperature of solid  $D_2$ . The one-phonon annihilation cross-section in an ortho- $D_2$  solid (solid curve) and in a para- $D_2$  solid (dashed curve) are plotted. The dashed-dagger line is the temperature independent UCN upscattering cross-section involving  $J=1 \rightarrow 0$  relaxation not coupled to phonons in a para- $D_2$  solid.

## 2.4 Comparison of the S- $D_2$ and superfluid $^4\text{He}$

The main difference between S- $D_2$  and superfluid  $^4\text{He}$  is the UCN residence time.<sup>4</sup> While UCN can stay in superfluid  $^4\text{He}$  until it  $\beta$ -decays (887s), UCN in solid deuterium are absorbed by the deuteron in 150ms after they are produced. The ideal UCN density can thus be formulated as:

$$\begin{aligned} \rho_{ucn} &= P(CN \rightarrow UCN) \times \tau \\ &= \begin{cases} \int_{E_{ucn}}^{T_{Debye}} \Phi(E_{cn}) \sigma(E_{cn} \rightarrow E_{ucn}) dE \times \tau_{nuc.abs.} & \text{for S-}D_2 \\ \Phi(E^*) \sigma(E^* \rightarrow E_{ucn}) \times \tau_{\beta-decay} & \text{for superfluid } ^4\text{He.} \end{cases} \end{aligned}$$

Considering the efficiency of neutron flux coupling, 80% of a 30K Maxwell-Boltzmann distributed cold neutron flux can be used to produce UCN in S- $D_2$ . This fraction is 4 orders

---

<sup>4</sup>We focus on the ideal situation where the phonon upscattering is suppressed and the effect of isotopic impurities is negligible.

of magnitude greater than the case of superfluid  $^4\text{He}$ . Even so, for a single cold neutron the UCN production probability is less in S-D<sub>2</sub> than in superfluid  $^4\text{He}$  because UCN production is only one of the many inelastic scattering channels. The coherent phonon excitations in superfluid  $^4\text{He}$  that lead to UCN production are two orders of magnitude more likely than the UCN production mechanism in S-D<sub>2</sub>. As a result, S-D<sub>2</sub> has a production rate two orders of magnitude higher than superfluid  $^4\text{He}$ . S-D<sub>2</sub> is thus a UCN source which outputs a higher UCN current than superfluid  $^4\text{He}$ . Moreover, the limiting production time in superfluid  $^4\text{He}$  (the neutron  $\beta$ -decay lifetime, 887 seconds) is 4 orders of magnitude longer than S-D<sub>2</sub>. Thus, even with a smaller UCN production rate, superfluid  $^4\text{He}$  can achieve an ultimate UCN density a few hundred times greater than that of solid deuterium.

Once superfluid  $^4\text{He}$  is cooled down to 0.75K, the dominant phonon upscattering due to the inelastic partial phonon energy exchange is suppressed to a level comparable to the neutron  $\beta$ -decay lifetime. The superthermal enhancement in solid deuterium is limited by the large nuclear absorption loss, and thus further cooling below 5K will not significantly enhance the UCN yield. The cryogenic requirement for a solid deuterium source is therefore less demanding.

It takes the beta-decay lifetime ( $\sim 1000 \text{ sec} \sim 15 \text{ min}$ ) to reach the saturation UCN density in superfluid  $^4\text{He}$ , and thus a continuous cold neutron source from a reactor is appropriate. Solid deuterium, on the other hand, only takes 40 ms to reach saturation, and thus, either a short cold neutron pulse from a spallation target or a continuous beam from a reactor are applicable. Because nuclear absorption limits the useful volume of solid deuterium, and S-D<sub>2</sub> operates at a higher temperature than superfluid He, it is more feasible to place a S-D<sub>2</sub> source very close to a reactor core.

Different features of these sources lead to different operating methods and conditions which impacts the design of subsequent neutron experiments. For a superfluid  $^4\text{He}$  source, an *in situ* experiment where the volume of the source is also the volume of the experiment, makes optimum use of the stored UCN. For example, a neutron lifetime measurement with magnetically trapped UCN produced in superfluid  $^4\text{He}$  has been implemented at NIST[28],

and a neutron EDM measurement with UCN produced in superfluid  $^4\text{He}$  at LANSCE has been proposed[19]. In the case of solid deuterium, it is essential to separate the production material from the UCN storage volume (which supplies the experiment with UCN). A counting experiment attached to the S-D<sub>2</sub> UCN source can make use of this large instantaneous UCN flux for high counting rates and a superb signal to noise ratio.

## Chapter 3

# Ortho/Para-D<sub>2</sub> Conversion

Para-D<sub>2</sub> is, unfortunately, a source of large UCN upscattering. Controlling the concentration of para-D<sub>2</sub> is thus an essential step towards realizing solid deuterium as an intense UCN source. We implemented an experiment to convert para- to ortho-deuterium molecules, using the procedure of flowing D<sub>2</sub> gas through a cryogenic cell filled with hydrous ferric oxide paramagnetic granules. This process efficiently reduced the para-D<sub>2</sub> concentration from 33.3% to 1.5%. Rotational Raman spectroscopy was applied to measure the residual para-D<sub>2</sub> contamination to 1 part in 10<sup>3</sup>, and the hydrogen contamination to 1 part in 10<sup>2</sup>. Some advantages of this technique over the traditional thermal conductivity measurements of the ortho/para ratio are also discussed at the end of this chapter.

### 3.1 Motivation

In a recent investigation of solid D<sub>2</sub> as a UCN source[34], it was surmised that the yield of UCN is correlated with the spin states of the deuterium molecules. Subsequently, detailed neutron scattering calculations, taking into account both the intra-molecular rotational transitions and the lattice vibrational excitations, predicted very different cross sections in lattices comprised of the two molecular species (ortho- and para-) of D<sub>2</sub>. This cross section difference originates from the fact that the UCN interaction with a deuterium molecule can induce a conversion of para to ortho-D<sub>2</sub>. However, UCN do not have sufficient energy



to cause the reverse process (para is the more energetic state). This conversion process results in a greatly shortened UCN resident time[35]. The elimination of this unwanted source of UCN loss enhances the superthermal performance of solid D<sub>2</sub>, which motivates the implementation of a para- to ortho-D<sub>2</sub> conversion apparatus presented in this report (Room temperature D<sub>2</sub> has a 33.3% para concentration, and relaxation of para to ortho state in solid D<sub>2</sub> takes months).

### 3.2 Ortho/Para-D<sub>2</sub> Physics

Quantum mechanics endows deuterium molecules with unique properties. The deuteron ( $S = 1$ ) is a boson, and thus, the deuterium molecule (D<sub>2</sub>) has a symmetric wavefunction under permutations of the two identical nuclei. The ortho state for deuterium (total nuclear spin,  $S = 0, 2$ ) can only have symmetrical molecular rotational states of even  $J$ , the rotational quantum number. The para state (total nuclear spin,  $S = 1$ ) can only have anti-symmetrical molecular rotational states of odd  $J$ . The vibrational excitations along the molecular axes, however, do not introduce such complications. The reasons are as follows: first, vibrations around the center of the mass are always symmetric, and second, the energy of the lowest rotational excitation ( $\sim 4000\text{K}$ ) is already too large for energy transfers associated with UCN. In addition, the ground state of the molecular electrons has a null net spin, and therefore contributions from the electron-nucleus as well as the electron-neutron couplings are negligible.

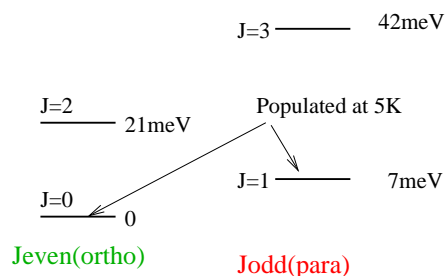
In the high temperature limit, equal population of the sub-states suggests that the para state ( $S = 1$ ) occupies,

$$\frac{2 \times 1 + 1}{1 + (2 \times 1 + 1) + (2 \times 2 + 1)} = 33.3\%$$

of the total population. The rotational energy spectrum (shown in Fig.3.1) can be classically described:

$$E_{rot} = \frac{J^2}{I} = \frac{B}{2}J(J+1), \quad (3.2)$$

where the factor  $B$  is related to the momentum of inertia,  $I$ , as  $B = \hbar^2/I = \frac{\hbar^2}{2M_D(a/2)^2} = 7.5$

Figure 3.1: The rotational energy spectrum of ortho- and para-D<sub>2</sub>.

meV, to the zeroth order. The separation between the two nuclei,  $a$ , is 0.74 Å. Note that  $B$  is in general  $J$  dependent, as the D<sub>2</sub> molecule is distorted at high angular momenta. The energy required to make the transition from the ground state ( $J = 0$ ) to the first excited state ( $J = 1$ ) is  $B = 7.5$  meV.

The molecular ground state ( $J = 0$ ) is in the ortho configuration, which is only accessible through transitions from other even  $J$ s among the ortho family. For a free non-interacting gas, cross transitions between even  $J$  (ortho) and odd  $J$  (para) states are prohibited by the spin selection rules. Conversions between para to ortho states involve a change of the spin symmetry through spin flips, where in general an external interaction potential is required. In fact, spontaneous spin flipping occurs; the spin-flipping channel through self-conversion occurs through collisions between the aspherical molecules ( $S = 1, 2$ ), whose non-central quadrupole interaction provides a small but yet finite torque to induce spin flip. The resulting time constant for such a self-conversion is, however, very long, and has been measured to be on the order of months[36]. Consequently, without special treatments, the condensed D<sub>2</sub> solid inherits the high para concentration of the initial gas phase, and throughout the short course of the experiment (several days), self-conversion is insignificant.

On the other hand, neutron scatterings provide a direct path to nuclear spin flips, because the nuclear strong interaction between a neutron and a deuteron introduces spin-dependent matrix elements which mix ortho and para states. The impact on the UCN production in solid D<sub>2</sub>, after introducing this additional spin flip channel, is not as drastic

as that on its reverse process, the UCN upscattering. In para-D<sub>2</sub>, UCN can be upscattered by directly absorbing this excessive amount of rotational energy, whereas the  $J = 1$  para molecule is quenched to the ortho ground state. It is the existence of this wide-open scattering channel which results in a very short residence time for UCN in para-D<sub>2</sub>.

### 3.3 Conversion of Para-D<sub>2</sub> into Ortho-D<sub>2</sub>

One of the many ways to eliminate the para-D<sub>2</sub> is to convert it into the ortho-D<sub>2</sub> state. The technique of pre-conversion of para-D<sub>2</sub> gas into the ortho state has many industrial applications [36], and is a straightforward and economical solution to our problems. UCN upscattering by para-D<sub>2</sub> in solid D<sub>2</sub> with 1% para concentration gives the same lifetime as that from nuclear absorptions by deuterons. This sets the goal for this conversion technique.

Lowering the temperature of the D<sub>2</sub>-catalyst system suppresses the population of non-zero  $J$  states and ensures a high purity of the ortho-D<sub>2</sub>. The residual population of the  $J = 1$  (para) state is characterized by the transition energy,  $E_{JJ'} = E_{01} = 7.5$  meV ( $\sim 80$  K), through the Boltzmann factor  $e^{-80/T}$  in the low temperature limit. When the converter is operated at 17K, the para concentration can in principle be reduced from 33.3% down to  $e^{-80/17} = 1\%$ . An adequate finite vapor pressure (50 Torr) can be also extracted from the converter at this temperature to grow the deuterium solid in a continuous fashion.

#### 3.3.1 Catalyzed Conversion

At least two mechanisms exist that catalyze the ortho/para conversion of hydrogen: paramagnetic and chemical mechanisms[37].

Paramagnetic conversion was first studied with the paramagnetic impurities (primarily oxygen) in charcoal. This catalyst agent, on which D<sub>2</sub> molecules are temporarily adsorbed and form a van der Waals layer, has a large magnetic field near its surface. The magnetic field gradient induces a relative dephasing between the two precessing nuclear spins, and results in a spin flip. Chemicals with manifest magnetic properties can serve as the catalyst [41]. With such catalysts, spin flipping reactions accelerate, which then establishes the

thermal populations for all the rotational states in a timely fashion. For a single adsorbed molecule this transition rate is almost temperature independent, and thus, the conversion rate of a gas flow is dominated by the gas adsorption probability. As a result, the overall conversion efficiency increases as the catalyst temperature decreases.

The other mechanism involves chemisorbed hydrogen on metal surfaces. Metals such as tungsten, platinum, palladium and nickel have been studied for this mechanism. Stringently out-gassed charcoal is in this category, too. This mechanism involves the dissociation and recombination of hydrogen molecules in a loosely bound chemisorbed layer. To proceed to spin flip, the molecules must first overcome a finite dissociation energy, and thus the conversion efficiency increases as the temperature rises, contrary to the paramagnetic mechanism.<sup>1</sup>

A paramagnetic catalyst is therefore the obvious choice for our low temperature application. Paramagnetic transition metal ions on a slight diamagnetic structure serve well as highly effective catalysts. A first-order model that suggests the reaction rate to be proportional to the square of the effective magnetic moment  $\mu_{eff}$  (in the unit of Bohr magneton),

$$\mu_{eff} = 2\sqrt{S(S+1)} = \sqrt{n(n+2)}, \quad (3.3)$$

where  $S$  is the total electronic spin of the metal ion, and  $n$  is the number of the unpaired electrons. The exchange interaction between electrons which results in a reduced strength of magnetic coupling is assumed to be negligible.<sup>2</sup> The ferric ion ( $\text{Fe}^{3+}$ ) has the most unpaired electrons in  $d$  shell, and thus, carries the largest magnetic moment ( $\text{Cr}^{3+}$ : 3.87,  $\text{Mn}^{4+}$ : 3.87,  $\text{Fe}^{3+}$ : 5.92,  $\text{Co}^{3+}$ : 4.92,  $\text{Ni}^{2+}$ : 2.83)[41]. Some rare earth elements (Gd, Nd, Ce), with more unpaired electrons in  $4f$  orbitals, however, do not exhibit a higher conversion efficiency[43].

Another important factor to consider is how to reduce the Heisenberg exchange inter-

---

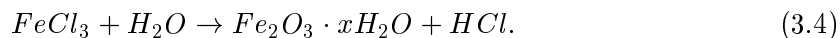
<sup>1</sup>The reaction of  $\text{H}_2 + \text{D}_2$  to produce HD (hydrogen-deuterium molecule) is of the same mechanism. Therefore one can predict that HD formation has a rate which directly correlates to the ortho/para conversion rate with a correction on the effect of the zero point motions of H and D.

<sup>2</sup>Chromium atom has the most unpaired electrons (5 in  $3d$ , and 1 in  $4s$  orbital), however, electrons of the pure chromium, which is in metal form, are conduction electrons, and thus, no longer carry manifest magnetic properties.

actions, which are most likely to result in a reduced effective magnetic moment. This is referred to the magnetic dilution effect[38]. Aqueous solutions and ion oxide crystals have moderate magnetic dilution. Metal oxides impregnated in a supporting alumina ( $Al_2O_3$ ) gel[38] are even better because their magnetic sites are further separated, and thus, the exchange interactions are suppressed. A converter of this kind also benefits from the alumina's large surface area of adsorption ( $\sim 300 \text{ m}^2/\text{g}$ ). One interesting alternative for the support is aerogel (silica gel) with an effective surface area of  $\sim 900 \text{ m}^2/\text{g}$ . However, a preliminary investigation of oxides on aerogel did not show a significant improvement of the conversion efficiency[38].

There also exists a class of self-supporting metal oxides in the form of colloidal gels, with an effective surface area of  $100\sim 300 \text{ m}^2/\text{g}$ . The terminology "gel" here refers to solid (or semi-solid) colloids. The activities of different metal oxide gels were studied in Ref.[41], where the scientists mistook the chemical composition of these self-supported oxides for hydroxides. In fact, the chemical is hydrous oxide. It is a gelatinous precipitate forming a microscopic network composed of extremely finely divided metal oxide particles which have coalesced to form flexible filaments or chains, and which absorb water very strongly and so are highly hydrous[39]. Considering the available surface area per unit weight for vapor adsorption, hydrous oxides are an ideal catalyst because they provide the highest collision rate in a constant volume flow. As a result, hydrous ferric oxide should be the most effective catalyst for ortho/para hydrogen conversion, and previous experimental tests all give supporting evidence.

The formation of this chemical is straightforward[39]: Hydrolysis of electrolytic iron salt ( $FeCl_3$ ) in water solution (boiling water) makes a precipitate of ferric oxides and acid:



Further addition of base ( $Na(OH)$ ) into the solution doubles the decomposition and increases precipitation. The solution is then peptized with ammonium hydroxide by washing out the excess agglomerating metallic salt and acid and decanted preferably with the aid of a centrifuge. The precipitate is then left drying in the air for a few days and breaks down in

various sizes.

Hydrous ferric oxide is non-ferromagnetic. It does not form a hydrate, in which water molecules bond in specific ways to the chemical. Therefore the possible reduction of the conversion efficiency associated with the saturation of the absorption sites (which should be reserved for D<sub>2</sub> gas) is not a problem in this water-rich compound.

We activated the catalyst before the initial operation by heating it up to 130 °C for 24 hours under the vacuum, and then back filled it with deuterium gas for preservation. Installation of the converter cell into the vacuum system was performed with care to minimize exposures to the atmospheric air. After some period of operation, which varies with the conversion load, regeneration of the catalyst is performed with the same activation procedure.

The problem of utilizing hydrous gel is that upon aging it loses water and coalesces into granules. This change of structure from amorphous gel to micro-crystals is evident from X-ray scattering experiments[39]. The volume shrinks by over a factor of 500 due to this dehydration. It is thus advisable to work with fresh gels, and not to attempt repeated regenerations. One way to prevent dehydration might involve refrigeration of the catalyst right after formation. A potential concern regards to the possible HD formation while D<sub>2</sub> gas passes through the hydrogen rich catalyst via isotope exchange. This, however, was not experimentally observed (see Sec. 3.4) because of the low operational temperature of the catalyst cell.

### 3.3.2 Design of the Converter

We built a cylindrical cell made of OFHC copper as the converter chamber, illustrated in Fig. 3.2. It is attached to the cold head of an air-cooled <sup>4</sup>He compression cryopump, Varian CryoTorr 8, which served as a refrigerator. Its inner cooling stage (cold head) has a cooling power of 1 W at the temperature of 10 K (5 W at 20K), which is adequate for the required conversion load. This closed system of <sup>4</sup>He compression cryopump provides an easy and compact alternative to the liquid <sup>4</sup>He evaporation cooling used in previous experiments[40].

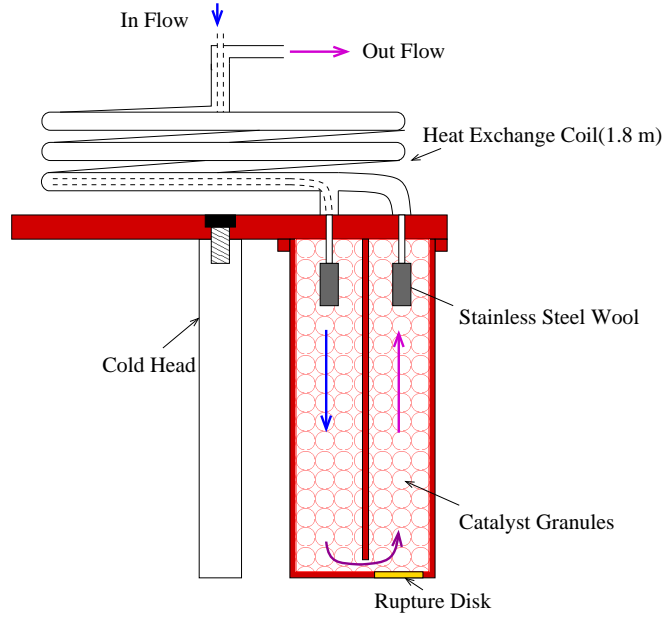


Figure 3.2: A schematic of the para/ortho-D<sub>2</sub> converter.

Features of the design are, first, the D<sub>2</sub> gas exit port is situated at the coolest plate to anchor the temperature of the output converted D<sub>2</sub> and also to minimize the temperature gradient across the D<sub>2</sub> gas flow. Second, in order to reduce the head load onto the cold head, we designed a 180 cm long heat exchange coil made of coaxial S.S. thin tubes. The inflow gas in the inner thin tube is pre-cooled by the outflow gas flowing in the outer tube. Its long length increases the thermal resistance and thus minimizes the heat conduction through the stainless steel (S.S.) tubes to the ambient environment. With a flow rate of 36 liter/hour ( $\sim 0.6$  liter/min) of STP gas, the heat load is  $\sim 1$  W, which is mainly the D<sub>2</sub> gas specific heat and the ortho/para conversion energy. The 100 c.c. inner volume of the cell is filled with fine grained hydrous ferric oxide as a catalyst. The catalyst granules are confined in the converter cell by S.S. wool filters plugged into both the gas entrance and the exit ports. A heater is mounted on the cold plate so that we can vary and control the temperature of the converter. Two temperature diode sensors are separately placed on the top and the bottom of the copper cylinder to monitor the temperature as well as the

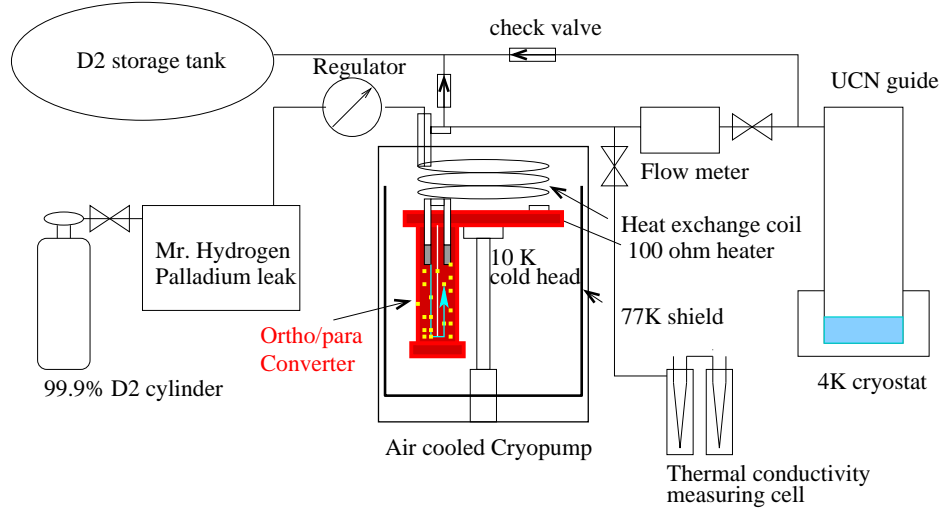


Figure 3.3: A schematic of the gas handling system used for the S-D<sub>2</sub> UCN source preparation.

gradient. In order to tolerate a baking for the catalyst regeneration as previously discussed, a wire made of indium/lead alloy is used between the top plate and the converter can to seal the vacuum. This soft alloy has a higher melting point (150 °C) than the regeneration temperature (130 °C). Pure indium metal (with a melting point of 110 °C) can not tolerate such a baking.

After flowing through the converter in which the catalyst is held below the D<sub>2</sub> triple point temperature (18.7K), D<sub>2</sub> is converted predominantly into the ortho state with a reduced para contamination of roughly 1%.

As illustrated in Fig. 3.3, this para to ortho-D<sub>2</sub> converter with the <sup>4</sup>He compression cryostat is then incorporated into the D<sub>2</sub> gas handling system which is used to prepare the UCN source. Cajon VCR S.S. tubes and connectors are used to the maximum extent possible in constructing this clean gas handling system. The ortho/para-D<sub>2</sub> converter is in series with a hydrogen gas purifier (palladium leak) which operates at 400 °C. Care was taken to minimize the magnetic surface area inside the apparatus placed after the ortho/para-D<sub>2</sub> converter, in order to prevent the back-conversion and preserve the fully



converted ortho-D<sub>2</sub>. Our measurements indicate that the room temperature S.S. tubes and the Ni coated UCN guides in this setup do not induce measurable D<sub>2</sub> back-conversions over the course of the experiment (typically two days).

### 3.4 Measurement of the Ortho/Para-D<sub>2</sub> Ratio

An in-line thermal conductivity measurement with hot wire cells was frequently performed on the outflowing D<sub>2</sub> to characterize the performance of the ortho/para-D<sub>2</sub> converter. An absolute uncertainty of 3% in the para-D<sub>2</sub> concentration was the best performance we could achieve with this in-line measurement of low pressure D<sub>2</sub> ( $\sim 30$  mbar). Molecular Raman spectroscopy [46] was later conducted on the evaporated D<sub>2</sub>, which was collected from the cryostat at the end of each fill. A high precision determination of the ortho-D<sub>2</sub> purity to one part in  $10^3$  can be achieved in a hour using an optical spectrum scan of a 0.5 atm sample.

#### 3.4.1 Raman Spectroscopy

A visible (far off-resonance) laser is used to probe the D<sub>2</sub> gas molecule sample. The rotational Raman spectrum gives information on populations of its rotational states.

#### The Theory of Raman Scattering

The dipole approximation of light scattering from atoms and molecules gives a cross-section of [44]:

$$\frac{d\sigma_{0 \rightarrow n}}{d\Omega'} = \frac{e^4 \omega \omega'^3}{c^4} \left| \sum_m \left[ \frac{\langle n | R \cdot \lambda'^* | m \rangle \langle m | R \cdot \lambda | 0 \rangle}{\epsilon_0 - \epsilon_m + \hbar\omega + i\eta} + \frac{\langle n | R \cdot \lambda | m \rangle \langle m | R \cdot \lambda'^* | 0 \rangle}{\epsilon_0 - \epsilon_m - \hbar\omega' + i\eta} \right] \right|^2, \quad (3.5)$$

where  $\omega$  and  $\omega'$  represent the frequency of the incident and scattered photon, respectively. The scatterer makes a transition from the initial state  $|0\rangle$  to the final state  $|n\rangle$ , via intermediate  $|m\rangle$  states (these states can be molecular rotational states which typically have

energies on the order of 10 meV, as well as the electronic excitation states which have relatively higher energies around 1 eV). The scatterer's energy is represented by  $\epsilon$  with the subscript indicating the energy state.  $R = \sum_i r_i$  is the dipole moment operator, and  $\lambda$  is the polarization vector of the light. The energy conservation constraint is only imposed on the initial and final states,

$$\epsilon_0 + \hbar\omega = \epsilon_n + \hbar\omega'. \quad (3.6)$$

This second order solution Eq.(3.5) describes scattering process involving virtual transitions through all the allowed internal states, in which the energy of the system is not conserved at the vertices.

The first order contribution to the elastic scattering is zero, because the single application of the dipole moment operator only connects states with opposite parities, unless it involves in an absorption and a subsequent re-emission of a real photon, subject to the condition that the energy of the photon has to match the internal transition energy. As a result, amplitudes of the elastic scattering (Rayleigh scattering),  $n = 0$ , and the inelastic scattering (Raman scattering),  $n \neq 0$ , are both second order contributions which involve virtual excitations of all the intermediate states with a parity opposite to both the initial state and the final state. In the case where the incident photon energy is larger than the internal excitation energies, i.e.,  $\hbar\omega \gg \epsilon_n - \epsilon_0$ , the amplitude ratio of Rayleigh and Raman scatterings scales with the ratio of the matrix elements of the polarization tensor is given by

$$\frac{\langle n | R \cdot \lambda'^* R \cdot \lambda | 0 \rangle}{\langle 0 | R \cdot \lambda'^* R \cdot \lambda | 0 \rangle}, \quad (3.7)$$

which is on the order of 1 for nominal gas. Furthermore, the angular momentum selection rules imposed by dipole transitions allow only

$$\Delta J = 0 \quad \text{for Raleigh scattering and} \quad (3.8)$$

$$\Delta J = \pm 2 \quad \text{for Raman scattering,} \quad (3.9)$$

in the case of rotational state excitations with rotational quantum number  $J$  changed by  $\Delta J$ .

The total Raman scattering cross section incorporates populations of the initial states. As an example, for particles in thermal equilibrium, the Raman cross section becomes

$$\frac{d\sigma^{Raman}}{d\Omega'} = \sum_J Q^{-1} g_J (2J+1) \exp(-E_J/kT) \frac{d\sigma_{J \rightarrow J \pm 2}}{d\Omega'}. \quad (3.10)$$

with ‘+’ for Stokes lines, and ‘-’ for anti-Stokes lines.  $Q$  is the normalization factor, and  $g_J$  is the multiplicity of the nuclear spin states.

### Experimental Setup

We performed a proof-of-principle test with the Raman spectroscopy setup in Professor Happer’s atomic group at Princeton University described in Ref.[45]. An argon ion laser with 15 W output power was used and its 5145 Å line was refracted to shine through the glass cell containing the sample gas. The scattered dipole radiation was collected transverse to the laser path and focused into a 0.85 m Spex 1404 double grating spectrometer with a PMT light detector. Fig.3.4 shows the measured spectrum (including both Stokes and anti-Stokes lines) of a mixture of normal, room temperature H<sub>2</sub> and D<sub>2</sub> gas with partial pressure of approximately 600 Torr each, which are contained in a 10 c.c. spherical Pyrex glass cell. The FWHM is 0.6 Å with slit widths of 100 μm.

This reference spectrum provided us with the information we required to construct a D<sub>2</sub> Raman spectroscopy system. For our application, we are less limited by the peak resolution due to the large spacing between D<sub>2</sub> rotational Raman lines. To perform a high precision measurement on the small para-D<sub>2</sub> fraction, a high light throughput is more critical than a high resolution. Scaling down of the laser power to 40 mW would reduce the peak count rate from 2300 Hz to 6 Hz. Utilizing a single grating spectrometer, with a 50 cm focal length increased the count rate by at least a factor of  $2 \times (85/50)^2 \sim 6$ . Increasing the slit width to 300 μm further enhanced the count rate to 120 Hz, with a sacrifice in the peak resolution to  $0.6 \text{ Å} \times (300/100) \times (85/50) = 3 \text{ Å}$ , which is only  $3\text{Å}/29\text{Å} = 10\%$  of the rotational Raman line spacing. Using a small PMT with a dark count rate of 5 Hz, a system with the above hardware parameters allowed us to perform a measurement in para-D<sub>2</sub> concentration with

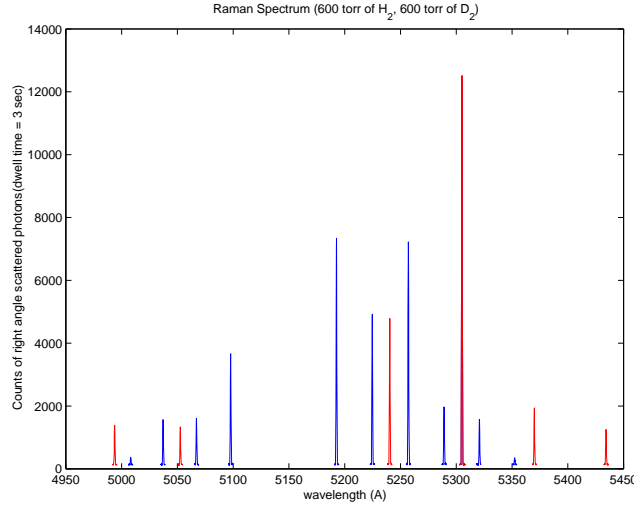


Figure 3.4: The first Raman spectrum of normal (non-converted) H<sub>2</sub> and D<sub>2</sub> with approximately 600 Torr partial pressure each. The power from the argon ion laser is 15 W. The primary laser wavelength is 515 nm. The dashed and solid peaks are spectrum of H<sub>2</sub> and D<sub>2</sub>, respectively.

a precision of  $(5\text{Hz}/120\text{Hz}) \times 33.3\% = 1.4\%$ , and we have performed measurements better than this estimate with the optimized setup described below.

A schematic of our Raman spectroscopy setup is shown in Fig.3.5. We use a small air-cooled argon ion laser, American Laser Corp. model 60x, which outputs a single line of unpolarized 488 nm TEM<sub>00</sub> beam with a power of 40 mW. The higher frequency 488 nm line gives an increase in the count rate of  $\sim 18\%$  from Raman scattering compared with the 515 nm laser line, according to the  $\omega^3$  dependence in the cross section Eq.(3.5). The laser line is directed and focused by two convex lenses ( $fl = 35$  mm) into the center of a cubic cell, which is built of a S.S. housing with 4 flat parallel uncoated quartz windows. A 58 mm Nikon camera lens ( $fl : \infty \sim 0.5$ ) is placed close to the cell for the maximum collection of the Raman scattering light perpendicular to the laser beam. It also focuses the Raman radiation onto the entrance slit of the spectrometer, which is placed approximately one focal length away. The spectrometer is a Jarrel Ash, model 82-000, single grating spectrometer

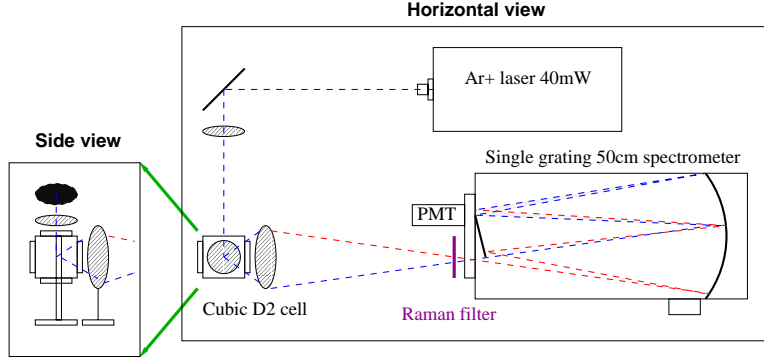


Figure 3.5: A schematic of the D<sub>2</sub> Raman spectroscopy setup.

with a focal length of 50 cm. It is equipped with a 1800 g/mm holographic grating blazed at 500 nm. We direct the primary laser path vertically through the cell so that it would be in parallel to the slit, in order to optimize the collection of scattered light through the slit into the spectrometer. A 1/2" Hamamatsu R647P PMT is used in single photon counting mode on the exit of the spectrometer.

A 488 nm narrow band filter (bandwidth = 30 Å), Omega Optical model XR3000-495AELP, was placed in front of the spectrometer entrance to compensate for the poor stray light rejection of single grating spectrometers. This filter greatly suppresses the background signal in the Raman spectrum as shown in Fig.3.6, and thus, is crucial for the high precision measurements of the para-D<sub>2</sub> concentration of a converted D<sub>2</sub> gas sample. However, with this Raman filter, the first rotational peak is filtered out and the second peak is distorted. We thus used the  $J = 2 \rightarrow 3$  and  $J = 3 \rightarrow 4$  peak to extract the ortho/para-D<sub>2</sub> ratio.

### Results and Analysis

Our strategy to obtain the para-D<sub>2</sub> concentration using the rotational Raman spectroscopy is based on a comparison between spectra of the unknown sample and a reference with a known ortho/para-D<sub>2</sub> ratio. Typical spectra obtained from our setup are shown in Fig.3.7. The amplitude ratio of the fourth ( $J = 3 \rightarrow 5$ ) to the third ( $J = 2 \rightarrow 4$ ) peak among the Stokes lines scales with the ratio of para-D<sub>2</sub> fraction,  $f_p$ , to the ortho-D<sub>2</sub> fraction,  $f_o$ ,

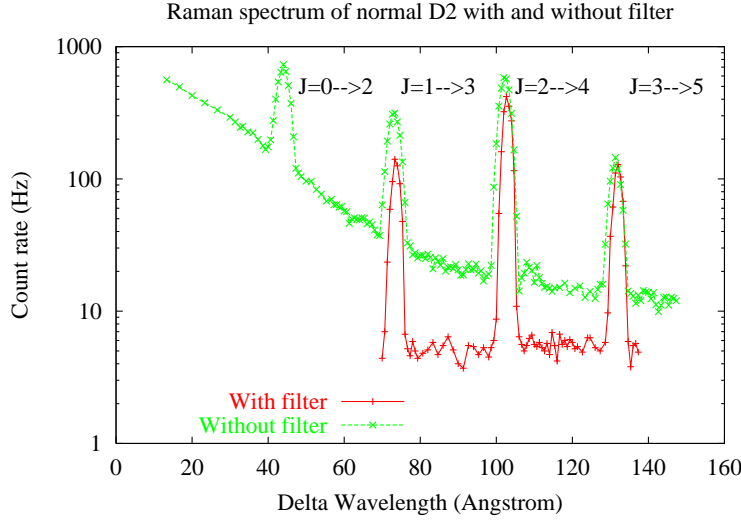


Figure 3.6: Rotational Raman spectrum with and without a Raman filter.

according to Eq.(3.10),

$$\frac{\text{Amp}_{J=3 \rightarrow 5}}{\text{Amp}_{J=2 \rightarrow 4}} = \left( \frac{f_p}{f_o} \right) \frac{Q_p^{-1} g_3 7 e^{-E_3/kT} \sigma_{J=3 \rightarrow 5}}{Q_o^{-1} g_2 5 e^{-E_2/kT} \sigma_{J=2 \rightarrow 4}}. \quad (3.11)$$

Here the normalization factor  $Q_p$  is a sum of spin multiplicities weighted by the Boltzmann factor over all the odd rotational states of para-D<sub>2</sub>, i.e.,

$$Q_p = \sum_{\text{odd } J} g_J (2J + 1) \exp(-E_J/kT), \quad (3.12)$$

and for  $Q_o$  the sum is over even  $J$ 's. When compared with a spectrum of the reference sample measured at the same temperature (room temperature), the statistical weighting factors and the cross sections cancel out, leaving only the para to ortho ratio,  $f_p/f_o$ , of the unknown sample. “Normal” D<sub>2</sub> which has an equilibrium population of rotational states at room temperature is conveniently used as the reference which has  $f_p/f_o = 1/2$  (at the high temperature limit).

These spectra in Fig.3.7 illustrate the effect of para to ortho-D<sub>2</sub> conversion. The  $J = 3 \rightarrow 5$  peak height is reduced, showing a reduction of the para-D<sub>2</sub> concentration from 33.3% (‘+’ curve, with D<sub>2</sub> collected before the converter) to 1.54% (‘×’ curve, with D<sub>2</sub> collected

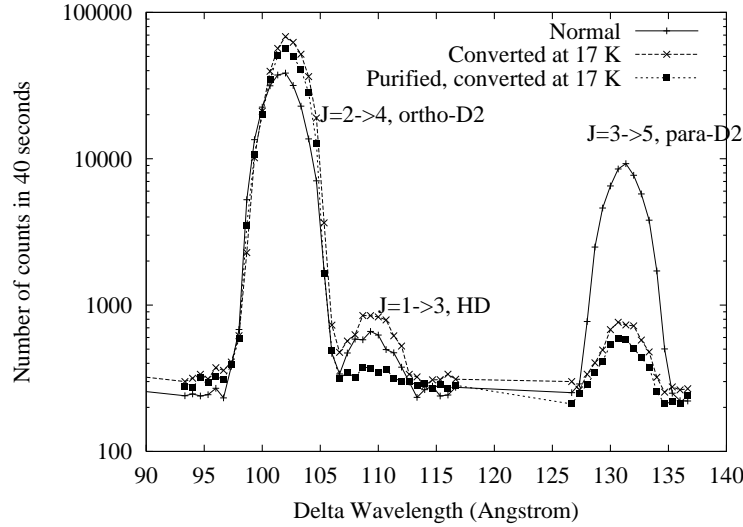


Figure 3.7: The Raman spectrum of converted and unconverted D<sub>2</sub>. Slit widths are set to 400  $\mu\text{m}$ . The ‘+’ curve is the reference normal D<sub>2</sub>. The ‘x’ curve is a converted D<sub>2</sub> with  $(1.54\% \pm 0.21\%)$  of para-D<sub>2</sub>, and  $(1.27\% \pm 0.12\%)$  of HD. The square-dotted curve is purified converted D<sub>2</sub> with  $(1.42\% \pm 0.20\%)$  of para-D<sub>2</sub>, and a reduced HD contamination of  $(0.26\% \pm 0.06\%)$ .

after the 17 K converter). This spectra also show a noticeable HD peak ( $J = 1 \rightarrow 3$ ) next to the  $J = 2 \rightarrow 4$  ortho-D<sub>2</sub> peak. Because the UCN lifetime in solid D<sub>2</sub> is also sensitive to the presence of hydrogen, which strongly absorbs UCN via nuclear capture on the H nuclei, our knowledge of the HD concentration is important in our study of the superthermal S-D<sub>2</sub> source. Rotational Raman spectroscopy is also a clean and powerful hydrogen mass spectrometer. To clearly identify HD rotational Raman peaks, a minimum peak resolution of 5 Å is required. After calibrating with a known concentration of HD, it is possible to produce very sensitive tests of the presence of HD. Spectra shown in Fig.3.7 demonstrate the power in resolving a HD concentration to smaller than 1%. (The square-dotted curve is the spectrum of a high purity, converted D<sub>2</sub>, which has a smaller degree of HD contamination of 0.26%.)

Limited by the available power of the laser, this Raman spectroscopy technique requires

the pressure of the sample gas to be higher than roughly half an atmosphere to perform para-D<sub>2</sub> peak identifications in 40 minutes. The resolution of the para-D<sub>2</sub> peak is limited by the background count rate (ideally the dark count rate of the photon counting device). Our PMT has a nominal dark count rate of 5 Hz at room temperature, and with a para-D<sub>2</sub> peak count rate of 10 Hz it gives a relative uncertainty of

$$0.67 \frac{\sqrt{N_{pk} + N_{bg}}}{N_{pk} - N_{bg}} = 0.67 \frac{\sqrt{(10 + 5)t}}{(10 - 5)t} \quad (3.13)$$

of the para-D<sub>2</sub> peak amplitude. 30 seconds measurement gives a 10% relative uncertainty. Transformed into the high ortho-D<sub>2</sub> purity, assuming  $f_o + f_p = 1$ , a photon count rate of 1000 Hz under the ortho peak gives an absolute uncertainty of 0.15% in the knowledge of ortho-D<sub>2</sub> purity. Comparative count rates are now achieved with the 40 mW 488nm Ar<sup>+</sup> laser, the single grating spectrometer, the 488nm narrow band filter, and the 1/2'' PMT.

We fit the peak spectral shape with a single Gaussian function plus a constant level of background. We then use the total area of the Gaussian function for the para-D<sub>2</sub> fraction analysis and the peak width for a consistency check. The area uncertainty obtained from the fit is converted into the uncertainty of the para-D<sub>2</sub> fraction. The uncertainties listed here are of 90% confidence level. Moreover, the extraction of the para-D<sub>2</sub> fraction is based on the assumption of a full conversion of the room temperature D<sub>2</sub> reference sample. The fact that we use purified D<sub>2</sub> flowing through a hot (400 °C) palladium purifier, which is a highly active ortho/para catalyst, gives us some confidence in this assumption. The precision of the para-D<sub>2</sub> fraction is currently statistically limited by the signal to background ratio of the small para-D<sub>2</sub> peak of the converted sample. It can be improved with a higher D<sub>2</sub> gas pressure, a stronger laser source, or a cooled PMT to a level where the effect of ortho/para-D<sub>2</sub> relaxation in the optical cell becomes measurable.

As previously mentioned, this optical technique requires gas samples with pressure of several hundreds of Torr, and we can only collect D<sub>2</sub> vapor at this pressure from the boil-off of the condensed D<sub>2</sub> in the cryostat used as the UCN source. There are usually several hours of delay from the time of sample collection to the time of measurement. Therefore, we have to measure the relaxation rate of ortho to para-D<sub>2</sub> in the optical sample cell, which



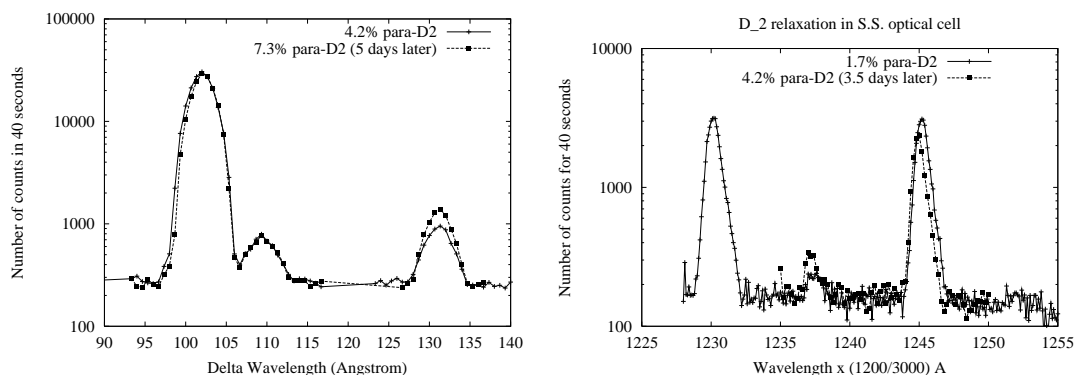


Figure 3.8: Relaxation in the Raman cell: The para-D<sub>2</sub> concentration grows from 4.2% (‘+’ set), converted at 23.6K, to 7.3% (dotted set) over a 5 day period.

has slightly magnetic S.S. surfaces, at ambient temperature. Fig.3.8 shows the observable relaxation over the course of 5 days. This corresponds to an increase of 0.3% of para-D<sub>2</sub> concentration overnight. Relaxation of ortho-D<sub>2</sub> introduces a correction within the measurement uncertainty, for samples measured a few hours after the collection. An inert optical cell will be required when the precision is improved.

To further improve the performance, we attempted to use a small double grating spectrometer, ISA model Gemini180, with a focal length of 18 cm. The spectra taken with it are shown in Fig.3.9. All the lines are preserved with a light throughput roughly a factor of two lower than the previous setup. The asymmetry of the peak shape needs to be corrected in order to perform measurements at better precision than the previous setup.

In conclusion, we have demonstrated here the technique of Raman spectroscopy to perform high precision measurements of the ortho-D<sub>2</sub> purity to 0.15%, using a low power visible laser and a normal grade spectrometer with an optimized light throughput. This provides us with the capability to cleanly determine the absolute para-D<sub>2</sub> and HD concentration. The fact that this technique requires almost no calibration makes it superior to a conventional scheme we discussed below.

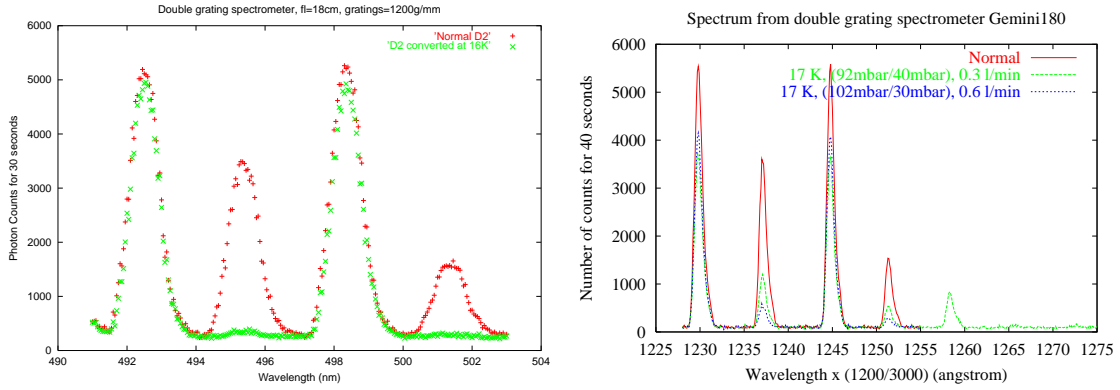


Figure 3.9: Raman spectrum taken with the double grating spectrometer

### 3.4.2 Thermal Conductivity Measurements – Hot Wire Method

#### Theory of Operation

This technique is an application of the traditional scheme for measuring the thermal conductivity of gas[47]. The hot wire method uses a thin metal wire as the heat source as well as the temperature sensor (through the linear temperature dependence of metal resistance). The supplied energy heats up the wire, and is conducted towards the cold walls of the cell through the surrounding media (in our case, D<sub>2</sub> gas). The rate of change as well as the ultimate temperature of the wire depend on the macroscopic thermal properties of the gas medium, and thus the voltage across the wire is expected to be sensitive to the concentration of para-D<sub>2</sub>.

When the mean free path is smaller than the dimension of the sample cell, the thermal conductivity  $\kappa$  depends on the specific heat,  $c_v$ ,

$$\kappa = \frac{1}{3} c_v \bar{v} l n. \quad (3.14)$$

Here the mean free path,  $l$ , is inversely proportional to the gas particle density,  $n$ , times the scattering cross section,  $\sigma$ . As a result, the thermal conductivity is independent of pressure in this medium pressure regime of molecular flow before the convection turns on at high pressure.<sup>3</sup> Convection can be reduced in a geometry of parallel plates, with the cost of a

<sup>3</sup>As a comparison, a Pirani pressure gauge has the same principle of operation, but is operated in a

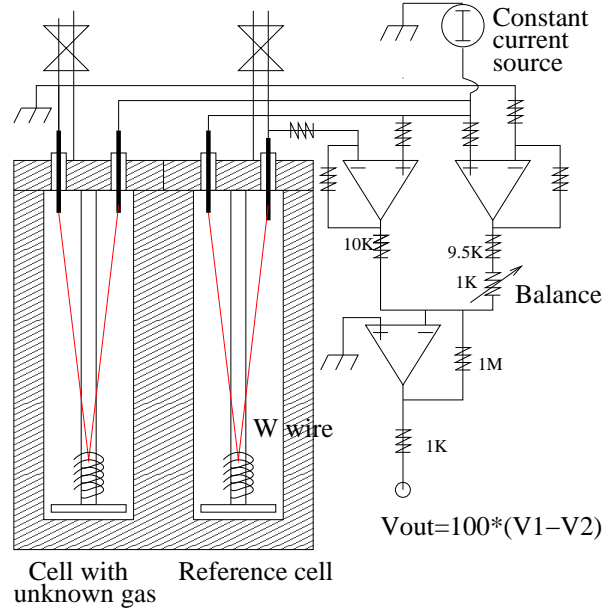


Figure 3.10: The thermal conductivity cell.

large thermal mass and thus, a slow response time[48]. As shown in tests, the measurements should be performed in the pressure range between 20 Torr to 100 Torr, where the thermal conductivity has the smallest pressure dependence.

### Design of a Hot Wire Cell

The thermal conductivity of ortho-D<sub>2</sub> and para-D<sub>2</sub> has a maximum 25% difference at a temperature of roughly 85 K, and a 8% difference at the temperature of roughly 120 K. This discrepancy in their thermal conductivity is large enough to be measured easily. A schematic in Fig.3.10 illustrates our hot wire measurement setup. We built two cylindrical cells with a 1" I.D. and a 5.5" height out of one rectangular cubic block of OFHC copper. Constantan conductor feedthroughs in ceramic insulator were used for the electrical leads. Tungsten pressure linear regime (low pressure), in which the mean free path is so long that gas particles carry away the heat directly to the cold surface without being scattered. As a result, the thermal conductivity is linearly dependent on pressure.

wires of 0.5 mm O.D. were used as the hot wires and were soldered to the constantan leads. The wires are slightly stretched by springs. The whole assembly was then immersed into a liquid N<sub>2</sub> bath to maintain a constant temperature on the outer cylindrical surfaces. <sup>4</sup>He was used as a reference gas in the reference cell, and D<sub>2</sub> at the same pressure (30 mbar) was filled into the other cell. Wires in these two cells were connected in series with the same current (100 mA) flowing through. The voltage across each wire was measured by an operational amplifier,  $\frac{1}{4}$ LF347, and the difference was amplified 100 times by a  $\frac{1}{4}$ LF347. This voltage was then read out with a standard multimeter with a precision of millivolts.

A material with a large resistivity is favored as a hot wire, because the sensitivity of the measurement scales with the size of the voltage signal. Platinum is an easy, affordable choice, which was widely used and cited in the literature[49]. However, its application as a hot wire in the hydrogen system is not advisable, because it is also known as an efficient ortho/para hydrogen catalyst. We followed the suggestion given in Ref. [50] to adopt tungsten, whose para-hydrogen conversion rate is 1/4 times that of platinum wire[37], but resistivity is three times lower. In addition, Ref.[48] reported a design of a copper circuit which is photo-etched as a thin 2.6 m long wire onto a hot plate. This avoids the catalytic wire problem and also has a fast response time.

## Results and Discussions

Fig.3.11 shows a set of hot wire voltage measurements on D<sub>2</sub> with varying para-D<sub>2</sub> concentration. The data is linear (sub-plot **a**) with approximately 10% scatter (sub-plot **b**). This scatter (due to systematic effects) sets the precision in the para-D<sub>2</sub> fraction to be  $(0.1 \times 4)/0.15 = 2.6\%$  (the maximum scatter of the data divided by the line slope). Also note that the HD contamination changes the slope of the voltage data set. This is consistent with HD at low temperatures having slightly larger specific heat and viscosity ( $\eta = \bar{v} l n/3$ ) than ortho-D<sub>2</sub>. A qualitative argument explaining the slope change is given by the following: <sup>4</sup>He's thermal conductivity is larger compared with that of HD (ortho- and para-D<sub>2</sub>)

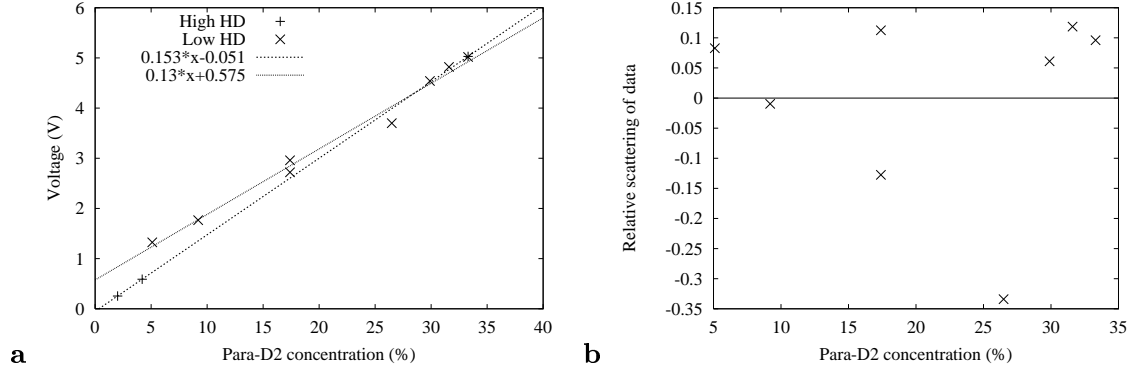


Figure 3.11: The performance of the hot wire cell. **a.** The ‘+’ data set is taken with a unpurified D<sub>2</sub> sample (with a high HD concentration of  $2.05\% \pm 0.16\%$ ) The knowledge of the para-D<sub>2</sub> concentration obtained from the Raman spectroscopy. The “x” set of data is taken with gas mixtures with known volume ratio of the converted D<sub>2</sub> at 17 K and the normal D<sub>2</sub>. HD contamination is approximately 0.3%. **b.** Scatter of data (“x” data set in **a**) in the voltage measurements.

because of its higher dynamic viscosity.<sup>4</sup> A higher HD concentration (ortho-D<sub>2</sub> fraction) results in a higher thermal conductivity of the sample gas, thus reducing the difference in thermal conductivity between the <sup>4</sup>He reference cell and the sample cell, resulting in a smaller voltage difference which is then recorded. The same reasoning applies to the ortho-D<sub>2</sub> (replace HD by D<sub>2</sub> in the above parentheses)<sup>5</sup> explaining the positive slope of the voltage measurement with increasing para-D<sub>2</sub> fraction. We also tested the stability of the hot wire cells by monitoring the converted D<sub>2</sub> over the course of 4 hours (Fig.3.12). One data set (“x”) shows a variation of 20%, while the other set shows a large drift in the voltage over time. Since these measurements were performed on the converted D<sub>2</sub>, which was flowing continuously out of the converter fixed at 17 K, we can not attribute this instability solely

<sup>4</sup>The viscosity scales with the mean velocity, and thus is inversely proportional to the square root of mass (for hydrogen isotope molecules). The small atomic size of <sup>4</sup>He gives a small cross section, and thus, a long mean free path.

<sup>5</sup>Ortho-D<sub>2</sub> has a higher thermal conductivity than para-D<sub>2</sub> because of its larger specific heat at low temperature, which is resulted from the available ground rotational state for thermal population.

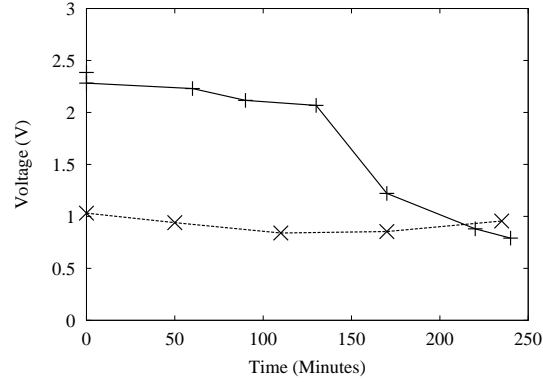


Figure 3.12: The stability in time of the converter and the measuring cell. Both sets of data are D<sub>2</sub> from a converter operated at 17 K. From the Raman spectroscopy measurement, the ‘+’ data set has an average para-D<sub>2</sub> concentration of  $1.54\% \pm 0.21\%$  and the HD concentration of  $1.2\% \pm 0.55\%$ , while the ‘x’ data set is taken with unpurified D<sub>2</sub> of an averaged para-D<sub>2</sub> concentration of  $1.42\% \pm 0.2\%$  and an HD impurity of  $0.26\% \pm 0.06\%$ .

to the hot wire cell performance. We will come back to this voltage drift in a later section.

Nevertheless, there is still room for improvement in the performance of the hot wire method. A power source with a feedback circuit which keeps the temperature of the wire constant would reduce the response time. A transient hot wire method has been investigated to measure the rate of temperature change, which is less sensitive to the effects of non-conductive heat transfer (radiation and convection) and heat leaks through the electrical leads[53, 54]. A higher precision of 0.6% was demonstrated using this transient hot wire method.

In conclusion, our static hot wire measurements were limited predominantly by electronic noise, and our method relies on frequent calibrations. Waiting for the output voltage to settle produced a response time of roughly 5 minutes. This technique also requires precise knowledge of the sample purity when analyzed as a binary gas mixture. A HD contamination at the level of 1% significantly shifts the overall thermal conductivity, and gives a spurious para-D<sub>2</sub> fraction of  $\sim 5\%$ . Nevertheless, it provides us with an easy, fast, *in-situ*, method for

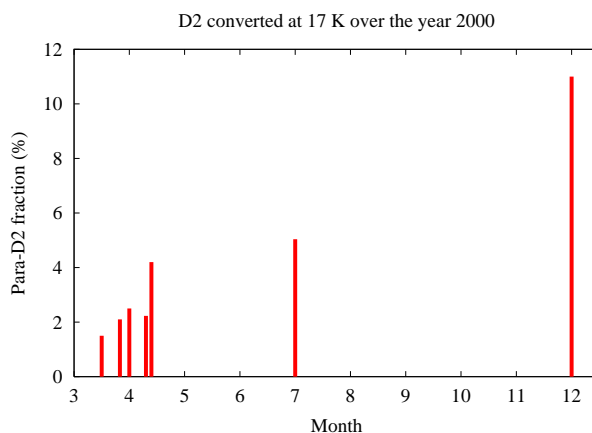


Figure 3.13: The performance of converter over a time course of 9 months during the on and off operations in the year 2000.

measuring the para-D<sub>2</sub> fraction to a few percent in low pressure (30 mbar) deuterium gas. Hence, this thermal conductivity cell permits us to continuously monitor and characterize the performance of the ortho/para-D<sub>2</sub> converter.

### 3.5 Discussions on the Converter Performance

With these tools to monitor the para-D<sub>2</sub> concentration, we studied the performance of the cryogenic converter using the catalyst, hydrous ferric oxide.

The best conversion achieved a  $1.4\% \pm 0.2\%$  para-D<sub>2</sub> concentration in the early stage of the experiments (with a converter temperature of 17K and the outlet pressure of the converter of around 35 mbar). As shown in Fig.3.13, the 17K converter produced converted D<sub>2</sub> gas with a para-D<sub>2</sub> fraction growing from 1.5% to 11% over the course of 9 months. This indicates that the catalyst became less efficient as time passed. The aging of the catalyst and the resulting deterioration of its catalytic ability is due to dehydration, which transforms the hydrous oxide gelatinoid into granules of micro oxide crystals, as explained in the previous discussion on catalysts. Regeneration of the catalyst by heating up the catalyst to 130°C under atmosphere was reported to restore the catalytic performance[43],

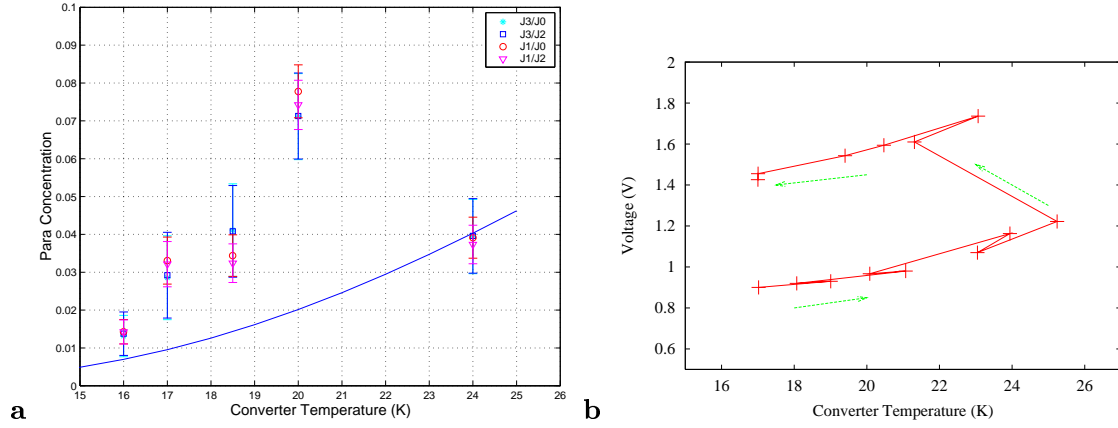


Figure 3.14: **(a)** The para-D<sub>2</sub> fraction of D<sub>2</sub> (measured with Raman spectroscopy) converted at different temperatures. **(b)** The hot wire voltage measurement of converted D<sub>2</sub> from converter operated at temperature from 17 K to 25 K. The arrows indicate the time order of measurements.

however, the total hours for regeneration were actually longer than the hours of operation in this experiment. Therefore, the obvious solution for maintaining the full efficiency is to replenish the converter with fresh catalyst.

Instabilities were also observed when we varied the converter operational parameters, such as temperature, pressure, flow rate, etc. As shown in Fig.3.14 (sub-plot **a**), the converted D<sub>2</sub> carries a higher para-D<sub>2</sub> fraction when converted below 20 K, and the thermal conductivity measurements (sub-plot **b**) indicate a transition of the physical state inside the converter at a temperature higher than 20 K. Fig.3.12 shows a drift in time of the hot wire cell measurements, which gives indirect evidence of a transition inside the converter. This leads us to ask the following questions: what is the physical phase of the D<sub>2</sub> inside the cell when the ortho/para conversion takes place, and what causes an incomplete conversion? A possible answer for the latter is the latent heat released from a D<sub>2</sub> phase transition inside the converter cell.

In order to reduce the para-D<sub>2</sub> fraction lower than 1%, the converter has to be cooled below 17 K, which is below the D<sub>2</sub> triple point temperature, 18.7 K. Thus, the operation



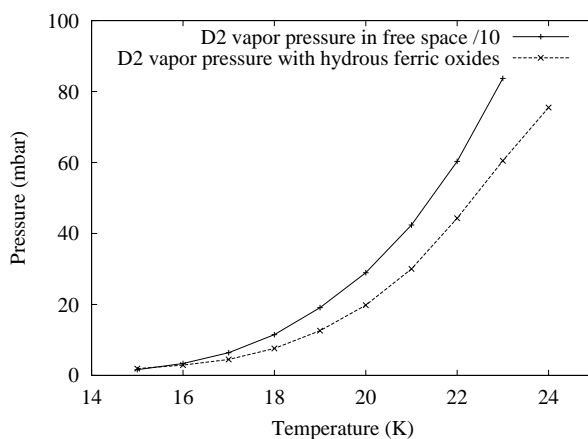


Figure 3.15: Vapor pressure of D<sub>2</sub> in an environment with catalyst, hydrous ferric oxide, compared with vapor pressure in the free space.

of this 1% para-D<sub>2</sub> converter is more difficult than a gaseous hydrogen converter. A large pressure (nominally a few hundred Torr) was supplied to the entrance of the converter to drive enough gas flow through the catalyst. In contrast, the outlet has a pressure of 35 mbar to sustain a moderate solid -D<sub>2</sub> growing rate ( $\sim 0.5$  liter of STP gas per minute). Thus, the D<sub>2</sub> gas experiences phase transitions inside the converter, where a large pressure gradient is present.

The large surface area of the catalyst introduces a large van der Waals field which adsorbs D<sub>2</sub> gas molecules. This adsorption is an essential first step of ortho/para-D<sub>2</sub> conversion via the paramagnetic mechanism. As a result, the phase diagram of D<sub>2</sub> in the converter is different than that of D<sub>2</sub> in free space. We measured the vapor pressure of D<sub>2</sub> in the presence of our catalyst, and observed that it is approximately 10 times lower than the vapor pressure of D<sub>2</sub> in free space (as shown in Fig.3.15) for a wide temperature range (15 – 25K). Noting this fact, we compared the conversion efficiencies when the D<sub>2</sub> pressure inside the converter was above or below the vapor pressure, which correspond to the condensed phase (liquid or solid) and gaseous phase, respectively. In table 3.1 we list the parameters and the resulting para-D<sub>2</sub> fraction,  $f_{para}$ , at a few temperatures we studied. At 17 K, the measured vapor pressure (4.5 mbar) is much lower than the nominal operating pressure (30 – 35 mbar);

T (K)	P <sub>in</sub>	P <sub>out</sub>	P <sub>vapor</sub>	flow rate (l/min)	$f_{para}^{meas.}$	$f_{para}^{theo.}$	$\Delta f / f^{theo.}$
17	92	40	4.5	0.3	0.16	0.01	15
17	102	30	4.5	0.6	0.051	0.01	4.1
21	168	115	30	0.5	0.18	0.025	6.2
21	60	18	30	0.2	0.077	0.025	2.1
22.5	190	111	50	0.5	0.074	0.0325	1.3
22.5	45	27	50	0.5	0.055	0.0325	0.7

Table 3.1: Ortho/para conversion with different parameters. The listed pressure readings are in mbar. The para-D<sub>2</sub> fraction is measured with Raman spectroscopy using the double grating spectrometer. The spectra are shown in Fig.3.9.

the condensed phase is thus expected to develop and cover the catalytic surface. This results in an incomplete ortho/para conversion of the outflow D<sub>2</sub>. The condensation also forms ice plugs, which generate a large flow impedance. We tested this hypothesis at higher temperatures of 21 K and 22.5 K, at which the empirical vapor pressures are 30 mbar (the canonical pressure for growing solid-D<sub>2</sub>) and 50 mbar, respectively. These measurements were conducted at the end of the 9 month period (depicted in Fig.3.13). As a result, none of the conversions gave expected populations of the excited para state. This is consistent with our use of an aged catalyst. Nevertheless, the manifest pressure dependence of para-D<sub>2</sub> conversion is very suggestive: conversion in the pure gaseous phase is more efficient than in the condensed phase. When condensation occurs, 50–80 mbar pressure gradient is present across the converter, whereas operations below the equilibrium vapor pressure exhibit less flow impedance and a smaller pressure gradient.

The possible existence of these phase transitions provides an insight into the disagreement between our low temperature conversion efficiency data and the theoretical predictions (in Fig.3.14), where all these data points were taken with outlet pressure somewhat above 30 mbar (the vapor pressure at 21 K) when the catalyst was still very effective. The latent heat released from the phase transition when condensing gas into liquid (or solid) provides

a source of energy that populates the  $J = 1$  rotational state (para state). The trend of an increasing deviation as temperature approaches the transition point, favors a phase transition model over a hypothesis which attributes the reduction of conversion efficiency to a reduction of the catalytic surface area. More latent heat is released around the triple point where the three phases coexist, and thus less D<sub>2</sub> completes the ortho/para conversion in the outflow. At 24 K with a vapor pressure of 76 mbar, the converter is operated purely in the gaseous phase, producing a fully converted product with the theoretical para-D<sub>2</sub> fraction. In addition, one might expect different D<sub>2</sub> phase diagram in the presence of catalyst with different degrees of aging.

In conclusion, even though the conversion condition in the converter is not yet fully under control, we have produced highly converted D<sub>2</sub> with a residual para state of 1.5%. This is done with a 100 c.c. converter filled with hydrous ferric oxide operated at 17 K, with a flow rate of roughly 0.5 liter/min. We developed an apparatus to monitor para-D<sub>2</sub> and HD contamination to a high precision. Our study of the functionality of the converter leads us to believe that regular replacement with fresh catalyst is the best way to ensure a full power of conversion and that ultimately a catalyst which does not largely reduce the D<sub>2</sub> vapor pressure is required to avoid complications associated with condensation.

## Chapter 4

# The S-D<sub>2</sub> UCN Source Experiment

From 1998 to 2000, we carried out a comprehensive set of experimental tests to study superthermal UCN production in solid deuterium. For these tests we built a prototype UCN source. Descriptions of this source as well as our experimental work using it are presented here. We focus primarily on measurements of the UCN residence time in solid deuterium, which sheds light on the limiting factors of UCN production. We have successfully verified the superthermal mechanism in this material, and also set the world record for UCN density using this test equipment.

### 4.1 Experimental Setup

We describe in this section the design and operation of the solid deuterium UCN prototype source.

#### 4.1.1 Cryostat Design

The cryostat which was used to contain and solidify deuterium has to provide enough cooling power to lower the temperature of the solid down to 5 K. It also has to endure radiation heating produced by the tungsten spallation target. The spallation target is designed to be placed closely to the solid deuterium, so that a high neutron flux can be used for UCN production. This assembly of deuterium cryostat (cooled by liquid <sup>4</sup>He) and

tungsten spallation target (cooled by liquid N<sub>2</sub>) is then placed into a neutron flux trap made of beryllium.

A schematic of the assembly is shown in Fig.4.1. For necessary thermal isolation, the assembly is placed in an aluminum vacuum chamber with a 38" O.D. and 33" height. Inside it, there is an inner 1.6" thick aluminum jacket which contains up to 25 liters of liquid N<sub>2</sub> coolant. The aluminum jacket is also the supporting structure for the stack of beryllium bricks used as the neutron trap, into which is embedded a block of 6.75"×6.75" × 2" tungsten as a spallation target. The heat deposited by protons onto this spallation target is conducted away through the Be bricks into the reservoir of liquid N<sub>2</sub>. There is one slab of 6.75"×6.75"× 1.6" polyethylene (PE) on top of the tungsten target, and there are four pieces of angled PE on the inner corners of the stack of Be bricks. PE is used as the neutron moderator, which thermalizes the spallation neutrons into cold neutrons.

The central 4K cryostat for the solid deuterium is built of an aluminum can, and it is inserted into the Be/PE stack. Inside the cooling jacket (which contains the liquid <sup>4</sup>He flow) is a polished S.S. cylindrical tube coated with <sup>58</sup>Ni on the inner wall and tightly surrounded by a cylindrical piece of PE. The bottom of the S.S. tube is closed by a <sup>58</sup>Ni coated S.S. plate. An additional thin PE disk (0.2" thick) is put outside the 4 K can, providing both further moderation of neutrons coming straight from the W target and radiation shielding from the spallation target. The entire lower part of the cryostat is wrapped in several layers of aluminized mylar (super insulation). The <sup>58</sup>Ni plated S.S. tube is the standard UCN guide tube (7.8 cm O.D.), provided by the Petersburg Nuclear Physics Institute (PNPI). It extends vertically out of the cryostat as the UCN guide, and connects to the bottle and detector system. Deuterium gas is filled into the guide system from the far end (just before the detector), and is cryopumped onto the other end of the guide, which is a part of the 4K cryostat. It solidifies into a block of solid deuterium with a volume of up to 1 liter. The inner 4K cryostat was later made smaller in order to grow the solid deuterium (up to a volume of 400 cm<sup>3</sup>) with a better defined geometrical shape.

Aluminum alloy type 6061-T6 is used extensively because it has high mechanical strength

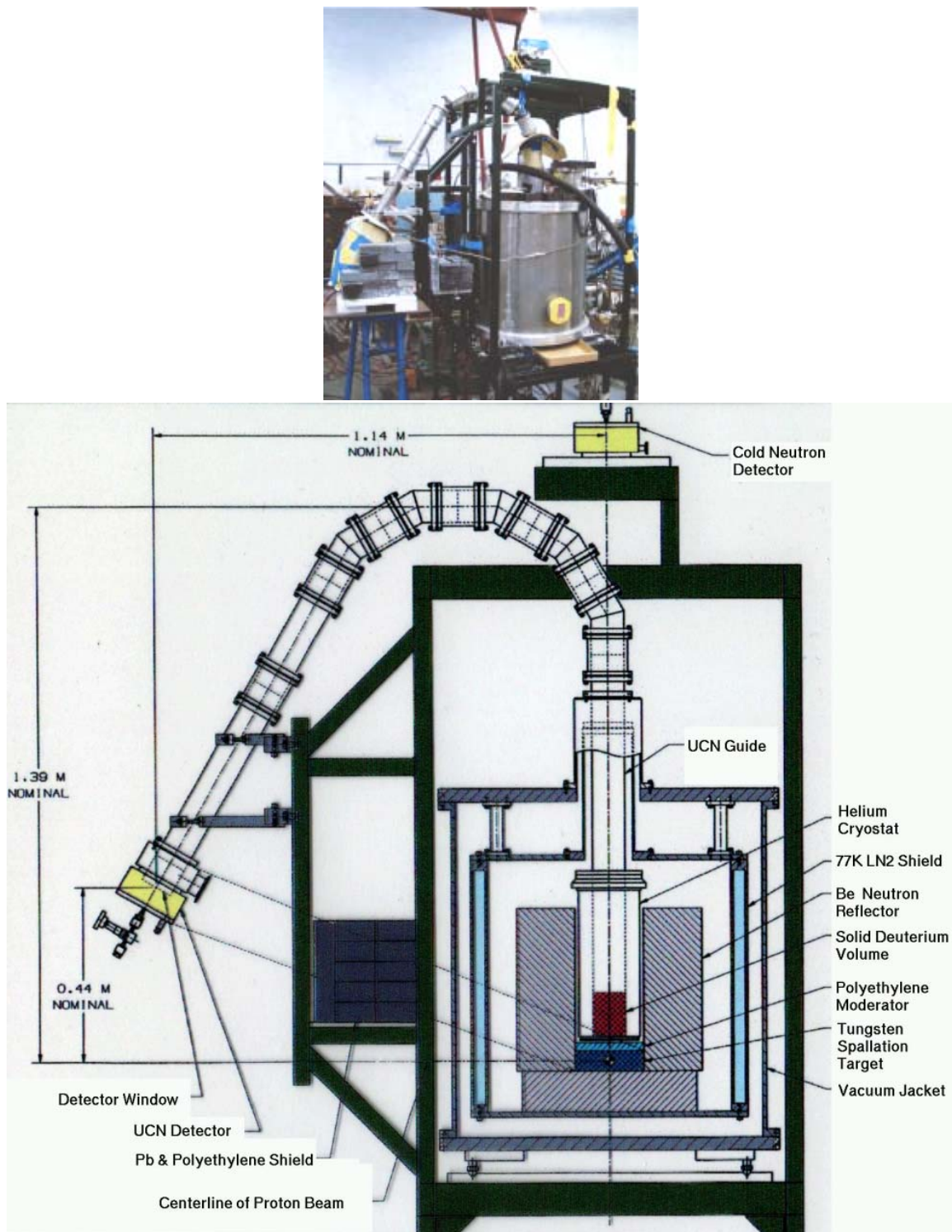


Figure 4.1: A picture and a schematic of the prototype UCN source.

and develops relatively little long-lived radioactivity in the intense neutron flux characteristic of our source.

### 4.1.2 Spallation Target

The spallation process refers to protons striking heavy nuclei, and creating high energy cascades inside the nucleus. High energy ( $\geq 20$  MeV) “secondary” particles escape the nucleus, leaving it in a highly excited state, which then relaxes primarily through emitting low energy “evaporation” neutrons. Compared with the fission process the spallation process is more efficient in creating neutrons. The average number of neutrons created in spallation is  $\sim 15$  per incident proton, much higher than the 2.5 per nuclear fission. About 180 MeV of energy is deposited in the reactor fission core per useful neutron produced, where as for spallation, the corresponding number is  $\sim 20$  MeV for an infinite lead target bombarded by 1 GeV protons. However, the spallation neutrons have higher energies than fission neutrons[92, 57].

Comparing the two common spallation targets, W and Pb, the multiplicity (neutrons per incident 800 MeV proton) for the Pb is 14.3, and for the W is 18.0 (12 from direct spallation, 6 from secondary (n,xn)-reactions). On the other hand, a Pb target is less easily activated, and thus, can be operated with roughly twice the proton current[63] as a W target to reach the same level of activation. However, Pb suffers from a low melting point, which eventually puts a limit on the size of the proton current. ( $Pb_{melt} = 601K$ ,  $W_{melt} = 3683K$ ).

### 4.1.3 Beryllium Neutron Flux Trap and Neutron Flux Amplifier

We designed a cold neutron flux trap using a beryllium neutron reflector to enhance the cold neutron flux in the location of the UCN converter[58]. A neutron is reflected multiple times inside the trap, which increases the time of interaction between the cold neutron and the solid deuterium, enhancing the probability of neutron downscattering. Beryllium is an ideal neutron reflector. It has a high effective neutron potential (see Table 4.1), and also a small neutron absorption cross section which minimizes the neutron flux attenuation. In

addition, it can amplify the neutron flux through the (n, 2n) reactions.

#### 4.1.4 Polyethylene Neutron Moderator

As discussed in chapter 2, hydrogen-rich materials are a favorable choice for neutron moderators. While other applications use water (heavy water, in cases where the nuclear absorption rate need to be reduced) or liquid hydrogen (liquid deuterium) as a thermal moderator, we use high density polyethylene, a plastic solid composed of long chains of (CH<sub>2</sub>)<sub>s</sub>. This choice also facilitates the prototype source construction, because PE is easy to machine and easier to implement than the cryogenic liquid alternatives.

We also developed a 4K and 77K PE scattering kernel using the complete full excitation spectrum of solid PE. They are incorporated as necessary input into a MCNP[59] simulation of the cold neutron flux. Good knowledge of the cold neutron flux is the first step towards a full Monte-Carlo simulation of the UCN production and the UCN transport/detection. The cryogenic PE scattering kernel is presented in appendix D.

#### 4.1.5 Heat Load and Thermometry

A MCNP simulation of the full geometry gives the heat load in different parts of the apparatus: The total heat load in the whole assembly is calculated to be  $\sim 185$  W per  $\mu$ A of protons. Most of the heat is deposited in the W spallation target ( $\sim 100$  W) and the Be neutron reflector ( $\sim 70$  W). With a heat of evaporation of 160 J/c.c. for liquid N<sub>2</sub>, the heat load in the W and Be will cause a boil-off of  $\sim 1$  cm<sup>3</sup>/sec of liquid N<sub>2</sub> per  $\mu$ A of protons.<sup>1</sup> The rest of the heat load (5W per  $\mu$ A of protons) is deposited in the 4K portion of the assembly cooled by liquid <sup>4</sup>He. The evaporation heat of 0.48 Jcm<sup>-3</sup> of liquid <sup>4</sup>He gives of a boil-off rate of roughly 10 cm<sup>3</sup>/sec of liquid helium for every  $\mu$ A of protons. The heat load into the 4K PE moderator is  $\sim 1$  mW per gram per  $\mu$ A of protons. The same heat load into the S-D<sub>2</sub>, with a specific heat of 25 mJ/g/K, induces a temperature rise in S-D<sub>2</sub> of approximately 0.04 K per  $\mu$ C of protons on target, which is well below the measurement

---

<sup>1</sup>One  $\mu$ C of protons corresponds to  $6.25 \times 10^{12}$  protons.



uncertainty of the temperature sensors.

It usually takes one full day of liquid nitrogen transfer and one full day of thermal conduction to cool the whole thermal mass of W/Be down to 100K. With this 77K heat shield it takes a few hours to cool down the 4K cryostat with <sup>4</sup>He at a rate of 50 liter/min. Note that liquid <sup>4</sup>He never accumulates in the cryostat. The temperature of the bottom UCN guide and the liquid helium cryostat is monitored by an array of silicon diodes, Lakeshore model DT-470, mounted on the guide wall and the aluminum cryostat wall. The measured temperature tracks the vapor pressure curve of S-D<sub>2</sub> at temperatures higher than 10 K. The temperature of the solid was obtained by averaging the temperatures of two diodes mounted on the outside of the guide wall. Off-line thermal tests using diodes embedded in the solid indicate these temperature measurements are accurate to 1K.

#### 4.1.6 UCN Guide and Bottle

Listed in table 4.1 are the scattering length, the density and the UCN critical velocity of different materials commonly used to construct UCN guides and bottles. <sup>58</sup>Ni has a large scattering length and a large number density. The combination of these properties gives it the highest UCN critical velocity. Carbon in the closely packed diamond structure is of great interest for polarization preserving applications, because of its small depolarization probability and high critical velocity.

We constructed our UCN guide and bottles with S.S. sectional guides coated with <sup>58</sup>Ni on the inner walls, to wherever possible. They are supplied by our PNPI collaborators. Some of the <sup>58</sup>Ni coated plates are prepared with the evaporation technique: Polished S.S. plates are pre-coated with 100 Å of chromium to provide enough adhesion for the subsequent Ni thin film with a thickness of a few thousand Å. Some parts of the guides and bottles are constructed using highly polished uncoated S.S.

The specularity of these guides and bottles directly affects the UCN transport. It influences the UCN transmission through guides and also modifies the filling and emptying time of a UCN bottle. A calibration test at the ILL revealed properties of our UCN

Material	$b_{coh}$ ( $10^{-12}$ cm)	$\rho$ (gm/cm <sup>3</sup> )	$v_{critical}$ (m/s)
Al	0.35	2.70	3.24
Al <sub>2</sub> O <sub>3</sub>	2.42	3.7	5.13
Be	0.774	1.8	6.89
BeO	1.35	3.02	6.99
C	0.665	1.80	5.47
C (graphite)	0.665	2.25	6.11
C (diamond)	0.665	3.25	7.65
Ni	1.03	8.9	6.84
<sup>58</sup> Ni	1.44	8.9	8.14
SiO <sub>2</sub> (glass)	1.58	2.3	4.26
Stainless Steel	0.86	8.03	6.00

Table 4.1: The critical velocity of different material used for the UCN guide.[27]

transport hardware[61]: the <sup>58</sup>Ni coated PNPI guides have a transmission fraction of 91% and a specularity of 97.5%. The loss factor is approximately 0.0005 per collision. The LANL S.S. UCN bottle has a wall loss lifetime of  $8 \pm 0.4$  seconds, corresponding to a loss per bounce of 0.002. The wall reflections in the bottle are approximately 84% specular.

#### 4.1.7 UCN Detector and Data Acquisition System

Neutrons are detected in a 5 cm thick multi-wire gas counter filled with a mixture of <sup>3</sup>He at 5 mbar and CF<sub>4</sub> at 1 bar. The neutron is detected through the nuclear absorption by <sup>3</sup>He + n → <sup>3</sup>H + p. The large recoil energy of the released proton and tritium ionize the CF<sub>4</sub> gas, which then causes a Townsend avalanche and produces a detectable current pulse. It is operated as a counting device. The detector entrance window is a 1 mm thick Al foil. The detector efficiency is discussed in Sec. 4.2.2. UCN counting data were acquired using a multi-scalar which was triggered by the proton beam signal through a toroidal current pick-up coil. The coil also measured the proton charge in order to scale the count rate from

the UCN detector.

## 4.2 Data Analysis

### 4.2.1 The Cold Neutron Spectrum

High energy neutrons are generated from the spallation target and then are subsequently moderated by the 77K/4K PE into cold neutrons and trapped in the Be trap. A small fraction of them are downscattered into UCN inside the solid deuterium, while the rest of the neutrons quickly leak out. To count these neutrons emerging from the cryostat, we used a cold neutron detector, which is the same multi-wire chamber as the UCN detector, but filled with 100 mbar of <sup>3</sup>He and 1 bar of CF<sub>4</sub>. It is placed outside of the vacuum chamber directly on top of the center of the assembly at a height of  $\sim 1.3$  meters above the solid deuterium (see Fig.4.1). The obtained neutron time-of-flight spectra (with and without the presence of the central block of solid deuterium) are shown in Fig.4.2 compared with the neutron spectrum calculated with a full LAHET (Los Alamos High Energy Transport)[60] and MCNP (Monte Carlo N Particle code)[59] simulation. LAHET calculate the high energy spallation process while MCNP calculates the thermal neutron moderation and the neutron transport. This Monte-Carlo analysis was carried out by one of our collaborator R. Hill. The neutron energy distribution can be elucidated from this time-of-flight spectrum, with an inherent uncertainty due to the neutron trapping time in the flux trap. The trapping time is calculated to be 133  $\mu$ s, which is a few times longer than the time of flight from the W target to the outside of the neutron trap, i.e.,

$$\begin{aligned} t^{30\text{ K}} &= \frac{40\text{cm}}{700\text{m/s}} = 0.57\text{ ms} \\ t^{300\text{ K}} &= \frac{40\text{cm}}{2200\text{m/s}} = 0.18\text{ ms.} \end{aligned} \tag{4.1}$$

We find that the energy distribution is consistent with 80% 35K and 20% 20K Maxwell-Boltzmann distributions[61, 76]. This verifies that neutrons are fully moderated by the polyethylene. A Monte-Carlo simulation shows that the cold neutron flux is highly vertically

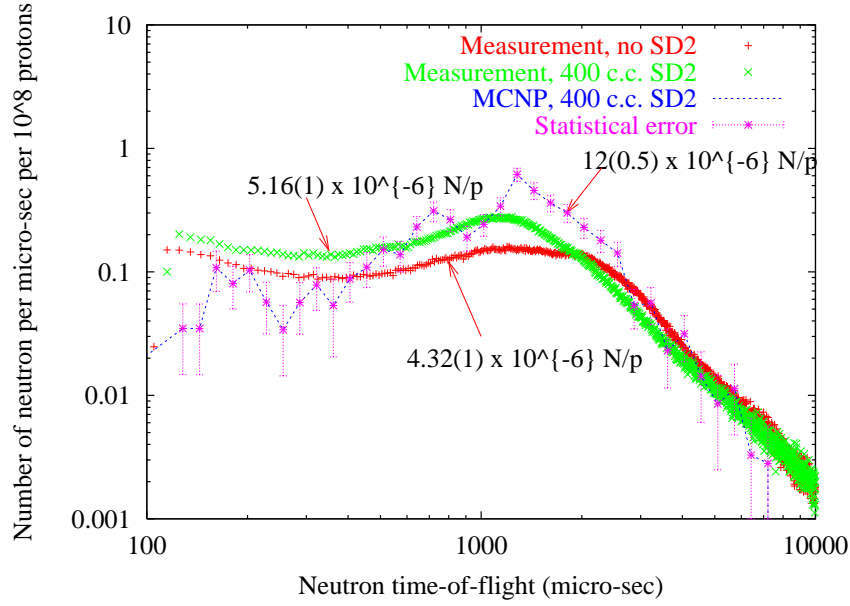


Figure 4.2: The cold neutron time-of-flight spectra compared with the MCNP simulation. The green curve is measured with 400 c.c. cryogenic solid deuterium, and the red curve is measured without the deuterium. The effect of the solid D<sub>2</sub> on the cold neutron spectrum is indistinguishable within our statistical limits[76].

directed by the trap geometry. There is a factor of 3 discrepancy in the number of cold neutrons entering the detector between the measurement and the Monte-Carlo simulation. A distortion of the angular distribution might account for this discrepancy. Nevertheless, with the current measurements of the cold neutron flux at only one angle, we cannot yet give a conclusive value for the absolute number of cold neutrons.

The measured neutron counts are converted into a cold neutron density of  $7.85 \times 10^5/\text{cm}^3\text{-}\mu\text{A}$ . This leads to a cold neutron flux of

$$\rho v_{\text{cold}} = (7.85 \times 10^5/\text{cm}^3) \times 700(\text{m/s}) = 5.5 \times 10^{10}/\text{cm}^2 \cdot \text{s} \quad (4.2)$$

in the solid deuterium for every  $\mu\text{A}$  of protons on the W target. We compare it with the following back-of-the-envelope estimate: The production rate of spallation neutrons is

$$P = 18 \times (6.25 \times 10^{12}) = 1.12 \times 10^{14} \quad (4.3)$$

for every  $\mu\text{A}$  of incident proton. The trapping time of the neutron trap is only  $130\mu\text{s}$ , and it limits the intensity of the neutron flux to

$$\frac{1}{4}\rho v = \frac{1}{4}\left(\frac{P\tau}{V_{trap}}\right)v = \frac{1}{4}\frac{(1.12 \times 10^{14} \text{ n/s}) \cdot (130 \mu\text{s})}{100 \text{ liter}} 700 \text{ m/s} = 2.5 \times 10^9 / \text{cm}^2 \cdot \text{s}. \quad (4.4)$$

This is smaller than the empirically derived number (Eq.(4.2)). Thus, it indicates that the effective volume for the neutron trap is smaller than the volume enclosed by the outer boundary of the Be bricks. If we take the trap volume as that enclosed by the PE moderator,  $\sim 10$  liters, we have a neutron flux of  $2.5 \times 10^{10} / \text{cm}^2 \cdot \text{sec}$ . Now the factor of two discrepancy can be attributed to the combined trapping and multiplying effects of the Be trap.

The above analysis suggests that an improved design of the neutron flux trap could leads to an enhancement to the cold neutron flux. A smaller opening in the Be trap would increase the cold neutron residence time, and a smaller trap volume would increase the cold neutron density. On the other hand, the nuclear absorptions from the internal hydrogenic material, which has an absorption length around 50 cm for pure liquid hydrogen, and 130 cm for Be, places a limit on the cold neutron trapping time in the trap:

$$\tau_{trap} = \frac{50 \text{ cm}}{700 \text{ m/s}} / f = 0.7 \text{ ms} / f \quad (4.5)$$

where  $f$  is the fraction of the volume occupied by hydrogenic materials in the total effective trap volume.

#### 4.2.2 The UCN Detection

One of our primary goals was simply to measure the number of UCN produced following a proton pulse of known total charge. Interpretation of our measurements was complicated, however, by a significant number of neutrons with energies slightly higher than UCN (VCN). This is especially true if we attempted to measure neutrons produced immediately after a proton pulse, because long storage times serve to clean all but UCN from the storage volume.

This problem arises because cold neutrons are downscattered into a continuous velocity spectrum of  $v^2 dv$ . After production, this spectrum is distorted by the velocity boost that the UCN encounter as they exit solid deuterium (which has a Fermi potential of 108 neV)

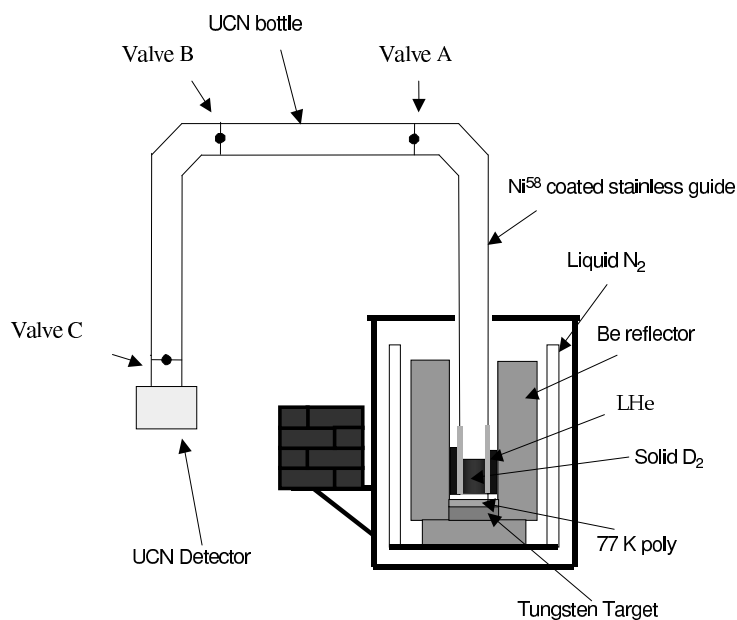


Figure 4.3: A schematic of our UCN run setup.

and by gravity, which red-shifts the potential as VCN and UCN follow the guides upward towards the bottle. These two influences on the spectrum largely cancel each other in our geometry. The experimental challenge for us was to demonstrate that the neutrons which survive the trip upward through the guides to our bottle were actually UCN.

At the exit of the storage bottle, UCN are guided downwards into the UCN detector. Gravity, in this case, accelerates UCN to high enough energies to penetrate through the aluminum detector window into the detection chamber, increasing the UCN detection efficiency.

Putting the neutrons through several 90° bends ensured several large angle collisions, helping to filter out VCN and neutrons with higher energies. Nevertheless, we tested the purity of the UCN signal from the detector with a <sup>58</sup>Ni coated plate, which is mounted on valve C right in front of the detector (see Fig. 4.3). The <sup>58</sup>Ni coated plate is a high pass filter which blocks UCN from reaching the detector. The measured time-of-flight spectra are shown in Fig. 4.4. With the filter in place, the UCN signal vanishes (green curve). This

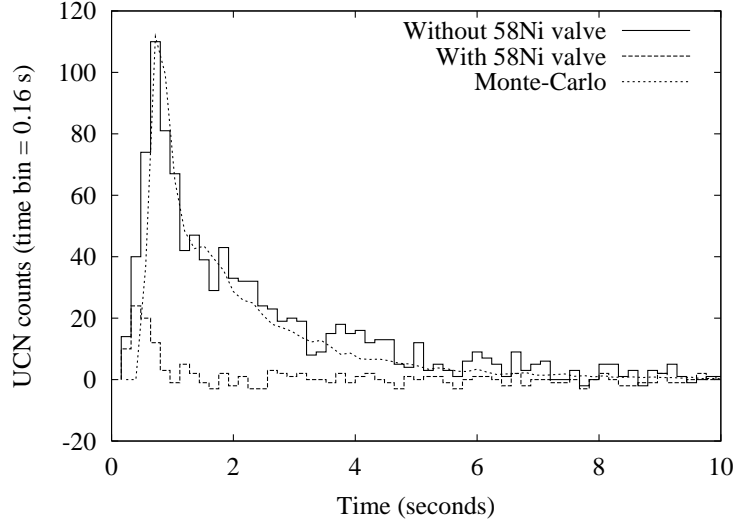


Figure 4.4: Time of flight spectrum.

confirms that the neutron counts registered in the UCN detector are indeed UCN signals. In fact, the residual counts ( $\sim 3\%$  of the total count without the UCN filter) are mainly due to the UCN leakage around the  $^{58}\text{Ni}$  valve. Also shown in the same plot is a Monte-Carlo simulated time-of-flight spectrum.

In order to reconstruct the number of produced UCN based on the detector signal, we studied both the UCN transport efficiency through the guide system and the detection efficiency of the UCN detector. The former was studied with two Monte-Carlo simulations: one uses a well-understood UCN source at ILL[61] and the other is developed to analyze our lifetime data[62]. The UCN transmission depends on the transport properties of the guides, as well as the physical configuration of the solid deuterium grown on the bottom of the cryostat. All our tests shows a UCN transmission fraction of  $\sim 70\%$  in our setup. The detector efficiency is a combination of the transmission fraction through the detector window, the chamber efficiency and the electronic efficiency. The first is estimated considering the transmission through the material potential barrier and the absorptive loss. For a UCN with velocity of 6 m/s and a velocity distribution given by our Monte-Carlo simulations, the transmission through the Al window is  $\sim 88\%$ , with losses dominated by the

nuclear absorption. The correction due to the small critical velocity of Al is negligible. The chamber efficiency was determined from the <sup>3</sup>He pressure: 5 mbar <sup>3</sup>He at room temperature corresponds to a number density of

$$\frac{P}{k_B T} = \frac{5 \times 10^{-3} \times 1.01 \times 10^5}{1.38 \times 10^{-23} \times 300} = 1.2 \times 10^{23}/m^3 = 1.2 \times 10^{17}/cm^3. \quad (4.6)$$

With a large <sup>3</sup>He nuclear absorption cross section (5333 barns for neutrons with a velocity of 2200 m/s), the neutron absorption length was

$$\frac{1}{n\sigma} = \frac{1}{(1.2 \times 10^{17})(5333 \times 10^{-24} \times 2200/6)}, = 4.3 \text{ cm}. \quad (4.7)$$

which leads to a detection efficiency of

$$1 - e^{-5/4.3} = 0.68. \quad (4.8)$$

in this 5 cm thick gas counter. UCN in the gas chamber can also be upscattered by the high pressure CF<sub>4</sub> gas before being absorbed by <sup>3</sup>He, without producing any detectable electronic signal. This effect is estimated to account for 0.08 of the total UCN annihilation events.

The electronic efficiency was measured by varying the discriminator threshold. The result of this linearity measurement is plotted in Fig.4.5. A nominal operation with a discriminating voltage of 50 V gives an efficiency of  $\sim 0.83$ .

In summary, the total efficiency of the detector system is  $0.68 \times 0.92 \times 0.83 = 0.52$ .

With our well-understood hardware monitoring the UCN produced, we independently varied each production parameter to systematically test the superthermal UCN production in solid deuterium. We describe a comprehensive set of such measurements in the following sections.

### 4.2.3 The Volume Dependence of UCN Production

The total UCN yield should scale with the amount of the source material, until the source becomes too large for UCN to leak out into the vacuum before they are absorbed or up-scattered in the source. The saturation size of the source is characterized by the UCN



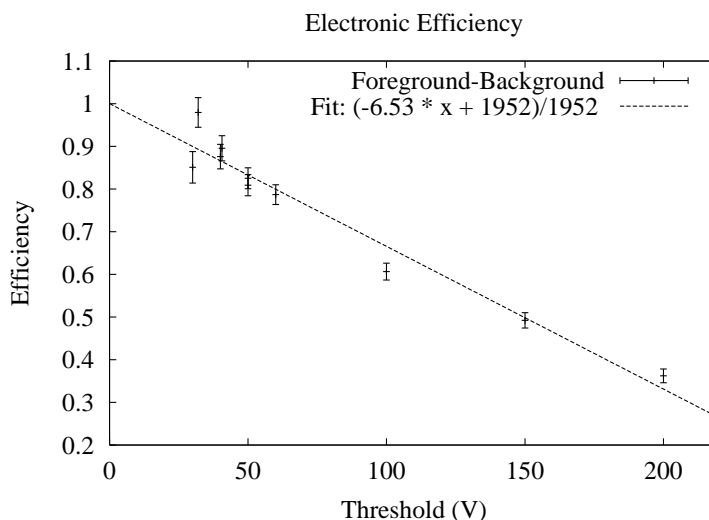


Figure 4.5: Electronic efficiency. Here shows the linearity of the detector response to the discriminator threshold.

mean free path within which the source is transparent to UCN. In large sources, only UCN produced in the top layer with a dimension of this mean free path can escape into the UCN guide. The mean free path of neutrons in a deuterium single crystal is the incoherent elastic scattering length,  $l_{inc}^{el}$ , with a value of

$$\frac{1}{n(4\pi b_{inc}^2)} = \frac{1}{(2 \times 3 \times 10^{22}) \times (2.04 \times 10^{-24})} = 8.2 \text{ cm}, \quad (4.9)$$

which is much shorter than its nuclear absorption length of 90 cm. Thus, UCN in a large block of S-D<sub>2</sub> experience elastic random walk and eventually are lost to nuclear absorption or upscattering. We do not consider the coherent scattering length because UCN do not have enough momentum for coherent Bragg scattering to redirect the UCN trajectories into Bragg angles. On the other hand, in a frozen block of solid D<sub>2</sub>, the neutron scatterings from macroscopic non-uniformities, such as the crystal boundaries, solid defects, and voids, might limit the actual UCN mean free path.

Fig.4.6 plots the volume dependence of the UCN production. The experimental data starts a turning over between 150 to 200 c.c. This volume corresponds to a height of 3 – 4 cm for a pancake shaped solid with a cross section of 50 cm<sup>2</sup>. To link the source dimension

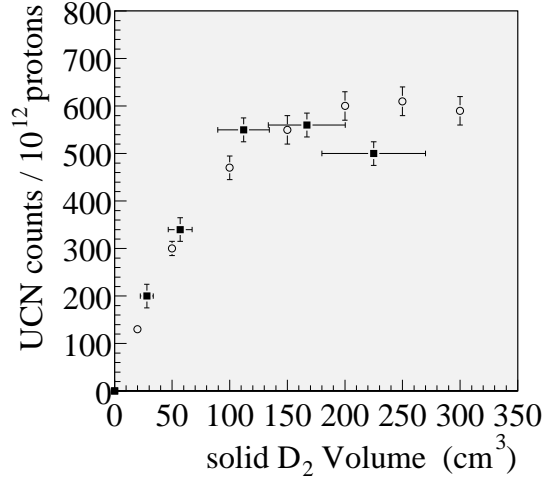


Figure 4.6: UCN production vs. S-D<sub>2</sub> volume. The experimental data (solid dots) is compared with the results of a Monte-Carlo simulation (hollow dots).

to the mean free path, we give a simple analysis: Because UCN are produced isotropically, the averaged vertical projection of their trajectory (before they are scattered) becomes

$$\begin{aligned}
 \overline{|z|} &= \frac{1}{4\pi} \int |r \cos \theta| d\phi \sin \theta d\theta \\
 &= r \frac{2\pi \cdot 2}{4\pi} \int_0^{\pi/2} \cos \theta \sin \theta d\theta = r/2.
 \end{aligned} \tag{4.10}$$

Here  $r$  is the total length of its trajectory. For UCN produced inside the source at a vertical distance  $z$  from the horizontal surface boundary to the vacuum, the averaged vertical projection of its trajectory is the probability-weighted sum of the upward flux and the downward flux which is then reflected upwards by the bottom plate. It is therefore just

$$\frac{1}{2}z + \frac{1}{2}((d - z) + d) = d, \tag{4.11}$$

which depends only on the height,  $d$ , of the source. As a result, all the neutrons inside the source have the same vertical projection of their trajectories, i.e.,  $\overline{|z|} = d = r/2$ , before they are scattered. The saturation dimension of a transparent UCN source, in which  $r = l_{inc}^{el}$ , is thus  $l_{inc}^{el}/2$ . Our measured value of 4 cm (with an uncertainty of 20%) is in a good agreement

with the above prediction using the incoherent elastic scattering length as the mean free path. This gives experimental evidence which supports the statement that macroscopic solid conditions do not significantly perturb the UCN wavefunction. For sources with a height larger than the half of the incoherent scattering length, the UCN yield starts to lose the reflected part from the flux initially directed downward, and thus, a decreasing number of output UCN are expected rather than a constant saturation. Moreover, a slightly reduced cold neutron flux at the higher part of the cryostat also results in a smaller UCN production in large sources.

#### 4.2.4 UCN Lifetime in Solid D<sub>2</sub>

The lifetime of UCN in solid D<sub>2</sub> limits UCN production. This is evident in the explicit formalism for UCN production:

$$N_{UCN} = V \times \rho_{UCN} = V \times (P \times \tau). \quad (4.12)$$

Here the source volume,  $V$ , is limited by incoherent elastic scattering, as discussed in the previous section; the UCN production rate,  $P$ , which is an intrinsic property of the solid deuterium, has a large value and makes S-D<sub>2</sub> a promising intense UCN source; the time of production,  $\tau$ , in this lossy source material cannot be longer than the UCN lifetime in S-D<sub>2</sub>, and this limits the intensity of the source. The lifetime, which is due to various loss mechanisms, is represented as

$$\tau_{SD_2} = \left( \frac{1}{\tau_{phonon}} + \frac{1}{\tau_{abs}(D)} + \frac{1}{\tau_{abs}(H)} + \frac{1}{\tau_{para}} \right)^{-1}. \quad (4.13)$$

The first term, which originates from phonon upscattering, has a distinctive temperature dependence, characterizing the superthermal performance of the phonon exchange process. The following two terms are the inevitable nuclear absorptions from the deuteron itself and the hydrogen impurity. The last contribution comes from the UCN upscattering caused by the para to ortho-D<sub>2</sub> spin flip, which was discussed in the previous chapter.

To determine the magnitude of these UCN loss mechanism and give a measure of the limiting lifetime, we measured the UCN lifetime in S-D<sub>2</sub> by trapping UCN in a bottle formed

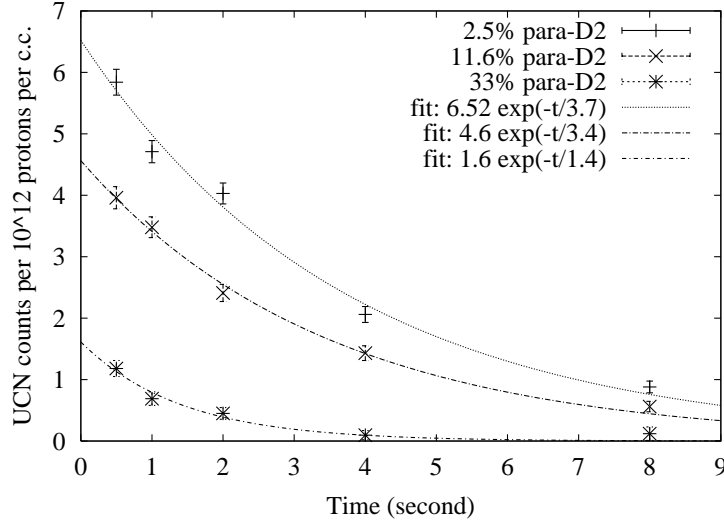


Figure 4.7: Decay curves of UCN in contact with solid deuterium with different para-D<sub>2</sub> concentrations.

by both the UCN guide section containing the solid deuterium and the valve A (see Fig. 4.3). Data were taken with S-D<sub>2</sub> volumes ranging from 12 to 300 cm<sup>3</sup>. UCN were produced and then stored in contact with the S-D<sub>2</sub> for a time,  $t_s$ . After  $t_s$ , the valve A was opened and the surviving UCN were detected. As shown in Fig. 4.4 essentially all UCN (greater than 90%) arrive in a 10s time window after the valve A is opened. Backgrounds were subtracted by fitting a linear function to the data between 20s and 65s after the proton trigger and extrapolating under the data in the UCN time window. The integral of the background-subtracted counts within the 10s window immediately after opening the valve A were then taken as the UCN signal for a given  $t_s$ . Lifetime were extracted by exponentially fitting the set of UCN signals for trapping times  $t_s$  of 0.5, 1, 2, 4 and 8 seconds. Plotted in Fig. 4.7 are typical decay curves. We then systematically varied the volume of S-D<sub>2</sub>, the temperature of the S-D<sub>2</sub> and the ortho/para ratio of the S-D<sub>2</sub> to produce families of experimentally determined lifetimes.

The measured lifetime is a function of the bottle lifetime,  $\tau_{bottle}$ , which characterizes the trapping time for UCN inside the bottle, and the source lifetime,  $\tau_{SD_2}$ , which represents the

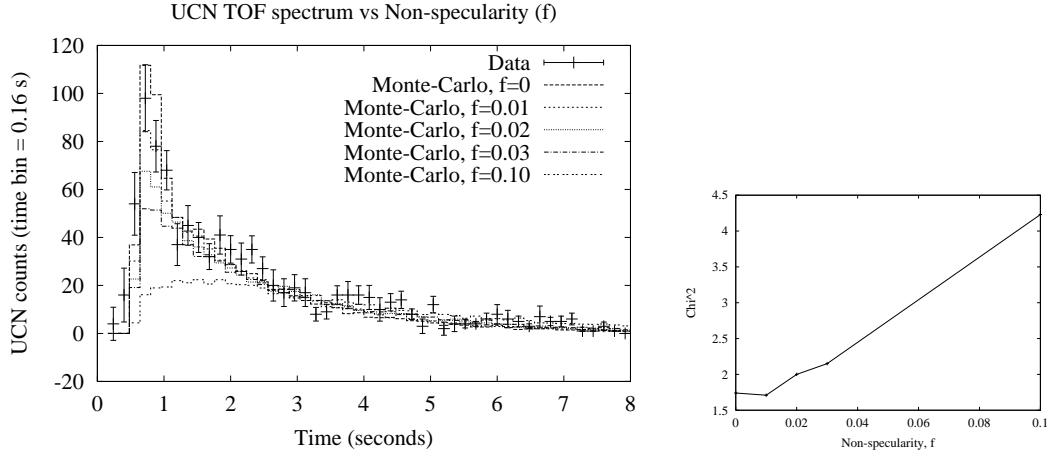
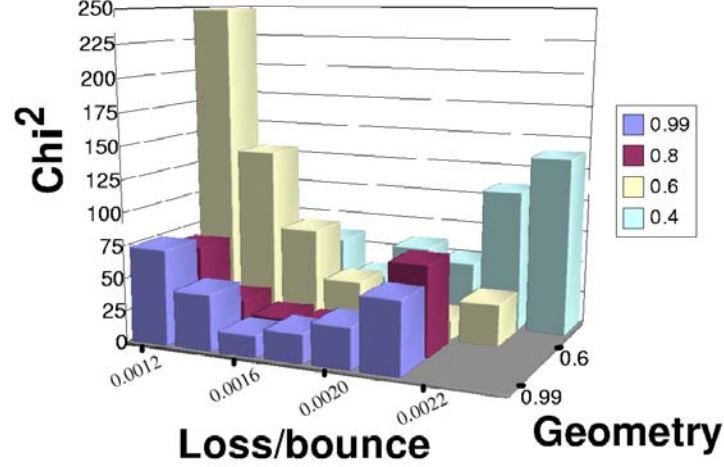


Figure 4.8: A measured UCN time-of-flight spectrum and Monte-Carlo simulated spectrum with different wall specularities.

UCN lifetime in the source material described in Eq. (4.13). The time for UCN to diffuse from the bottom source to the top of the bottle is  $\sim 0.5$  second, which is on the same scale as the varying UCN trapping times. Thus, it requires a detailed Monte-Carlo simulation to correctly account for the UCN transport in interpreting the lifetime data. Our collaborator C. Morris developed this Monte-Carlo transport code[62, 29]. In this transport code, the full experimental geometry, gravitation, the S-D<sub>2</sub> potential and wall collisions in the guide tube were taken into account.

The parameters which influence the measured lifetime are the source lifetime itself,  $\tau_{SD_2}$ , the probability of UCN loss every time it bounces off the wall surface, the specularity of the wall surface, the mean free path of UCN in S-D<sub>2</sub> and the physical shape of the S-D<sub>2</sub> grown in the cryostat. For small volumes of S-D<sub>2</sub> (few tens of c.c.), it is more likely to form a bucket-shaped film than the pancake geometry of our current cryostat. The effect of the source geometry can be described by a single parameter,  $r$ , which is the ratio of the S-D<sub>2</sub> volume in a uniform layer coating the walls to the pancake volume at the bottom.

The specularity of the guide was adjusted to fit the time-of-flight spectra as demon-

Figure 4.9:  $\chi^2$  minimization of the fit.

strated in Fig. 4.8.<sup>2</sup> Because thin samples of S-D<sub>2</sub> were used (0.4 cm or less) for most of the lifetime measurements, this measurement is quite insensitive to the mean free path of UCN inside the solid. The data for the larger volume indicates an mean free path of 8 cm as discussed in the previous session. Nevertheless, the extracted lifetime results change by less than 10% for a mean free path as small as 0.5 cm. We then performed a simultaneous fit of  $\tau_{SD_2}$ ,  $r$  and loss per bounce ( $f$ ) to reproduce the time-of-flight spectrum for all the measurements with all the S-D<sub>2</sub> volume for all the data below 10K. Data were subtracted from the Monte-Carlo time-of-flight spectrum given a set of parameters, and  $\chi^2$ 's were obtained. As demonstrated in Fig. 4.9, the best fit values are extracted at the minimum  $\chi^2$ , with a maximum deviation consistent with  $1\sigma$  variation for each independent parameter.

After combining these Monte-Carlo studies to the measurement,  $\tau_{SD_2}$  is extracted in a systematic way for all sets of data which have varying temperature and para-D<sub>2</sub> fraction. The dependence of  $\tau_{SD_2}$  on the temperature from 5 to 12 K is plotted in Fig.4.10, where

<sup>2</sup>Parameters relating the properties of the UCN guide, such as the probability of UCN loss per bounce from the wall, and the specularity of the wall, are the same as long as no new parts are added in (we frequently altered our hardware in this test and developmentstage).

data were taken with deuterium with a para-D<sub>2</sub> concentration of 2.5%. Taking into account the UCN upscattering by the D<sub>2</sub> vapor at higher temperatures, the data tracks well with the theoretical curve throughout the whole temperature range. The dependence of  $\tau_{SD_2}$  on the para-D<sub>2</sub> fraction is plotted in Fig. 4.10 for all the data with temperature below 6.6 K. Data taken with various volumes of S-D<sub>2</sub> from the tests carried out throughout the year of 2000 are included in the same plot (Fig. 4.10), and are fit to a curve with a single parameter. The fit parameter gives a UCN lifetime due to para-D<sub>2</sub> upscattering of  $1.2 \pm 0.2$  ms, consistent with the theoretical calculation of 1.5 ms.

The uncertainty at the 20% level of the deduced para-D<sub>2</sub> upscattering time, is consistent with the scatter of the data, which reflects our limited ability to control systematic uncertainties: the ortho/para ratio, the volume of S-D<sub>2</sub> and the temperature measurements.

#### 4.2.5 Stored UCN – World Record

The ultimate goal of this source development project was to demonstrate a high UCN density in a storage bottle. We achieved this with a pseudo-bottle constructed out of a 73 cm section of highly polished, uncoated S.S. UCN guide with valves (the butterfly valve A and B in the schematic of Fig. 4.3) on both ends. The valves are pneumatically operated butterfly valves made of S.S. flat plate. This UCN lifetime in this bottle was measured to be  $13 \pm 1$  seconds, which is relatively short because of the large leakage through the gap between the valve plate and the inner surface of the guide tube. The nominal trapping scheme is described as follows: first, fill the bottle with the entrance valve (valve A) open and the exit valve (valve B) closed for the duration of the proton pulse plus an additional 0.5 seconds to account for the delayed UCN arrival. Valve A is then closed to keep UCN from draining back to the lossy source. UCN are stored in the bottle for a varying trapping time. At the end of this time, valve B is opened, the bottle is emptied, and UCN are counted in the UCN detector. A typical spectrum showing the time structure is plotted in Fig. 4.11. In this run, a series of eight pulses of protons were fired at the target in the first 1 seconds, during which the bottle is filled. After the UCN arrive (0.5s later) it is closed, and UCN is

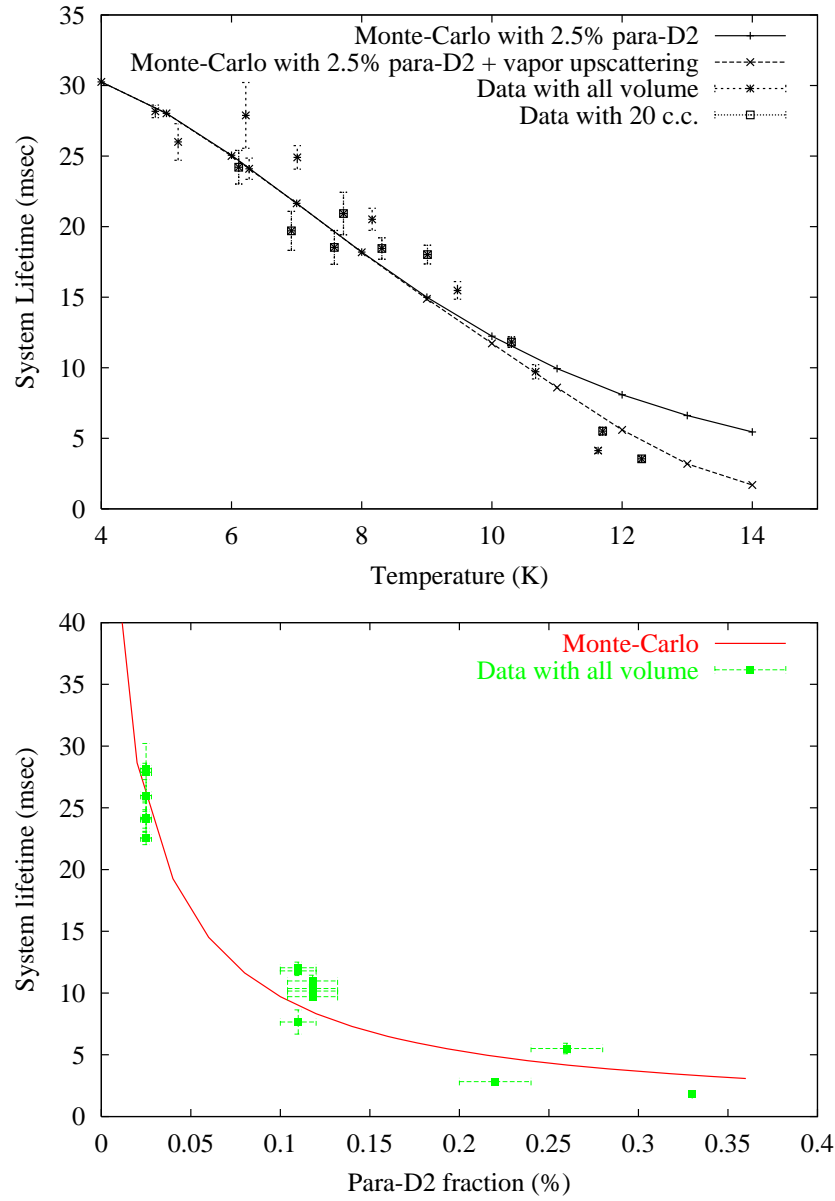


Figure 4.10: UCN lifetime dependence on the solid temperature and the para-D<sub>2</sub> fraction.[29]



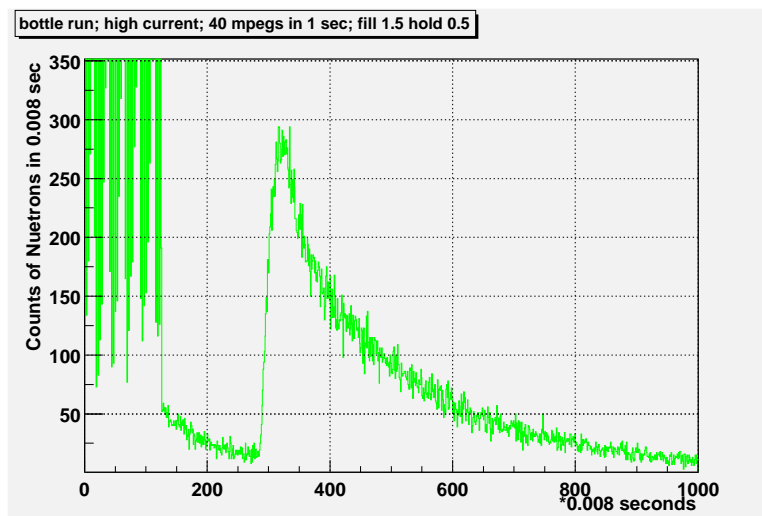


Figure 4.11: A TOF spectrum for the UCN bottle run.

stored for 0.5 seconds and then emptied into the detector, resulting in a significant peak in the UCN count. Again the rise time of the peak is delayed by the UCN time-of-flight from the exit of the bottle to the detector, showing the characteristic low velocity of UCN. In this spectrum the finite, non-zero UCN count before the valve B is opened indicates that the bottle used for this test suffers a big UCN leakage around the valves.

Corrected by the UCN transport efficiency and the detection efficiency, the integral neutron counts in the detector are converted into the total number of UCN stored in the bottle. Dividing this UCN number by the volume of bottle, 3640 cm<sup>3</sup>, we obtained the UCN density stored in the bottle at the end of the trapping period. With this prototype source, not yet optimized, we managed to trap in a leaky S.S. bottle 1 UCN/cm<sup>3</sup> for every 1  $\mu$ C of protons on target (see Fig.4.12).

It is of practical interest to test the linearity of the relationship between UCN production and the amount of protons. In principle, the production rate scales with the cold neutron flux, which is linearly dependent on the total proton charge at the spallation target. The fundamental limitation, however, comes from the warming of the S-D<sub>2</sub> caused by the fast particles produced in the spallation process. There is some evidence for the non-linear trend

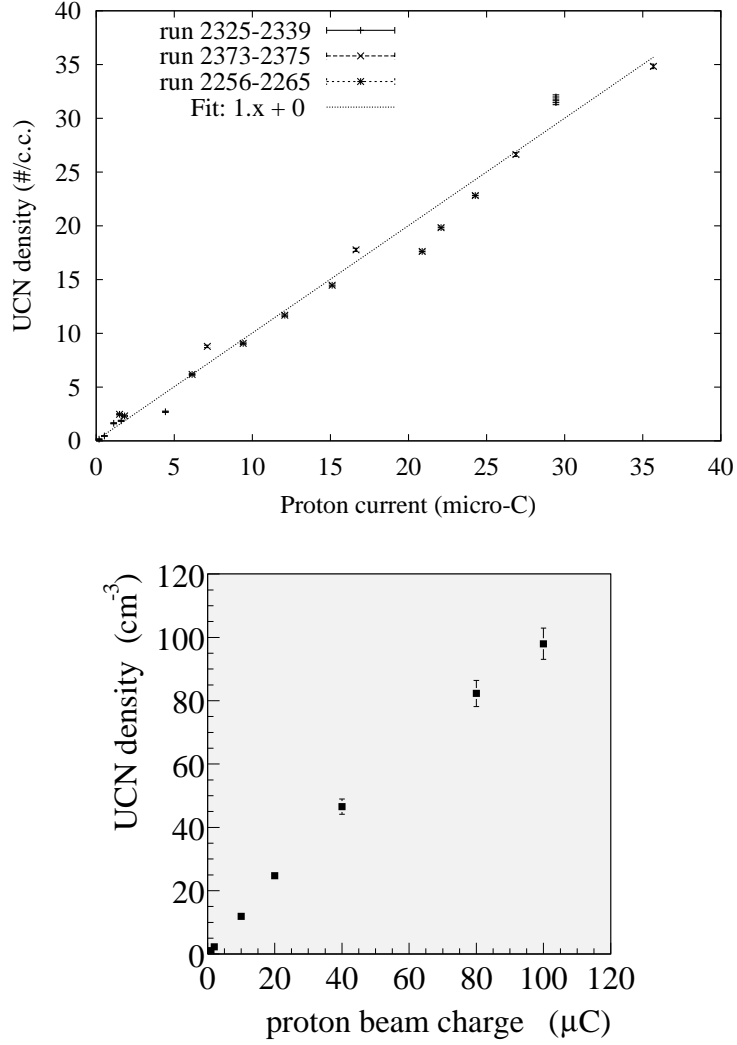


Figure 4.12: Stored UCN density in the S.S. bottle. The dependence of UCN production on the proton current. The volume of S-D<sub>2</sub> is approximately 200 c.c. and the para-D<sub>2</sub> fraction in the source is approximately 6%, with a 0.2% HD contamination.

in the slight fall off at high beam charges (see Fig. 4.12). However, no drastic decrease in UCN production has been found up to 100  $\mu\text{C}$ . With high total proton charges, the temperature sensors registered an increase of up to 2 K in the cryostat temperature right after the proton pulse. The fast temperature rise indicates that the heat load is associated with the spallation induced heating. We may well have approached the cooling limit of the cryogenic design of this prototype. The highest density measured in this experiment was  $98 \pm 5 \text{ cm}^{-3}$  in this 3.6 liter S.S. bottle using a 200  $\text{cm}^3$  of S-D<sub>2</sub> with a contamination of 6% para-D<sub>2</sub>.

It is worth mentioning that 41  $\text{cm}^{-3}$  was the highest previously obtained UCN density[64]. This value was measured with a S.S. bottle coupled to the UCN source at the ILL high flux research reactor. The fact that our small prototype source sets a new density record underlines this great potential of the new method of UCN production.

## Chapter 5

# Solid Oxygen as a Superthermal Source

Spin waves, or magnons, in the anti-ferromagnetic  $\alpha$  phase of solid oxygen (S-O<sub>2</sub>) provide a novel mechanism for ultra-cold neutron (UCN) production. Like phonons in solid deuterium superthermal sources, magnons in solid  $\alpha$ -oxygen dominate the energy exchange mechanisms for cold neutrons and UCN. We present in this chapter calculations of UCN production and upscattering rates in S-O<sub>2</sub>. The results indicate that S-O<sub>2</sub> as potentially a very effective UCN source material.

### 5.1 Introduction

Solid  $\alpha$ -<sup>16</sup>O<sub>2</sub> has manifest magnetic properties. Its related ability to interact with cold neutrons and UCN, through neutron-magnon inelastic scattering, provides potential advantages which stem from the dispersion relation of its anti-ferromagnetic magnons. In fact, the large neutron-magnon inelastic scattering rate together with oxygen's small nuclear absorption cross section suggest that a S-O<sub>2</sub> UCN source may well compete favorably with the solid deuterium UCN source.

Non-metallic solid  $\alpha$ -<sup>16</sup>O<sub>2</sub> has a two dimensional anti-ferromagnetic structure which

exhibits spin wave excitations[68, 70]. Its magnetism originates from one of the unpaired  $2p$  electrons from each oxygen atom, which align to form a molecular electronic ground state  $^3\Sigma_g^-$  with a net spin of one ( $S = 1$ ) and an orbital angular momentum of zero ( $l = 0$ ). We will concentrate on the most abundant isotope  $^{16}\text{O}$ , which has a null nuclear spin, and thus only odd rotational states are present in the molecular energy spectrum[46]. The characteristic absence of half of the rotational states is a strong advantage of S-O<sub>2</sub> as a UCN source, as will be discussed below.

At low temperatures ( $T < 23.9\text{K}$ ), long range anti-ferromagnetic ordering is established and the lattice structure slightly distorts from a rhombohedral to a monoclinic symmetry through the transition from  $\beta$  to  $\alpha$  phase. For the UCN work, we will be concerned with S-O<sub>2</sub> in the  $\alpha$ -phase below 10K, where the superthermal UCN production is possible.

## 5.2 Neutron-Magnon Scattering Theory

### 5.2.1 Magnetic Scattering Length

The coupling of neutrons to magnons in S-O<sub>2</sub> originates from the non-zero neutron magnetic moment interacting with the magnetic field generated by the unpaired molecular electrons. This spin-spin magnetic coupling has an intrinsic scattering length of 5.4 fm[33], which is comparable to the scattering length associated with the strong interaction for neutron-phonon scattering.

The complete expression for the double differential magnetic neutron scattering cross-section is (for a fixed orientation between the initial momentum vector  $\vec{k}_i$  with respect to the crystal axes, specified by the angular variables  $\Omega_i$ ):

$$\begin{aligned}
 \left( \frac{d^2\sigma}{d\Omega_f d\epsilon} \right) &= \frac{k_f}{k_i} |\langle k_f \lambda_f | V | k_i \lambda_i \rangle|^2 \delta(\hbar\omega + E_{\lambda'} - E_{\lambda}) \\
 &= \left( \frac{m_n}{2\pi\hbar^2} \right)^2 (2\gamma\mu_N\mu_B)^2 (4\pi)^2 \frac{k_f}{k_i} \sum_{\lambda_i \lambda_f \sigma_i \sigma_f} p_{\lambda_i} p_{\sigma_i} \\
 &\quad \times |\langle \lambda_i \sigma_i | \hat{\sigma}_i \cdot \hat{Q} | \lambda_f \sigma_f \rangle|^2 \delta(\hbar\omega + \Delta E) \\
 &= r_0^2 \frac{k_f}{k_i} \mathbb{S}(\vec{\kappa}, \omega),
 \end{aligned}$$

where  $\hat{Q}$  relates the electronic spin  $\hat{s}$  and the neutron momentum transfer  $\vec{\kappa} = \vec{k}_f - \vec{k}_i$  through

$$\hat{Q} = \sum_i e^{i\kappa \cdot r_i} \tilde{\kappa} \times (\hat{s}_i \times \tilde{\kappa}). \quad (5.1)$$

Here  $\Omega_f$  is the solid angle for  $k_f$ ;  $\lambda_i$  and  $\lambda_f$  are the initial and final states of the oxygen molecule;  $\sigma_i$  and  $\sigma_f$  are the initial and final neutron spins.

The double differential cross-section is usually decomposed into the product of an effective magnetic scattering length  $r_0$ , the kinematical factor,  $\frac{k_f}{k_i}$ , and the scattering law  $\mathbb{S}(\kappa, \omega)$  [71] with units of [1/Energy]. Essentially all of the specific details of the scattering process are swept into  $\mathbb{S}(\kappa, \omega)$  which contains a full description of the physics of the neutron interaction with S-O<sub>2</sub>. The magnitude of the scattering length,  $r_0$  is

$$\begin{aligned} r_0 &= \frac{m_n}{2\pi\hbar^2} \cdot 2\gamma\mu_N\mu_B \cdot 4\pi \\ &= \frac{m_n}{2\pi\hbar^2} \cdot 2\gamma \frac{e\hbar}{2m_p c} \frac{e\hbar}{2m_e c} \cdot 4\pi = \gamma \frac{e^2}{m_e c^2}, \end{aligned}$$

a product of the gyro-magnetic ratio  $\gamma=-1.91$  of neutron, and the classical electron radius 2.82 fm, which is obtained from  $\frac{e^2}{r} = m_e c^2$ .

### 5.2.2 Treatment of Coherent Scattering

Before presenting the scattering law  $\mathbb{S}(\kappa, \omega)$  of magnetic scattering in S-O<sub>2</sub>, we present our approach to calculating the pure coherent scattering cross-sections. To evaluate the overall scattering strength, one needs to perform an integration of the double differential cross-section of the appropriate scattering kernel,  $\mathbb{S}(\vec{\kappa}, \omega)$ .

$$\begin{aligned} \frac{d^2\sigma}{d\Omega d\epsilon} &= r_0^2 \frac{k_f}{k_i} \mathbb{S}(\vec{\kappa}, \omega) \\ \sigma^{tot}(E_i, \Omega_i) &= r_0^2 \int_0^\infty dE_f \int d\Omega_f \frac{k_f}{k_i} \mathbb{S}(\vec{\kappa}, \omega). \end{aligned} \quad (5.2)$$

The coordinate transformation from  $(\Omega, E_f)$  to  $(\vec{\kappa}, \omega) = (\phi, \kappa, \omega)$  facilitates the above

integration,

$$\begin{cases} \omega &= E_i - E_f \\ \kappa &= \sqrt{k_f^2 + k_i^2 - 2k_f k_i \cos\theta} \\ &= \sqrt{\frac{2m}{\hbar^2}} \sqrt{E_f + E_i - 2\sqrt{E_f E_i} \mu}. \end{cases}$$

and implies that

$$d\Omega dE_f = (d\phi d\mu) dE_f = d\phi \left( \frac{\kappa}{k_f k_i} d\omega d\kappa \right). \quad (5.3)$$

The energy transfer  $\omega$  can be interpreted as the magnon energy gain, and  $\kappa$  the magnitude of neutron momentum transfer. This yields the total neutron scattering cross-section involving single energy quanta:

$$\sigma^{tot}(E_i, \Omega_i) = r_0^2 \iint d\omega d\kappa d\phi \frac{\kappa}{k_f k_i} \frac{k_f}{k_i} \mathbb{S}(\vec{\kappa}, \omega) \quad (5.4)$$

which can be further reduced to

$$\sigma^{tot}(E_i) = 4\pi r_0^2 \frac{\hbar^2}{2mE_i} \int_{-E_{BZ}}^{\min(E_i, E_{BZ})} d\omega \int_{\kappa_{lower}}^{\kappa_{upper}} d\kappa \kappa \mathcal{S}(\kappa, \omega). \quad (5.5)$$

The energy quanta for neutron energy transfer,  $\omega$ , have a maximum energy of excitation at the Brillouin zone (BZ) boundary  $E_{BZ}$ , as a nominal phenomena in a periodic structure. Note that we define a reduced scattering law,  $\mathcal{S}(\kappa, \omega)$ , by implicitly orientationally averaging in the incident angle  $\Omega_i$ , i.e.,

$$\mathcal{S}(\kappa, \omega) = \frac{1}{4\pi} \int d\Omega_i \mathbb{S}(\vec{\kappa}, \omega). \quad (5.6)$$

This orientation independent scattering law  $\mathcal{S}(\kappa, \omega)$ , however, does not imply the application of the widely used incoherent approximation, in which the constraint of a single excited energy quantum propagating in a well-defined direction is relaxed. We simply take the integration over the incident angle in advance, which is appropriate in the case of a neutron beam scattering from a polycrystal, a  $4\pi$  incident neutron flux, or a combination of both. We emphasize that the detailed energy and momentum conservation laws are strictly followed in every step of our treatment of coherent scattering.

The ranges of integration in Eq.(5.5) are easily set by the kinematics of the scattering process. The range of possible values for  $\kappa$  is bounded by  $(\kappa_{lower}, \kappa_{upper})$ . For a given magnitude of energy transfer and initial energy of the neutron:

$$\begin{aligned}\kappa^2 &\geq \frac{2m}{\hbar^2}(E_f + E_i - 2\sqrt{E_f E_i}) \equiv \kappa_{lower}^2 \\ \kappa^2 &\leq \frac{2m}{\hbar^2}(E_f + E_i + 2\sqrt{E_f E_i}) \equiv \kappa_{upper}^2 \\ |\kappa_{lower}| &= \sqrt{\frac{2m}{\hbar^2}} \left| \sqrt{E_i - \omega} - \sqrt{E_i} \right| \\ |\kappa_{upper}| &= \sqrt{\frac{2m}{\hbar^2}} (\sqrt{E_i - \omega} + \sqrt{E_i}),\end{aligned}$$

The integration in Eq.(5.5) is numerically approximated by a sum over all kinematically accessible points on a grid of the phase space[70]. This gives the neutron downscattering ( $\sigma_{down}^{tot}$ ) and upscattering cross sections ( $\sigma_{up}^{tot}$ ):

$$\begin{aligned}\sigma_{down}^{tot}(E_i) &\cong 4\pi r_0^2 \frac{\hbar^2}{2mE_i} \sum_{l(\omega_l > 0)}^{l(\omega_l = \min(E_i, E_{BZ}))} \Delta\omega_i \\ &\times \sum_{m(\kappa_m = \kappa_{lower})}^{m(\kappa_m = \kappa_{upper})} \Delta\kappa_m \kappa_m \mathcal{S}(\kappa_m, \omega_l) \\ \sigma_{up}^{tot}(E_i) &\cong 4\pi r_0^2 \frac{\hbar^2}{2mE_i} \sum_{l(\omega_l > 0)}^{l(\omega_l = E_{BZ})} \Delta\omega_i \\ &\times \sum_{m(\kappa_m = \kappa_{lower})}^{m(\kappa_m = \kappa_{upper})} \Delta\kappa_m \kappa_m \mathcal{S}(\kappa_m, -\omega_l).\end{aligned}\tag{5.7}$$

A table of scattering laws,  $\mathcal{S}(\kappa, \omega)$ , can be prepared given the complete dispersion relation  $E(\vec{\kappa})$  of energy quanta excitations: With the vector  $\vec{\kappa} = (\kappa \sin \theta \cos \phi, \kappa \sin \theta \sin \phi, \kappa \cos \theta)$  specified by randomly assign an orientation  $(\theta, \phi)$  with respect to the crystal axes, we calculate the corresponding energy of excitation,  $\omega$ , through the dispersion relation  $E(\vec{k})$ . For those momentum transfers larger than the first BZ, unique Bloch translations through integer multiples of the inverse lattice momentum can map them back to the first BZ. Then the scattering law is incremented by a value of  $\mathcal{S}(\kappa_i, \omega_j)$  on bin  $(i, j)$ , in which  $i\Delta\kappa = \kappa_i$  and  $j\Delta\omega \leq \omega \leq (j+1)\Delta\omega$ . We generate a large number of randomly generated  $(\theta, \phi)$  values



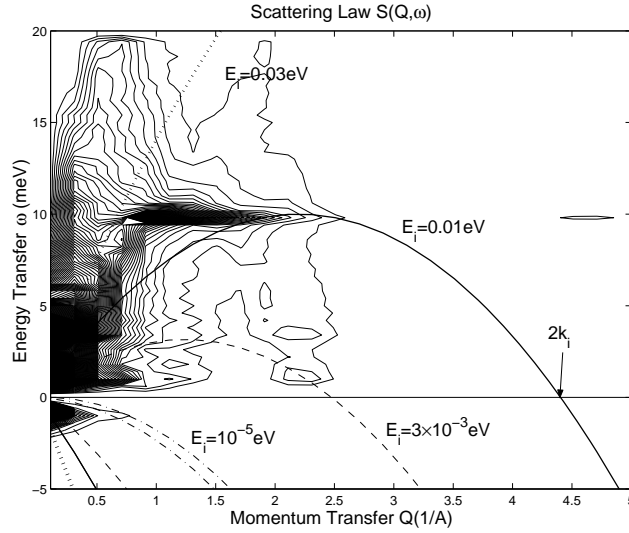
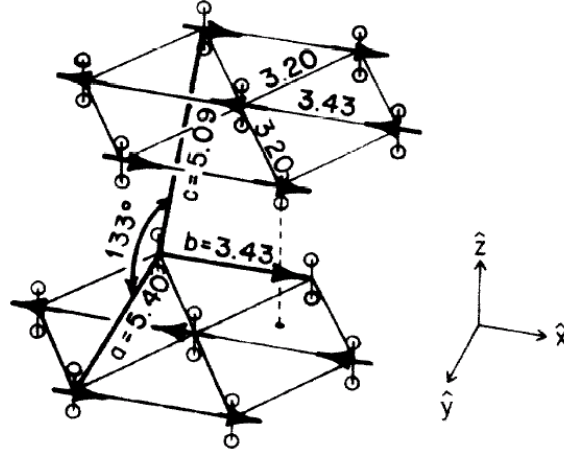


Figure 5.1: Neutron scattering law in a 5K solid  $\alpha$ -O<sub>2</sub>: A contour plot of  $S(\kappa, \omega)$  is presented here. The upper half plane ( $\omega > 0$ ) describes the case of downscattering, and the  $\omega < 0$  describes the case of upscattering. The importance of the contribution from different  $(\kappa, \omega)$  is illustrated by the density of the contours. The area of integration is bounded by the dotted lines for incident neutrons with an initial energy  $E_i = 0.03\text{eV}$ , and solid lines, dashed lines and dash-dotted lines, for  $E_i = 0.01\text{eV}$ ,  $3 \times 10^{-3}\text{eV}$  and  $10^{-5}\text{eV}$ , respectively.

for each  $\kappa$ , and then we average the corresponding  $S(\kappa, \omega)$  values. These resulting  $S(\kappa, \omega)$  values are then inserted back into the double integral Eq.5.7.

Note that in a general solid, for every  $\kappa$ , there exists a continuum of energy modes available for excitation. This is because of the anisotropy of the lattice structure which manifests itself in its orientationally dependent dispersion relation. As a result, a broader energy range of cold neutrons is available for UCN production. This is distinct from the case of neutron inelastic scattering in superfluid  $^4\text{He}$ , where only a narrow band of energy and momentum transfers are allowed because of its simple isotropic energy dispersion curve (a characteristics of most liquids).

Figure 5.2: A schematic of the lattice structure of solid  $\alpha$ -O<sub>2</sub>. [70]

### 5.2.3 Anti-ferromagnetic Magnons

A primitive unit cell with the geometry of a distorted hexagon is a reasonable description of solid  $\alpha$ -O<sub>2</sub>. There are 14 oxygen molecules in this cell, and its long c-axis is tilted from normal of the basal a-b plane by  $133^\circ$  [70]. On the a-b plane, the b-axis is placed on a side of the hexagon which points along the direction of magnetization. The a-axis is then conventionally chosen as orthogonal to the b-axis. While the lattice constant on the c-axis,  $5.09 \text{ \AA}$ , is larger than the spacing between lattice sites on the a-b plane, couplings between the a-b plane layers are relatively weak compared to the in-plane couplings. The suppressed overlaps of molecular wave-functions in the c direction results in a manifest 2-d antiferromagnetism on the a-b plane [70].

The magnetic structure can be described as a composition of two sub-lattices interlacing each other, each carrying the opposite magnetization. Every site is surrounded by 2 nearest neighbors on the same magnetic sub-lattice, and 4 next nearest neighbors on the opposite magnetic sub-lattice.

This system can be described by the following Heisenberg Hamiltonian

$$H = -2 \sum_{\langle ij \rangle} J_{ij} s_i \cdot s_j + \sum_i (-D s_{xi}^2 - D' s_{yi}^2 + D' s_{zi}^2), \quad (5.8)$$

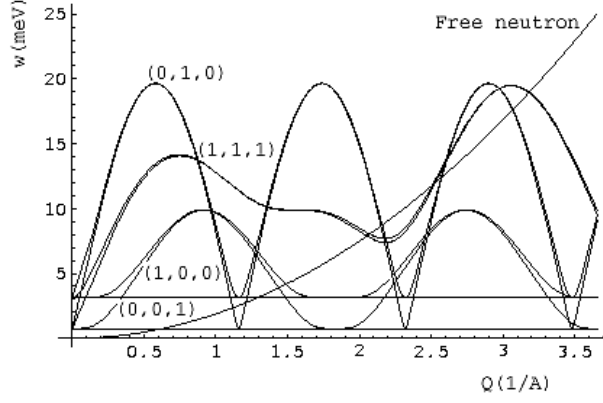


Figure 5.3: The dispersion relation of magnons in solid  $\alpha\text{-O}_2$  ((5.9)): Note the presence of one acoustic and one optical mode. The dispersion relations are plotted for momentum transfer along three principle axes,  $(1,0,0)$ ,  $(0,1,0)$  and  $(0,0,1)$ . Different periodicities originate from different lattice constants on those axes. Momentum transfers along a non-symmetrical direction introduce a non-periodic dispersion relation, which is illustrated by  $(1,1,1)$ . Intersections with the parabolic free neutron dispersion set the condition for UCN production.

where  $J_{ij}$  contains the information of the exchange interactions between site  $i$  and  $j$  with molecular spin  $s_i$  and  $s_j$ , respectively.  $D$  represents the self-energy of the molecular spins along the direction of magnetization, and  $D'$  represents the transverse directions. Here the  $x$  and  $y$ -axes corresponds with the  $b$  and  $a$ -axes, respectively. Note that even though the out-of-plane coupling is negligible, it still has considerable contributions to the scattering in the  $z$ -direction due to the non-trivial self-energy term,  $D'_z s_z^2$ . The energy spectrum of the magnon excitations can be solved from Eq.(5.8) and reduced to the following dispersion relation[70],

$$E_a(\vec{q}) = \sqrt{(2J_0 - 2J_{\vec{q}} - 2J'_0 + D)^2 - [2J'_{\vec{q}} + (-1)^a D']^2}. \quad (5.9)$$

This is an orientationally dependent function because of  $J_{\vec{q}} = \sum_j J_j e^{i\vec{q} \cdot \vec{r}_j}$ , which sums over neighbors on the same sub-lattice, and  $J'$  which is similarly defined on the opposite sub-

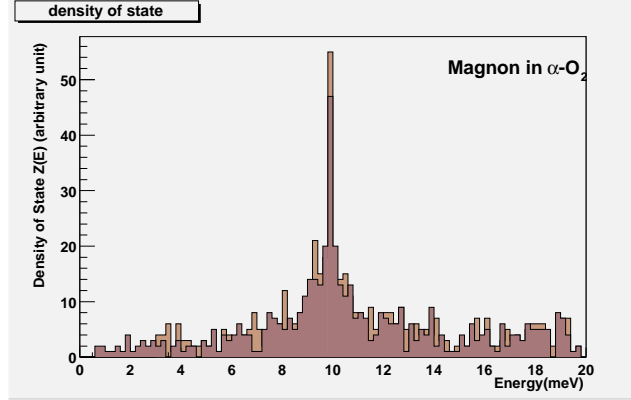


Figure 5.4: The density of states of solid  $\alpha$ -O<sub>2</sub> lattice excitations: The dark and light histogram represents the magnon density of states for acoustic and optical branch, respectively.

lattice. As suggested by Stephens and Majkrzak[70], parameters for spin couplings are chosen here to be  $J_{NN} = -1.22$  meV for the nearest neighbors,  $J_{NNN} = -2.44$  meV for the next nearest neighbors and  $J_{\perp} = 0$  for the out-of-plane (z direction) coupling.  $a = \{0, 1\}$  is the branch index. In Fig. 5.3, this dispersion relation is illustrated at several different orientations of neutron momentum transfer. The dispersion relation for a free neutron,  $E = \hbar^2 \kappa^2 / 2m_n$ , is also plotted. For coherent UCN scatterings (for downscattering as well as upscattering), the intersections of this free neutron dispersion curve and the dispersion curves set the kinematic criteria for neutron-magnon interaction.

When sampled uniformly over the 3-dimensional magnon momentum space  $\vec{q}$ , the dispersion relation is reduced to a histogram representing the density of states  $Z(E)$ , which is defined by

$$\sum_{\vec{q}} = \int dE Z(E). \quad (5.10)$$

This illustrates the relative weight of the contributions of different energy excitations. The resultant density of states for magnons is plotted out in Fig. 5.4. A distinct peak at 10 meV, where live a dense density of states, is caused by the flattening of the dispersion curve approaching the BZ boundary of  $\kappa_x$ . The expected 20 meV peak (which corresponds to the BZ energy in  $\kappa_y$  direction) is less significant because of the smaller flattening region due

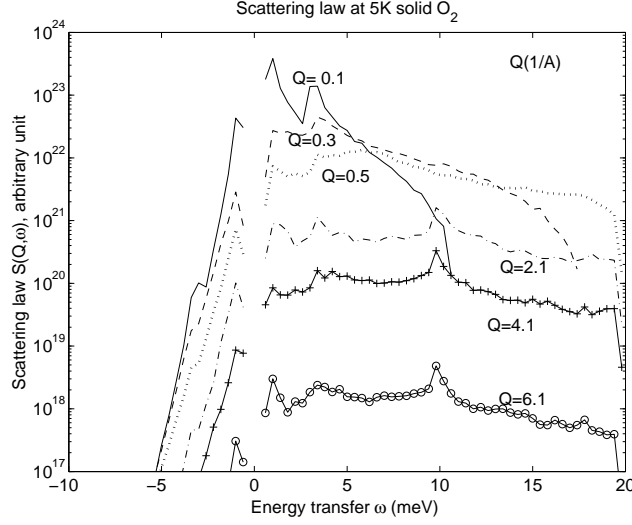


Figure 5.5: Neutron scattering law  $\mathcal{S}(\kappa, \omega)$  of a 5K solid  $\alpha$ -O<sub>2</sub>:  $\mathcal{S}(\kappa, \omega)$  is plotted as a function of the energy transfer  $\omega$  for momentum transfer  $Q=0.1, 0.3, 0.5, 2.1, 4.1$  and  $6.1 \text{ \AA}^{-1}$ . Distinct energy dependences are shown for  $\omega > 0$  downscattering and  $\omega < 0$  upscattering parts. At low  $\kappa$ 's, there exists two dominant contributions at 0.7 meV and 3 meV, which correspond to the self-energy of the acoustic and optical modes, respectively. As  $\kappa$  increases, the significance shifts to a high energy peak centered at 10meV, which is clearly the BZ boundary energy.

to a higher periodicity in  $\kappa_y$ . Note that using the Hamiltonian parameters derived from inelastic neutron scattering, there are no magnon modes with energies below  $E_0 = 0.7 \text{ meV}$ . This is particularly significant for S-O<sub>2</sub> serving as a superthermal UCN source and we will discuss this in greater detail in Sec.5.3.

The scattering law for neutrons scattering from a Heisenberg anti-ferromagnet with single magnon creation(+) and annihilation(-) is well-established [33]:

$$\begin{aligned}
 \mathbb{S}^{\pm}(\vec{\kappa}, \omega) = & \left\{ \frac{1}{2} g F(\kappa) \right\}^2 \frac{1}{4} (1 + \tilde{k}_x^2) e^{-2W(\vec{\kappa})} \frac{(2\pi)^3}{N v_0} \\
 & \times \sum_{a=0,1} \sum_{q, \tau} \left( n + \frac{1}{2} \pm \frac{1}{2} \right) \delta(\hbar \omega_{q,a} \mp \hbar \omega) \delta^3(\vec{q} \mp \vec{\kappa} - \vec{\tau}) \\
 & \times \{ u_q^2 + v_q^2 + 2u_q \cdot v_q \cos(\vec{\rho} \cdot \vec{\tau}) \},
 \end{aligned} \tag{5.11}$$

where  $F(\kappa)$  is the electron spin form factor of the oxygen molecule,  $g = 2$  is the gyro-magnetic ratio of the electron,  $\tilde{k}_x$  is the neutron momentum unit vector component on the axis of magnetization,  $N$  is the total number of scatterers and  $v_0$  is the average volume occupied per scatterer. For this preliminary calculation, a spherical Bessel function[74] of order zero  $j_0(\kappa R/2)$  is utilized for the electron spin form factor  $F(\kappa)$ , which is adequate for a zeroth order estimation.[72]<sup>1</sup> The last part of Eq.(5.11) can be reduced:

$$\begin{aligned} & \{u_q + (-1)^m v_q\}^2 \\ &= 2sN \frac{2J_0 - 2J'_0 - 2J_q + D - (-1)^m [2J'_q + (-1)^a D']}{E_a(q)}, \end{aligned}$$

with  $m = 0$  for a nuclear peak, and  $m = 1$  for a magnetic peak.

This scattering law Eq.(5.11) can be further simplified by summing over the inverse lattice momentum  $\tau$ :

$$\begin{aligned} & \frac{(2\pi)^3}{Nv_0} \sum_{q,\tau} \delta^3(\kappa + q - \tau) \\ &= \frac{(2\pi)^3}{Nv_0} \sum_{\tau} \frac{V}{(2\pi)^3} \int d^3q \delta^3(\kappa + q - \tau) = \sum_{\tau} \delta_{\tau,\kappa+q}. \end{aligned}$$

Unique integer multiples of the inverse lattice momentum  $\vec{\tau}$  can be found to translate each neutron momentum transfer  $\vec{\kappa}$  into the first BZ. The resulting net vector is the momentum  $\vec{q}$  of the created magnon.

With this information, we calculated the orientationally averaged scattering law  $\mathcal{S}(\kappa, \omega)$  for neutron-magnon scattering and tabulated the results on a grid of  $500 \times 500$  points, spaced by  $\Delta\kappa = 0.02\text{\AA}$  and  $\Delta\omega = 0.04$  meV. The contour plot of the scattering law of a 5K solid is shown in Fig. 5.1, and the detailed dependence on energy and momentum transfers are illustrated in Fig. 5.5. In both figures, the peaks correspond to magnons near the BZ boundary, where magnon states are densely distributed. A double integration of  $\mathcal{S}(\kappa, \omega)$  in Eq.(5.5), following the coherent treatment described in the previous section, was performed for solids at various temperatures below  $E_0$ . The resultant neutron-magnon scattering total cross section are plotted in Fig. 5.6.

---

<sup>1</sup> Although difficult to quantify, we believe that our calculations are accurate within a factor of 2.

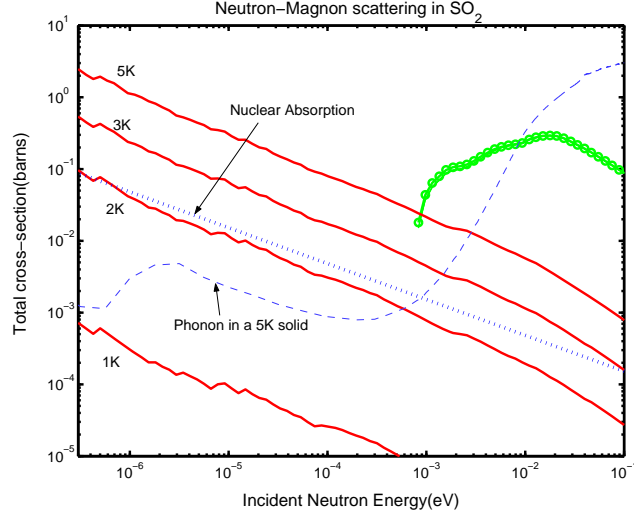


Figure 5.6: The total cross-section(Eq.(5.5)) for a neutron scattering from a solid  $\alpha$ -O<sub>2</sub> at temperatures of 1K, 2K, 3K and 5K with an exchange of a single magnon, compared with neutron-phonon scattering(dashed curve) and nuclear absorption cross-section per <sup>16</sup>O<sub>2</sub> molecule(dotted curve). The circled curve at the high incident neutron energy shows the neutron downscattering cross-section via the creation of single magnon, which is nearly temperature independent. The solid curves represent UCN-magnon upscattering cross-sections at various solid temperatures.

### 5.2.4 Phonon Scattering

The process of neutron-phonon inelastic scattering is also possible inside solid  $\alpha$ -O<sub>2</sub>. The size of a practical UCN source is such that we do not expect more than one phonon or magnon to be created during the residency time of a neutron inside the converter, so we do not concern ourselves with multiple phonons, multiple magnons, or both phonon-magnon events. The scattering law for single phonon creation(+) and annihilation(-) is[33]:

$$\begin{aligned} \mathbb{S}^{\pm}(\vec{\kappa}, \omega) = & \frac{1}{2M_{lattice}} e^{-2W(\vec{\kappa})} \frac{(2\pi)^3}{v_0} \sum_{j=1,2,3} \\ & \sum_{q,\tau} \frac{|\vec{\kappa} \cdot \sigma^j(q)|^2}{\omega_j(q)} \left(n + \frac{1}{2} \pm \frac{1}{2}\right) \delta(\hbar\omega_{q,a} \mp \hbar\omega) \delta^3(\vec{q} \mp \vec{\kappa} - \vec{\tau}). \end{aligned} \quad (5.12)$$

This expression is similar to Eq.(5.11) with the important distinction that there is an additional dependence on the mass of the scatterer  $M_{lattice}$ , located at each lattice site. This mass dependence reflects the inertia in producing a nuclear recoil. When a neutron scatters from a lattice site it causes a recoil: This perturbation can be described as a superposition of the collective vibrational normal modes of the solid (phonon), which then propagate away. This picture does not apply to neutron-magnon scattering, because the spin-wave produced does not result from a nuclear recoil, but from a coupling of the magnetic moment of the neutron to the magnetic moment of the  $O_2$  molecule.

The neutron scattering cross-section via the phonon couplings was calculated using LEAPR, one of the subroutines in the NJOY package developed by Los Alamos National Laboratory [102]. The incoherent approximation is used in this code, and an iterative expansion to include the creation or annihilation of 100 phonons is included. The results are compared with magnon scattering in Fig.5.6.

The intrinsic nuclear coherent scattering length of the oxygen nucleus  $^{16}O$ ,  $b_c = 5.78$  fm is very close to the magnetic scattering length  $r_0 = 5.4$  fm, and thus, as we expect, the mass factor in the phonon scattering cross-section suppresses the scattering cross-section relative to magnon scattering by a factor of 32. However, a large fraction of the magnon scatterings involves higher momentum transfer and is then suppressed by the Debye-Waller factor,  $e^{-2W}$  (in the cross section Eq.(5.12)). As a result, the neutron-phonon scattering is only roughly 5 times weaker than the neutron-magnon scattering.

### 5.3 Solid $O_2$ vs. Solid $D_2$ for UCN Production

In S- $O_2$ , with its thermal energy  $k_B T$  below the minimum threshold of excitation  $E_0 \approx 8K$ , the total number of the magnons present is exponentially suppressed as one cools down the



solid:

$$\begin{aligned}
N &= \sum_i n_i \\
&\cong \frac{V}{(2\pi)^3} \int_{E_0}^{\infty} Z(E) dE \frac{1}{e^{E/k_B T} - 1} \\
&\propto e^{-8/T},
\end{aligned} \tag{5.13}$$

We approximate  $Z(E)$  to be roughly constant above  $E_0$ . At low temperatures, there is essentially no low energy magnon mode to be thermally populated, and only a small population of the magnon modes with energy higher than  $E_0$  exist. The resultant exponential factor,  $e^{-8/T}$ , thus exhibits a stronger quenching effect on the UCN upscattering from magnon absorption than in the case of phonon absorption in solid deuterium. Moreover, the phonon interaction is much weaker than the magnon interaction at this temperature, so phonon upscatterings need not to be considered. The loss rate due to the upscattering from magnons equals the nuclear absorption rate at 2.1 K. Further cooling will increase the lifetime by no more than a factor of two.

Note also that natural oxygen is over 99%  $^{16}\text{O}$ , which has neither electronic nor nuclear spin. The molecular rotational spectrum has only one set of allowed rotational states;  $^{16}\text{O}$  can not be excited into long lived rotational states at low temperature. Recall, however, that the interaction of UCN with the rotational states of  $\text{D}_2$  is a major source of loss in S- $\text{D}_2$  sources, and must be controlled[35] by minimizing the para- $\text{D}_2$  concentration (see chapter 3).

The maximum achievable UCN density is:

$$\rho_{ucn} = (P \times \tau) \propto \frac{\bar{\sigma}_{ucn} \Phi}{n \sigma_{abs} v_{ucn}}. \tag{5.14}$$

To obtain a practical value for the UCN production, one needs to incorporate a realistic cold neutron energy distribution into the cross section integration. With a normalized cold neutron flux of  $\Phi(E)$  with a Maxwell-Boltzmann distribution, the production rate is:

$$P_{ucn} = n \int \left( \frac{d\sigma(E \rightarrow E_{ucn})}{dE} E_{ucn} \right) \Phi(E) dE. \tag{5.15}$$

The production rate is plotted in Fig. 5.7 as a function of the cold neutron temperature. It is evident that the optimum temperature is  $\sim 6$  K, somewhat lower than the 30K optimal temperature for a S-D<sub>2</sub> source[26]. As reported by Hill *et al.*[76], a Maxwellian cold neutron spectrum with a temperature around 30 K is characteristic of our spallation neutron source. The UCN conversion rate is

$$\begin{aligned}
 P_{ucn} &= \{2.2 \times 10^{-8}\} \times \Phi_0 && \text{with 30K cold neutrons} \\
 &= \{3.5 \times 10^{-8}\} \times \Phi_0 && \text{with 12K cold neutrons} \\
 &= \{1.95 \times 10^{-8}\} \times \Phi_0 && \text{with 30K cold neutrons in ortho S-D}_2 \\
 &= \{1.74 \times 10^{-8}\} \times \Phi_0 && \text{with 30K cold neutrons in para S-D}_2,
 \end{aligned}$$

where  $\Phi_0$  is the total neutron flux. A 60% more UCN production may be possible if a 12K cold neutron flux could be achieved. Moreover, the five times smaller nuclear absorption cross-section of <sup>16</sup>O than D[27] gives an UCN absorption time of 750ms in solid O<sub>2</sub>. The best lifetimes achieved to date in S-D<sub>2</sub> are approximately 40ms, so an improvement of roughly a factor of 10 is available in S-O<sub>2</sub>. Furthermore, because the UCN elastic mean free path in S-O<sub>2</sub> single crystal is infinite, (incoherent scattering length = 0, and no coherent elastic scatterings for UCN) the dimension of the source is limited by the nuclear absorption length, which is five times longer than that of solid deuterium. Larger volume sources may be constructed and a much larger UCN output flux may be possible. However, the tendency of micro-crystals to form in S-O<sub>2</sub>[79, 80] may limit the effectiveness of larger UCN source.

The advantages of a solid oxygen source may be tempered by the fact that it is difficult to produce a large single crystal of  $\alpha$ -oxygen. In addition, the heat conductivity is lower[69]. Also, it is clear that in order to realize all of the potential gains of this converting material, one should utilize crystals near 2 K, and cold neutron fluxes near 6 K, which are lower temperatures than those required for optimal use of S-D<sub>2</sub>. In the high radiation fields typical for neutron sources, ozone formation[78] in the crystal may be a safety concern as well as a source of loss for UCN, although we have no quantitative information on the UCN loss rates at present. One also expect more  $\gamma$  ray heating of oxygen because of its higher Z

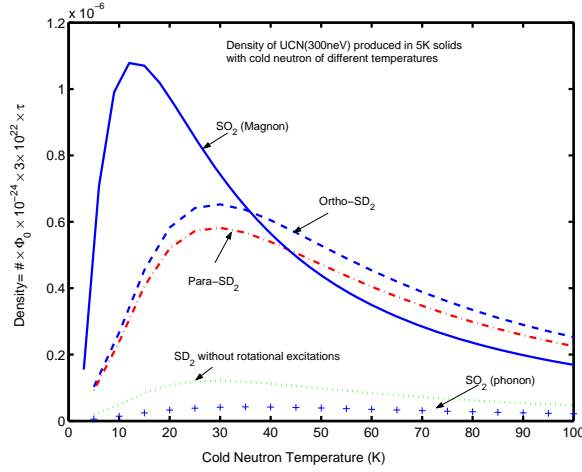


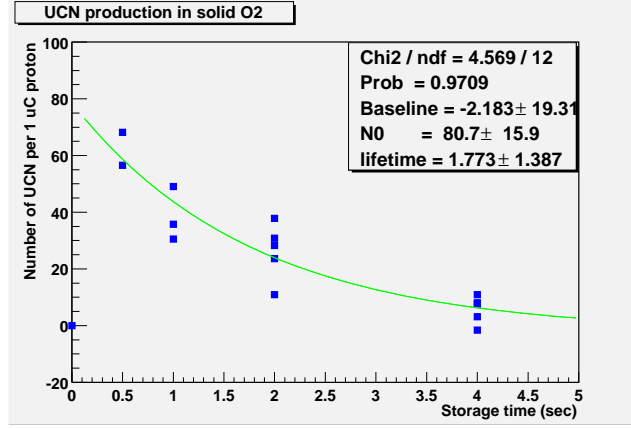
Figure 5.7: UCN density vs. temperature of incident cold neutron flux with Maxwell-Boltzmann spectrum. The UCN production in S-O<sub>2</sub> peaks with cold neutrons at 12K, whereas in S-D<sub>2</sub> the UCN production is optimized using cold neutron flux with a higher temperature of 30K.

than solid deuterium. Finally, we investigated the effects of hyperfine transitions[73] in the S-O<sub>2</sub> crystal as a source of UCN loss, and find no significant rate for UCN upscattering. However, definitive measurements of the UCN lifetime in solid oxygen are required to place quantitative limits on this loss mechanism as well.

We have reviewed the characteristics of solid oxygen as a UCN source, by analyzing inelastic neutron-magnon scattering. Oxygen appears to be a promising candidate, with strengths and weaknesses which compliment those of solid deuterium.

## 5.4 Experiment on UCN Production in S-O<sub>2</sub>

We performed a measurement of UCN production in solid oxygen using cryostat we designed for the study of the S-D<sub>2</sub> superthermal process, as as described in chapter 4. The lowest solid O<sub>2</sub> temperature we could achieve with this cryostat was 5 K. Nevertheless, UCN were successfully produced by a 20 cm<sup>3</sup> volume of solid oxygen which was condensed from industrial grade O<sub>2</sub> gas. The data demonstrates that S-O<sub>2</sub> produced a less total number of

Figure 5.8: UCN lifetime run with S-O<sub>2</sub>.

UCN  $0.097 \pm 0.03$  times of that of solid ortho-D<sub>2</sub>, which has a 2.5% para-D<sub>2</sub> contamination under the same physical condition.

To compare with the presented calculations, we analyzed the measured UCN number by formulating the UCN production

$$N_{ucn} = nVP \times t = nV(\Phi_0 \sigma_{production})t. \quad (5.16)$$

Assuming a large UCN mean free path, the number of UCN produced by such a small source should only be sensitive to the production power, and not to the UCN loss inside the source material.<sup>2</sup> The production time,  $t$ , in Eq.(5.16) is thus the duration of the cold neutron pulse. This can be combined with the cold neutron flux,  $\Phi_0$ , to give the total number of incident cold neutrons,  $N_0$ . Our calculations show that for a 30 K Maxwellian cold neutron flux the temperature independent UCN production rate of oxygen is half the production rate of deuterium. As a result, the ratio of total number of UCN produced per pulse in

<sup>2</sup>In the case of 20 c.c. S-O<sub>2</sub>, the vertical dimension (0.4 cm), assuming a pancake shape, is much smaller than the magnon upscattering length at 5K,

$$l = \frac{1}{n\sigma} = \frac{1}{(2.89 \times 10^{22}/\text{cm}^3) \times (2 \times 10^{-24}\text{cm}^2)} = 17.3 \text{ cm}. \quad (5.17)$$

S-O<sub>2</sub> to S-D<sub>2</sub> is

$$\frac{N_{ucn}^{O_2}}{N_{ucn}^{D_2}} = \frac{P^{O_2}t}{P^{D_2}t} = \frac{2.2 \times 10^{-8} N_0}{(1.95 \times 0.975 + 1.74 \times 0.025) \times 10^{-8} N_0} = 1.1, \quad (5.18)$$

which is 10 times larger than the measured result. No correction to the UCN transport is introduced because of a similar neutron potential in both materials. However, a followup S-O<sub>2</sub> crystal growing test showed that a thin layer of very diffusive O<sub>2</sub> film coated the UCN transport guide for 15 cm from the surface of the cryostat. Therefore, this could have affected the UCN transport in the S-O<sub>2</sub> test. We could put an upper bound of the number ratio in the case when the characteristic time,  $t$ , is limited by UCN loss in the S-O<sub>2</sub> film during transport:

$$\frac{N_{ucn}^{O_2}}{N_{ucn}^{D_2}} \leq \left( \frac{P^{O_2}}{P^{D_2}} \right) \left( \frac{\sigma_{loss}^{D_2}}{\sigma_{loss}^{O_2}} \right) = 1.1 \times \frac{0.4 \text{ barns}}{2 \text{ barns}} = 0.2. \quad (5.19)$$

We assume that the UCN also suffer the same kind of transport loss in solid deuterium thin film. The loss in S-D<sub>2</sub> comes equally from deuteron nuclear absorption (0.1 barn), phonon upscattering (0.1 barn), para-D<sub>2</sub> upscattering (0.1 barn) and isotope H absorption (0.1 barn), whereas the loss in S-O<sub>2</sub> is dominated by the magnon upscattering (2 barn) as shown in Fig. 5.6. The corrected UCN yield agrees with our experimental result within a factor of two. The above estimate combined with the observational evidence of the presence of a diffusive S-O<sub>2</sub> thin film lead us to believe that the UCN upscattering loss in transport through the thin film coated guide accounts for the discrepancy between our calculation and measurements. Other possible sources of additional loss in 5K solid oxygen may come from the UCN transport inside the polycrystal solid which is not yet well understood.

Even though we have not yet demonstrated the predicted strong superthermal UCN production via the magnon mechanism in solid oxygen, the preliminary results in this test are encouraging and they strongly suggest more UCN should be produced once several of the identified problems have been fixed. This motivates further investigations on UCN production in S-O<sub>2</sub> with an improved 2 K cryostat which should fully optimize the magnon superthermal mechanism.

## Chapter 6

# An UCN Spin Flipper

We report the first application of the bird cage resonator as an adiabatic fast passage (AFP) UCN spin flipper[84]. The principles of operation of both the AFP spin flipper and the bird cage resonator are briefly reviewed, and the fabrication techniques of such a device are presented. An experimental test of an AFP spin flipper just carried out at ILL achieved an UCN spin-flip efficiency of higher than 99.6%, This technique will be useful for measurements of neutron  $\beta$ -decay using polarized UCN.

### 6.1 Introduction – AFP Spin Flip

Neutron spin will precess along a magnetic field and, as a result, a well defined magnetic field is often used to guide and preserve the spin orientation of polarized neutrons. A naive conception of spin flipping thus consists of a static field which spatially reverses its direction. The spin of neutrons passing through such a field adiabatically follows the field direction and reserves their orientation. This desired field profile can be constructed by combining a static, monotonically decreasing longitudinal field which changes its direction at the flipper midpoint with a static transverse field with a maximum strength at the midpoint. This spin flip technique was successfully demonstrated with slow neutrons [81], however, the efficiency ( $\sim 80\%$ ) is not adequate for the proposed high precision measurement of the “A” coefficient in neutron  $\beta$ -decay where we need a 99.9% efficiency. Thus, we examine another technique

first proposed by Bloch [82] and implemented by Egorov *et al.*[83]

Bloch's idea is based on nuclear magnetic resonance (NMR) where a small dynamic field is applied to provide the energy quanta required to drive transitions between the two spin states. Under the application of a rotating transverse field with angular frequency  $\omega$ , the classical description of the spin evolution,

$$\frac{d\mathbf{M}}{dt} = \frac{\partial\mathbf{M}}{\partial t} + \boldsymbol{\omega} \times \mathbf{M} = \gamma\mathbf{M} \times \mathbf{H}, \quad (6.1)$$

can be simplified in a frame co-rotating with the transverse field component. In such a rotating frame<sup>1</sup>, the equation of spin precession is[84]:

$$\frac{\partial\mathbf{M}}{\partial t} = \gamma\mathbf{M} \times (\mathbf{H} + \boldsymbol{\omega}/\gamma) = \gamma\mathbf{M} \times \mathbf{H}^{eff}. \quad (6.2)$$

The fictitious force field,  $\boldsymbol{\omega}/\gamma$ , which originates from the rotation of the coordinate frame, can be introduced in such a way as to cancel the longitudinal field,  $H^0$ . To be more explicit,

$$\mathbf{H}^{eff} = (H^0 - \omega/\gamma)_{\parallel} + H'_{\perp}. \quad (6.3)$$

Here  $H'_{\perp}$  stands for the strength of the superimposed transverse field. With a monotonically decreasing longitudinal holding field  $H^0$ , we create the same static field condition mentioned above for a spin flip when the spin precession is analyzed in a co-rotating frame (Eq.(6.3)). The advantage over the static configuration is that a large nonzero holding field  $H^0$  is utilized, eliminating the zero field region where neutrons are allowed to freely precess, and thus depolarize. The frequency  $\omega$  of the rotating transverse field  $H'_{\perp}$  is tuned to the resonance frequency of neutrons in the magnetic field, which is dominated by the longitudinal holding field  $H^0$ , i.e.,

$$\omega = \gamma H^0 = \frac{ge}{2mc} H^0. \quad (6.4)$$

With this approach, the challenge is to carefully tailor the homogeneity of the main monotonically decreasing longitudinal field, so as to ensure a single, well defined resonance point inside the rotating transverse field region.

---

<sup>1</sup>If  $z$  is the direction of the holding field, the coordinate transformation is on the x-y plane:  $x' = x\cos(\omega t) + y\sin(\omega t)$  and  $y' = -x\sin(\omega t) + y\cos(\omega t)$ .

In this chapter, we present a comprehensive discussion of the development and test of a radio frequency (RF) resonator which produces the required oscillating<sup>2</sup> transverse field, one of the key elements of the NMR neutron spin flip technique described above.

## 6.2 The Bird cage Resonator

We applied the bird cage resonator, developed for medical imaging research, to the neutron spin flip, for fundamental physics studies of polarized neutron decay. To build such a resonator, one places conducting rungs equally displaced in the azimuthal angle on a circle, and uses two end rings to make the electrical connections. It is utilized for its superb RF field homogeneity inside the resonator and its easy RF resonance frequency tunability. Also, from a practical point of view, the cylindrical symmetry of the device ensures that it is compatible with our neutron guide geometry. Previous devices used perpendicular RF coils or solenoids[87].

Given a surface current flowing on a conducting cylinder parallel to the symmetry axis, with a sinusoidal distribution in the azimuthal angle  $\theta$ , it can be shown that the field generated inside the cylinder is uniform everywhere, and points transversely along the direction  $\theta = 0$ , where no current flows. For the bird cage resonator, the design goal is to generate such a sinusoidal current distribution in a finite element conducting cylinder using the lumped element delay lines.

### 6.2.1 Theory of the Resonator

The lumped LC circuit shown in Fig. 6.1 is a schematic of a bird cage resonator and is analyzed by the voltage equations:

$$\Delta V_n = V_{n+1} - V_n = j\omega L I_n \quad (6.5)$$

$$V_n = \left( j\omega M + \frac{1}{j\omega C} \right) (I_{n-1} - I_n) \quad (6.6)$$

---

<sup>2</sup>The choice of an oscillating field instead of a rotating field is discussed in the Section 6.2.4.



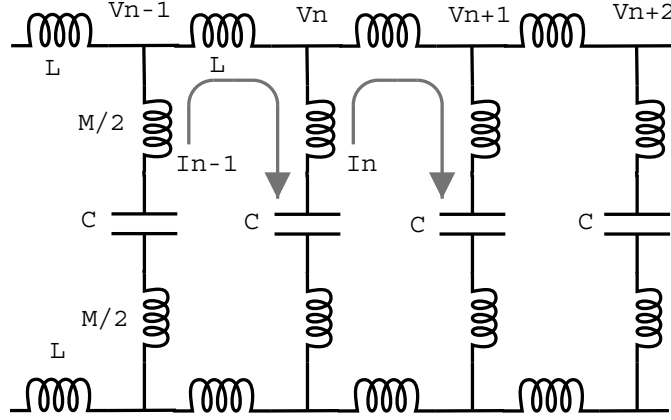


Figure 6.1: An electrical diagram of the lumped LC circuit in a bird cage resonator.

where the capacitor,  $C$ , and the inductance  $L$  and  $M$ , are identical for each repeating LC element indexed by  $n$ . Both  $L$  and  $M$  here represent effective inductances, including the self inductance and the mutual inductance which can be calculated once the geometrical parameters are given[88]. For a closed network in which the end is connected to the beginning, the *ansatz*,

$$I_n^J = I_0^J e^{i(nJ\frac{2\pi}{N})}, \quad (6.7)$$

solves the voltage equations, and one finds that this periodic structure sustains standing waves with a frequency spectrum of

$$\omega_J = 2\omega_a \frac{\sin(\pi J/N)}{\sqrt{1 - 2(\omega_a/\omega_b)^2 \cos(2\pi J/N)}}, \quad J = -N/2, \dots, 0, 1, 2, \dots, N/2 - 1. \quad (6.8)$$

Here  $\omega_a = 1/\sqrt{(L + 2M)C}$ , and  $\omega_b = 1/\sqrt{MC}$ .  $N$  is the total number of the repeating LC elements. There should be  $N$  modes of  $J$ , however,  $J = 0$  and  $J = -N/2$  are trivial solutions, and the trigonometric function dependence in the frequency spectrum Eq.(6.8) makes the positive and negative  $J$  modes degenerate in energy (but orthogonal in polarization), leaving only  $(N/2-1)$  non-degenerate modes, i.e.,  $J = 1, 2, \dots, N/2 - 1$ .

The fundamental mode ( $J = 1$ ) is the standing wave solution: one wavelength spans the whole network. Only this mode is useful for NMR. As illustrated in Fig. 6.2, when such a resonator is driven in the fundamental mode, the rungs automatically carry the inherited

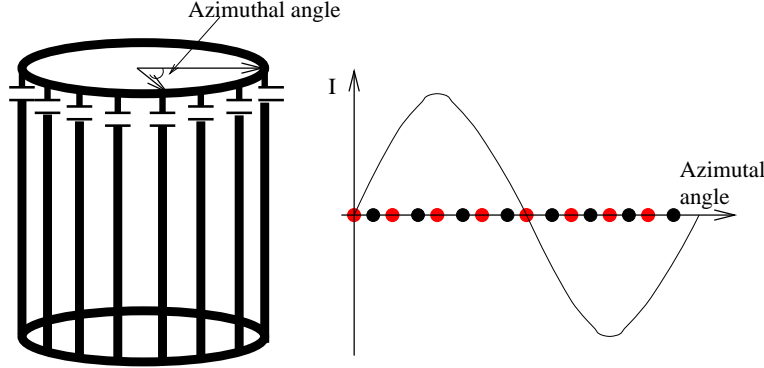


Figure 6.2: A schematic of a 16-rung bird cage resonator and a current distribution when driven in the fundamental resonant mode.

sinusoidal current distribution, which is the desired configuration to produce a homogeneous transverse field.<sup>3</sup> High frequency external power is supplied to resonantly drive the resonator in the fundamental mode and sustain the oscillating homogeneous transverse field inside the resonator.

### 6.2.2 Fabrication of the Resonator

We first tried to use copper tube as the bird cage rungs, however, it was later proven that copper tape[85] with conducting adhesive is an easier and smarter approach which provides greater flexibility for modifications. Plexiglas tube was used as structure support; the copper tapes were applied to the outer surface of the Plexiglas to construct the rungs and end rings. Capacitors were soldered between rungs and one of the end rings. We built a 4" O.D., 10" long, 16 rung bird cage resonator. The the widths of the end rings and rungs were 3/4" and 3/8", respectively. The thickness of the tape is 0.0014". 100 pF

<sup>3</sup>To be explicit, the current flowing in the  $n^{th}$  rung is

$$\begin{aligned}
 \Re(I_n^1 - I_{n+1}^1) &= \Re(I_0 e^{in\frac{2\pi}{N}} - I_0 e^{i(n+1)\frac{2\pi}{N}}) \\
 (\text{for } I_0 = I e^{i\phi}) &= I \cos(\phi + n\frac{2\pi}{N}) - I \cos(\phi + n\frac{2\pi}{N} + \frac{2\pi}{N}) \\
 (\text{set } \phi = -\frac{\pi}{N}) &= 2I \sin \frac{\pi}{N} \sin(n\frac{2\pi}{N}).
 \end{aligned} \tag{6.9}$$

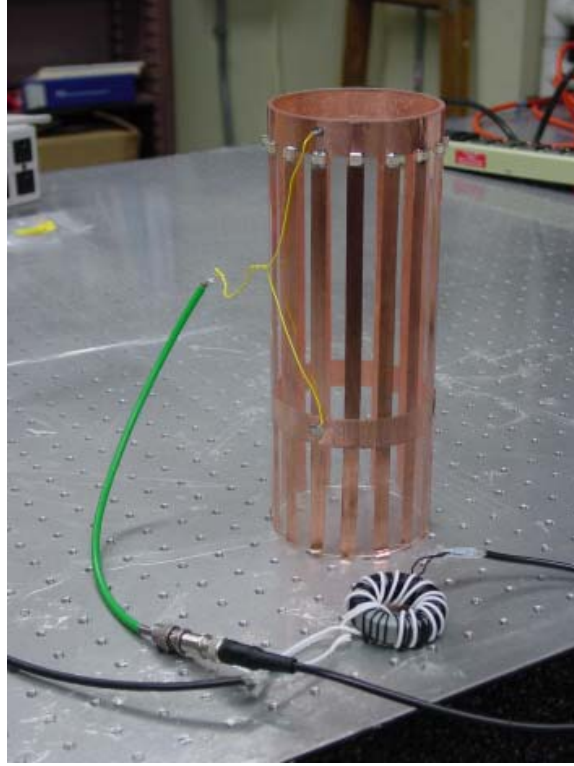


Figure 6.3: A picture of the bird cage resonator.

capacitors were used. The resonant spectrum was measured and fit to Eq.(6.8), as shown in Fig.6.4. The fit to the theoretical formula is not perfect (the  $\chi^2$  value is not consistent with Poisson statistics) because of an inexact account of the mutual inductance coupling between rungs[85]. Nevertheless, the shape of the spectrum demonstrates the predicted performance, and the fitted parameters provided information on the effective inductance of each element, which was helpful in following frequency tuning step. In this case, the values of  $\omega_a$  and  $\omega_b$  indicate that the effective inductance of the rung ( $M$ ) is 71.5 nH, and that of the end ring ( $L$ ) is 74.8 nH. These numbers can be compared with the inductance of conductors with simple geometry calculated and tabulated in Ref. [88]. For example, the self inductance of a round wire with radius,  $\rho$ , is

$$0.002l \left[ \ln \frac{2l}{\rho} - \frac{3}{4} \right] \quad \mu H, \quad (6.10)$$

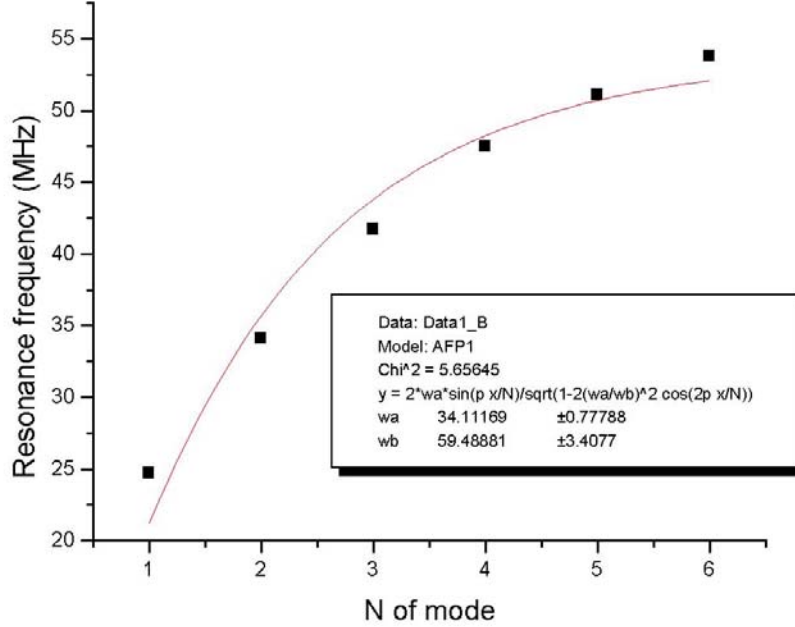


Figure 6.4: The frequency spectrum of the bird cage resonator.

where  $l$  is the length measured in centimeter. For a wire of rectangular cross section, with sides of length  $B$  and  $C$ , the self inductance is

$$0.002l \left[ \ln \frac{2l}{B+C} + \frac{1}{2} - f \right] \quad \mu H, \quad (6.11)$$

where  $f$  can be found in Table 3 in Ref.[88].<sup>4</sup>

In this resonator, the fundamental mode has a frequency of 24.5 MHz, which is lower than 30 MHz, the Larmor frequency of neutrons in a field of 1 T. To properly tune the frequency to the desired value (using the LC dependence in Eq.(6.8) as the guide), one would replace the capacitors for a coarse tuning, and further tailor the dimensions (length and width) of the copper tapes of the rungs, to vary the inductance  $M$ , and end rings, to vary the inductance  $L$ , for the fine tuning.

<sup>4</sup>It has a value  $\sim 0.002$  for a wide range of  $B/C$ .

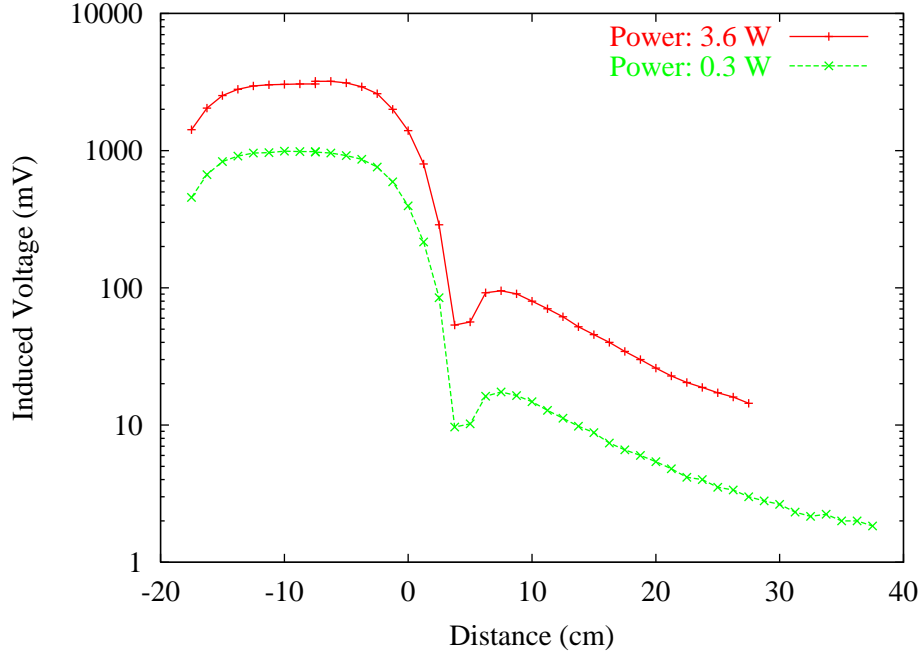


Figure 6.5: The transverse field profile of the bird cage resonator. The resonance frequency is 27.4 MHz. Blue and green curves are data sets with input power of 0.3W and 3.6W, respectively. One edge of the resonator is set at the origin.

### 6.2.3 The Field Profile

The homogeneity of the field inside of the bird cage resonator has been studied and measured to a very high precision using NMR signals of standard test samples[89] (for example, water). The near field profile outside of the resonator, however, is not known well. For our nuclear spin flip application good knowledge of the residual RF field outside of the resonant region is essential to control and reduce the probability of unwanted spin flips.

We measured the field profile of the fundamental resonant mode of this bird cage resonator (used for the resonance frequency measurement), after having modified to a length of 17.5 cm and a resonant frequency of 27.4 MHz. The voltage induced in a  $1 \text{ cm}^2$  single loop coil was used to measure the B field. Two data sets of the on-axis field strength with input power of 0.3W and 3.6W are presented in Fig.6.5. We observed a significant peak

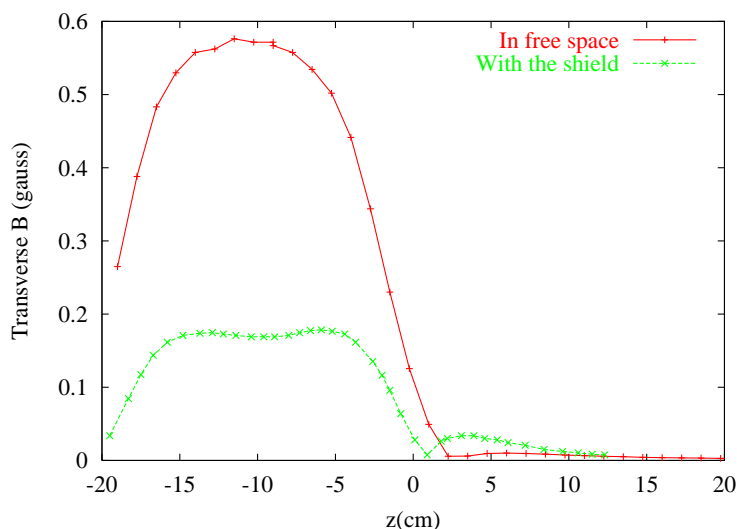


Figure 6.6: A measurement of RF field strength inside the shielding. The metal shield has an O.D. of 14 cm and wall thickness of 0.625 cm. The presence of the shield shifts the resonance frequency from 27.4 MHz to 33.9 MHz. The input power in the resonator is 0.3 W.

after the fast decay in the field strength right outside the resonator. This unexpected peak appears roughly one radius away from the end ring outside of the resonator. A Biot-Savart integration by decomposing the sinusoidal current flow in the bird cage network into a sum of current loops correctly reproduced the measured field profile. This peak originates from the returning currents in the end rings producing an out-of-phase field. An incomplete cancellation between the tail of the central transverse field and this edge field produced the observed residual peak. This calculation and discussions on various parameters impacting the field profile, including shielding (see Fig.6.6), are presented in appendix F.

#### 6.2.4 Discussion

Here we discuss the technical details encountered during the development of such a resonator. First, we learned the hard way that impedance matching is essential in applications with power amplifiers. The RF amplifier we used, American Research Amplifier model

100A150, nominally outputs a power of 150W. Improper impedance matching results in power reflection which can destroy the output power transistors in the final RF amplifying stage. There are different ways to address this problem. We used a resistance transformer to step the impedance of the bird cage resonator to  $50\ \Omega$ , the value of the output impedance of the power amplifier. The resistance transformer has a high  $Q$  ferrite core.<sup>5</sup>

For better circuit performance, one would like to reduce the resistance of every electrical element. The overall resistance (characterized by the  $Q$  factor) determines the efficiency for converting power into the produced field strength, as well as the width of the resonance ( $Q = \omega_0/\Delta\omega$ ). In the case of the bird cage resonator at RF frequency, the power loss is dominated by the capacitors. To reduce this loss, we used porcelain multilayer capacitors manufactured by American Technical Ceramics. Their 100 pF capacitor has a high  $Q$  of approximately 2000 at 30 MHz, and a maximum working voltage of 2500 V. The surface mount design eliminates connecting leads, further reducing the additional uncontrolled inductance and loss.

The power coupling present additional concerns. A direct coupling which separately attaches the two power leads onto the opposite end rings, fixes the boundary condition of the resonator. The resultant oscillating field is thus linearly polarized ( $= \sigma^+ + \sigma^-$ ). The other way to deliver power into the resonator is through inductive coupling[85]: The bird cage resonator can be effectively driven by a single current loop (power loop), driven by the power supply at the resonant frequency, placed close to the surface of the resonator. With this coupling method the resonator is in “free-running” mode, and thus, both degenerate transverse modes are simultaneously excited. The relative position of the power loop to one of LC loops of the resonator controls the phase difference between the two linearly polarized modes. As a result, one of the two circularly polarized fields,  $\sigma^+$  or  $\sigma^-$ , can

---

<sup>5</sup>With the assumption of energy conservation as well as the flux conservation, it can be easily deduced that the ratio of the resistances is proportional to the square of the ratio of number of winding. For example, a 47 nF capacitor operated at 1.5 MHz has a resistance of  $2\ \Omega$ , and thus a 1:5 transformer is needed for the optimal power delivery. One should also note that the impedance of the LC circuits is frequency dependent.

be selected by adjusting the inductance coupling method.<sup>6</sup> With such a capability, one can envision possible applications like optical pumping of UCN into a definite spin state in a storage configuration (as opposed to the flow mode used in the spin flip experiment discussed next). Splitting the end rings open destroys the symmetry and thus, one of the degenerate modes is suppressed and only the linearly oscillating mode can be excited. Note that in an experiment requiring a flow of polarized UCN through an AFP spin flipper, one would demand that the resonator run in the linearly polarized mode, in which both the circular polarizations exist, so that a spin flip can occur for both entrance directions. Only this technique can ensure a minimum contamination of the wrong spin state in the polarized UCN flowing through the AFP due to multiple passes.

### 6.3 UCN Spin Flip Experiment

In October of 2001, we conducted an experiment at the ILL to measure the depolarization of polarized UCN stored in diamond-like carbon coated UCN guides and bottles, and to test the performance of the AFP spin flipper described above. In the following, we will only focus on the part of the experiment which measured the spin flip efficiency.

#### 6.3.1 Experimental Setup

The ILL UCN facility provides a constant UCN flow coming from the turbine source at the top of the reactor. Adopting an existing UCN gravity spectrometer as the UCN reservoir (UCN buffer), we attached onto it the assembly for the UCN depolarization measurement, consisting of diamond-like carbon/quartz guides, magnets, a spin flipper and detectors as shown in Fig 6.7. Diamond-like carbon/quartz guides were used wherever possible (indicated by the red tube) in forming a depolarization-free storage volume for UCN. The 3" I.D. quartz tube was coated on the inner walls with diamond-like carbon thin films using the pulsed laser deposition (PLD) technique implemented at the Virginia Polytechnic Institute and State University[91]. It was reported that carbon thin films (graphite) have a

---

<sup>6</sup>The distance between the power loop to the resonator affects the  $Q$  value, or the resonant peak width.



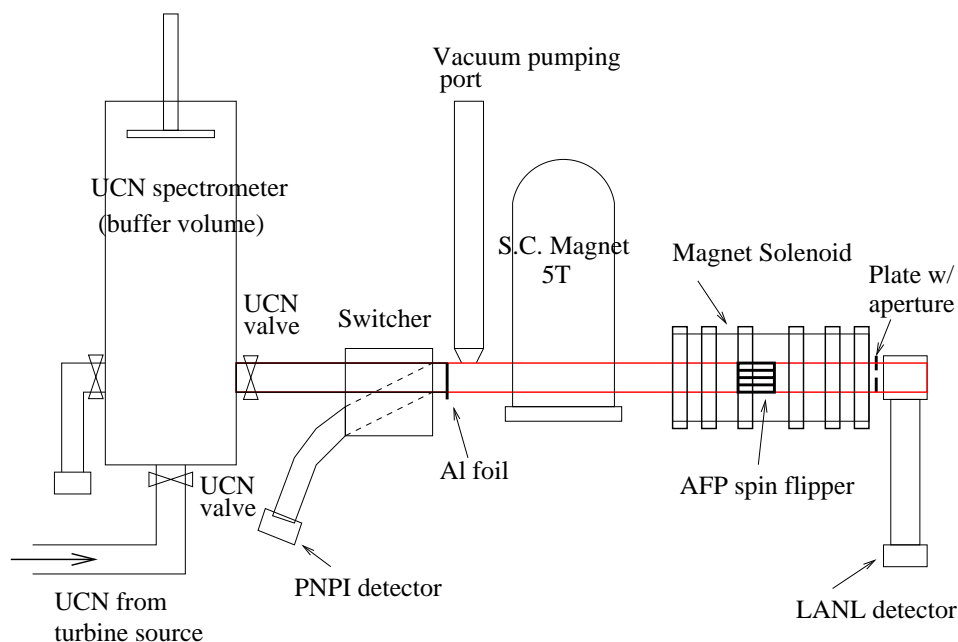


Figure 6.7: A schematic of the experimental setup at ILL.

depolarizing effect on polarized UCN at the level of 1 part in  $10^6$  per bounce[90]. Diamond has a higher number density and exhibits a higher critical velocity ( $\sim 7.2$  m/s) for neutrons. These features make diamond coatings ideal for the polarized UCN guide applications.

After the UCN buffer was a switcher (consisting of a vacuum housing and a polished S.S. tube) which was pneumatically actuated to switch the direction of UCN flow towards the quartz guide or the PNPI detector. To reduce the chance of hydrogen contamination, two dry turbo pumping systems were used in parallel directly pumping the main vacuum as well as differentially pumping all the junctions between quartz guides and metal tubes. The LANL detector was attached to the end of the guide through a small aperture, providing continuous monitoring of the number of neutrons in the diamond-coated guide without significantly perturbing the population.

In the middle of the UCN guide system a 5 T superconducting magnet was placed which was used to filter the spin states of the incoming unpolarized UCN, allowing only UCN polarized antiparallel with the direction of motion. On the downstream side of this

Event	Upstr.	$V_1$	AFP	$V_2$	Comments
Fill (60s)	$+-$	$+$	off	$+$	fill the trap with “+” spin
(40s)	$+-$	$+$	on	$-$	produce a population of “-” spin
Empty		$-$	off	$-$	trapped: $N_0$
(40s)		$+$		$+$	emptied: $N_1$ ( $1^{st}$ $\mathbf{pk}$ in PNPI det.)
AFP on		$-$	$\longleftrightarrow(\mathbf{on})$	$+$	trapped: $N_0 \times \frac{V_1}{V}$
(40, 20, 10s)		$+$	$\longleftarrow(\mathbf{on})$	$-$	emptied: $N_2 = N_0 \times \frac{V_2}{V}$ ( $2^{nd}$ $\mathbf{pk}$ )
AFP off		$-$	off	$-$	trapped: $(N_0 \frac{V_1}{V}) \times \frac{V_1}{V}$
		$+$		$+$	emptied: $N_3 = (N_0 \frac{V_1}{V}) \times \frac{V_2}{V}$ ( $3^{rd}$ $\mathbf{pk}$ )

Table 6.1: The scheme of the AFP spin flipping experiment. The time order of events follows the increment of the rows. The trap region is divided into  $V_1$  and  $V_2$  by the position of the AFP spin flipper.

superconducting magnet, the UCN polarization was held by a magnetic field of 500 gauss, which was generated by conventional solenoidal magnets with a total current of roughly 50 A. The AFP spin flipper (bird cage resonator) was placed coaxially around the quartz cylindrical guide in approximately the middle of the conventional solenoid magnet. We manipulated the spin states of the UCN with the spin flipper, and the resultant population of the spin states were detected with a detector (PNPI detector) which was placed on the upstream side of the superconducting magnet.

### 6.3.2 Experimental Scheme and Procedure

The efficiency of the spin flipper was determined using the following procedure (see Table 6.1, too).

#### Filling Stage

The experiment starts by filling the polarization preserving system (diamond-like carbon/quartz guide) with polarized UCN (with spin “+”). The switcher directs the UCN flow from the buffer volume to the guide tube in the magnetic region. Unpolarized UCN

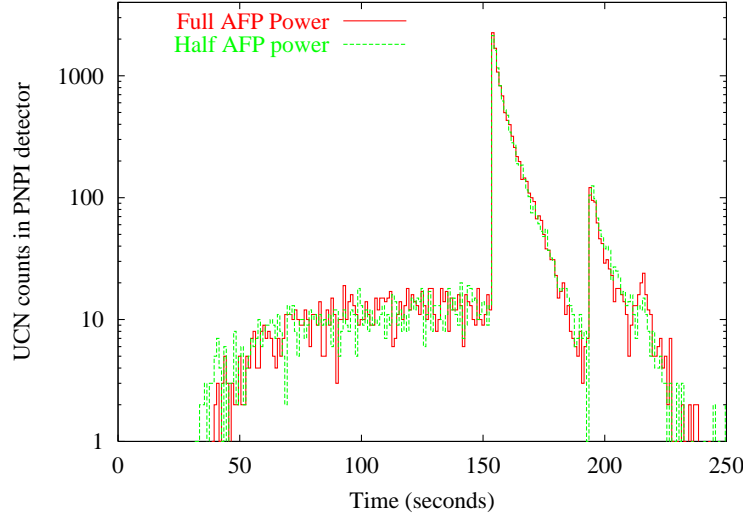


Figure 6.8: UCN counts in the PNPI detector with 40 seconds of AFP spin flipper on. The green curve is with the spin flipper operated at 50% of the power of that in the red curve.

pass into the polarizing magnet; only spin “+” UCN are allowed into the quartz guide. A total fill time of 100 seconds ensures an equilibrium UCN density. The actual density distribution must be modeled by simulations. The AFP spin flipper is turned on for the last 40s of filling in order to build up a population of the opposite spin states (represented by “−” in Table 6.1) in  $V_2$ . We label the volume of the space between the spin flipper and the end of the guide tube as  $V_2$ , the volume between the polarizing magnet and the spin flipper as  $V_1$ , and sum of these two as  $V$ .

### Emptying Stage

The state of the switcher is then changed so that UCN are directed into the PNPI UCN detector. The spin flipper is off during this emptying stage. The “+” spin UCN residing in  $V$  as well as the unpolarized UCN in the upstream are drained into this detector, resulting in the first noticeable peak in Fig 6.8. Meanwhile, the wrong spin “−” UCN are trapped in  $V$ , which is the volume inside the diamond-like carbon/quartz guide and closed by the magnetic potential barrier of the superconducting magnet. At the end of this phase, there remains a “−” spin UCN population of  $N_0$  throughout the volume  $V$ .

### **Spin Flipping Stage (AFP on)**

We then turn on the AFP spin flipper. This immediately induces the second peak in the detector: the “−” spin UCN in  $V_2$  pass through the AFP and transform into “+” spin UCN in  $V_1$  and then are accelerated through the polarizing magnetic field into the PNPI detector. On the other hand, the “−” spin UCN in  $V_1$  remain “−”. They can pass through the AFP and become “+” in  $V_2$ , however, on the next trip from  $V_2$  into  $V_1$  they flip again and become “−” and are still trapped by the polarizer magnet. The “+” in  $V_2$  are also trapped for the same reason. Assuming 100% spin flipping efficiency, UCN are spin flipped every time they pass through the spin flipper and, as a result,  $N_0 \times \frac{V_1}{V}$  UCN are trapped in volume  $V$  (here we assume an uniform UCN density.)

### **Spin Flipper Off**

As soon as we turn off the AFP spin flipper, the spin “+” UCN in  $V_2$  will be drained into the PNPI detector, which then results in the third peak with a count of  $(N_0 \times \frac{V_1}{V}) \times \frac{V_2}{V}$ , whereas the spin “−” UCN are still trapped, and uncounted.

### **6.3.3 Analysis of the Spin Flip Efficiency**

One can extract the efficiency of the spin flipper by comparing the amplitude of the second to the third peak. With a 100% efficiency, the amplitude ratio should be  $\frac{V_1}{V}$  ( $\sim 0.5$ ). The measured value is somewhat smaller, and can be ascribed to the finite spin flip efficiency as well as the population decay during a holding time (AFP on) of  $t$  seconds in the trap. The first effect gives a factor of  $\epsilon^n$ , in which  $\epsilon$  is the spin flip efficiency for a single pass and  $n$  is the number of passes, while the second effect gives a factor of exponential decay  $e^{-t/\tau}$ . (the lifetime  $\tau$  of UCN in the bottle is measured to be 58 seconds.) This number can be estimated by directly dividing the distance traversed (average velocity, 600 cm/s, times the AFP on time,  $t$ .) by the length of the trap, 150 cm, i.e.,

$$n = (600\text{cm/s} \times t) / (150\text{cm}). \quad (6.12)$$

Table 6.2 lists a set of data with a AFP on time  $t$  of 10, 20 and 40 seconds and the deduced efficiency of the spin flip. The uncertainty is only statistical. The data with the longest

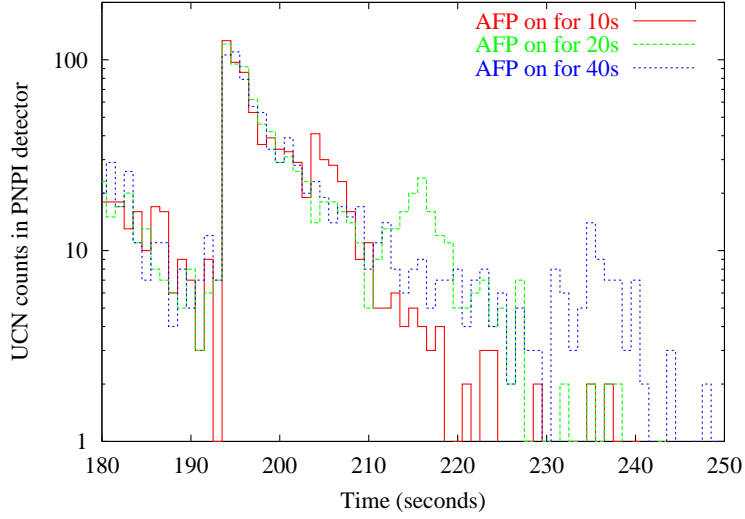


Figure 6.9: UCN counts in the PNPI detector with different AFP on times. Time of trapping for the red, green and blue data sets are 10, 20 and 40 seconds, respectively.

t(sec)	$N_2$	$N_3$	$e^{-t/58}$	$R_{meas}$	$A$	$n$	$\epsilon$	$\Delta\epsilon$
10	126 – 7	41 – 19	0.84	0.22	0.44	40	0.9797	$\pm 0.007$
20	121 – 7	24 – 7	0.708	0.21	0.42	80	0.9892	$\pm 0.004$
40	110 – 7	15 – 1	0.502	0.27	0.54	160	0.9962	$\pm 0.0017$

Table 6.2: Measurements of the spin flip efficiency with different time of trapping (AFP on). The numbers under  $N_2$  and  $N_3$  are the peak counts minus the background counts.

trapping time (40 seconds) gives the most credible measurement of  $99.62\% \pm 0.17\%$ .

To check this extracted number, we study the parameter dependence of the  $\epsilon^n$  model. The efficiency  $\epsilon$  is explicitly expressed as

$$\epsilon = A^{1/n} = \left( \frac{R_{meas}}{R_{100\%}} \right)^{1/n}, \quad (6.13)$$

where  $R_{meas}$  is the measured peak counts ratio between the third and the second peak, including the decay correction, i.e.,

$$R_{meas} = (N_3/N_2)/e^{-t/58}. \quad (6.14)$$

$R_{100\%}$  represents the ideal case with 100% spin flip efficiency and with no neutron loss, and it gives a value of  $\frac{V_1}{V}$  (as shown in Table 6.1). A partial differentiation of Eq.(6.13) gives the sensitivity of the efficiency  $\epsilon$  to  $A$  and  $n$ ,

$$d\epsilon = \frac{1}{n} \frac{A^{1/n}}{A} dA + \frac{1}{n^3} \frac{A^{1/n}}{A} dn. \quad (6.15)$$

In the limit of large  $n$ ,  $A^{1/n} \sim 1$ . The second term is largely suppressed by a fraction of  $n^3$ . The application of the previous crude estimate of  $n$  (Eq.6.12) is thus justified in the case of large  $n$  because in this limit the error in  $n$  does not contribute to the error in  $\epsilon$ . As a result, the uncertainty of  $\epsilon$  is primarily dominated by the uncertainty of  $A$ , weighted by  $1/n$ , leading to a relative uncertainty of  $\epsilon$ :

$$\frac{d\epsilon}{\epsilon} = \frac{1}{n} \frac{dA}{A} = \frac{1}{n} \left( \frac{dR_{meas}}{R_{meas}} + \frac{dR_{100\%}}{R_{100\%}} \right). \quad (6.16)$$

The first term represents the uncertainty in the peak measurements (statistical uncertainty only), and the second term reduces to the uncertainty in volume ( $V_1$ ,  $V_2$  and  $V$ ), which is roughly 10%. In conclusion, the precision of the deduced efficiency extracted from this measurement is statistically limited, giving a relative uncertainty of  $(dA/A)/n = (30\%)/160 = 0.2\%$ . Thus a longer AFP “on” time gives a better measurement of the efficiency.

### 6.3.4 Discussion

The bird cage resonator used in this experiment was built with 16 rungs made of copper tape 15 cm long, 0.625 cm wide, and two 7.5 cm O.D. closed end rings, made of copper tape 1.25 cm wide. We used 47nF capacitors with a rated maximum working voltage of 150V. The fundamental mode was tuned to 1.45 MHz, and was then blue shifted to 1.52 MHz under a co-axially cylindrical metal shield which enclosed the resonator. An oscillating transverse field with a strength of 8 gauss was measured using a 1 cm<sup>2</sup> pick-up coil. The input RF power was approximately 20 Watts. With a Hall probe, the longitudinal holding field gradient in the resonance region was measured to be 1.5 gauss/cm, and the center field strength was measured to be 502 gauss.

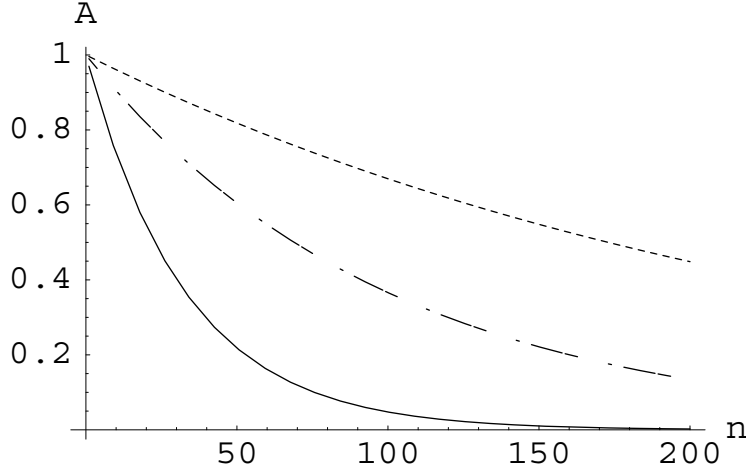


Figure 6.10: The efficiency dependence on the parameter  $n$  and  $A$ . The efficiency  $\epsilon$  for the solid, dash-dotted and dashed curves are 0.97, 0.99 and 0.996, respectively.

The AFP spin flip mechanism requires that the neutron spin adiabatically follow the field direction in the rotating frame. The adiabatic criterion states that the rotation rate of the effective field,  $\Omega$ , has to be much smaller than the Larmor precession of the neutron spin, i.e.,  $\Omega/\gamma H^{eff} \ll 1$ . An evaluation of this criterion gives a measure of the inefficiency of our AFP spin flipper:

$$\begin{aligned}
 1 - \epsilon \sim \frac{\Omega}{\gamma H^{eff}} &= \frac{v H_{\perp} (dH^0/dz) / (H^{eff})^2}{\gamma H^{eff}} \\
 &= \frac{v \frac{dH^0}{dz}}{H_{\perp}^2 \times 2\pi \times 30\text{MHz/Tesla}}. \tag{6.17}
 \end{aligned}$$

With the above measured field conditions, this gives an inefficiency  $(1 - \epsilon)$  of 0.00065, which is a factor of 6 smaller than the measured value (0.0038).

We must also consider the small, but, finite depolarization from the diamond-like carbon surface which might contaminate the spin flip efficiency measurement. A preliminary analysis gives a depolarization probability of approximately 1 part in a million per bounce. With an average UCN velocity of 6 m/s, the transverse velocity  $6 \text{ m/s} \times 1/\sqrt{3} = 3.5 \text{ m/s}$  gives a wall collision frequency  $\sim 45 \text{ Hz} \times 2 = 90 \text{ Hz}$  inside the 7.8 cm I.D. cylinder. This

gives a depolarization time of

$$\frac{1}{10^{-6} \times 45} = 2.2 \times 10^4 \text{ seconds.} \quad (6.18)$$

In a 40 second AFP “on” time, we expect the total population to be reduced by

$$e^{-40/(2.2 \times 10^4)} = 0.9982 \quad (6.19)$$

Without an additional efforts to discriminate these two effects, if we simply analyze this reduction to be the inefficiency of the spin flipper, a spurious measure of spin flip efficiency of  $(0.9982)^{1/160} = 0.999989$  (or  $1.1 \times 10^{-5}$  for  $(1 - \epsilon)$ ) is expected. This correction is approximately two orders of magnitude smaller than the measured value, and thus, the generic depolarization from the storage surface can not directly account for the discrepancy between the measurement and the theoretical prediction.

During the experiment, we noticed that the longitudinal holding field strength fell roughly 10% over a course of several days. This was caused by the time drifting performance of the solenoid magnet power supply (even with current regulated mode). As a result, the spin flip resonant point shifted from the center of the birdcage towards the edge, and at the end of the experiment it was outside of the birdcage. In fact, with a reduced 40% RF field strength (on the edge), the adiabaticity weakens and Eq.(6.17) predicts a spin flip inefficiency matching the experimentally measured value. Note also that we did the field measurement with only half of the aluminum shield on, which introduced an large uncertainty in our knowledge of the AFP field strength. However, our present uncertainty levels do not justify a more precise measurement of the efficiency. Further experiments with an improved control of the field strengths are required to systematically investigate the capability of our AFP technique to produce the predicted spin flip efficiency. In this work, we have demonstrated the viability of the technique of the bird cage resonator, and with it, achieved a spin flip efficiency of higher than 99.6%.

We note that detailed simulations of UCN traversing an AFP spin-flipper operated at 30 MHz with a 5 Gauss field strength in a 60 G/m gradient indicate spin-flip efficiencies better than 99.97%, even when wall collisions (with specular collision occurring 97.5% of



the time) are taken into account. Thus we take our results in these first experiments to be consistent with our anticipated extremely high spin-flip efficiencies in the beta asymmetry experiments.

## Chapter 7

# Conclusion

### 7.1 Conclusions of This Work

We have identified four UCN loss mechanisms in solid deuterium. Our most important discovery is that UCN can upscatter by inducing a para- to ortho-D<sub>2</sub> conversion. We report that this loss gives a UCN lifetime of  $1.2 \pm 0.2$  ms in a pure para-D<sub>2</sub> solid, consistent with our previous calculation. To mitigate this problem of short UCN residence time, we have implemented an ortho/para catalyzed conversion apparatus. A reduction of the para-D<sub>2</sub> concentration from 33.3% to 1.5% was demonstrated using molecular Raman spectroscopy. This optical technique was developed to perform clean and high precision measurements of the ortho-D<sub>2</sub> fraction to 1 part in 10<sup>3</sup>. The instability of the converter performance will need to be addressed for long term operation, and a catalyst which does not strongly perturb the D<sub>2</sub> vapor pressure might be the solution.

We have also identified that solid deuterium exhibits superthermal properties in UCN production at temperatures as low as 5 K. We produced UCN using a prototype S-D<sub>2</sub> source and demonstrated the feasibility of the UCN bottle technique with a pulse timing scheme of spallation source. 1 UCN/cm<sup>3</sup> for every 1  $\mu$ C of protons incident on the spallation W target was stored in a 3.6 liter S.S. bottle placed 1.5 meters above the source. An UCN density of  $98 \pm 5$  cm<sup>-3</sup> was stored in this same bottle in a high current production test.

The  $100\mu\text{C}$  of proton pulse resulted in a measurable heating effect in the solid.

We also investigated superthermal production in solid oxygen. The magnon exchange mechanism yields a large neutron downscattering cross section and the magnon upscattering can be suppressed at temperatures of 2K. A preliminary test demonstrated UCN production from solid oxygen at 5K, however, we have not yet completed systematic studies to test our theoretical predictions.

We also developed a bird cage resonator for adiabatically flipping the UCN spin. We observed a spin flip efficiency of  $99.6 \pm 0.2 \%$ . This device will be useful for the proposed neutron decay experiment using polarized UCN.

## 7.2 A Dedicated UCN Source for the “A” Measurement

With the knowledge and experience we have gained from development work, we are now ready to construct a dedicated UCN source for the proposed experiment measuring the electron asymmetry coefficient “A” of neutron  $\beta$ -decay with UCN.

R. Hill, one of our collaborators, performed a full scale Monte-Carlo simulation of a superthermal UCN source to find the geometry which optimizes UCN production. This Monte-Carlo simulation was calibrated by the experimental results of the prototype. It also reconstructed the UCN trajectories, and with it the stored UCN density of  $1 \text{ UCN cm}^{-3}$  for every  $\mu\text{C}$  of protons was found to produce a UCN density in solid deuterium of  $1100 \text{ UCN cm}^{-3}$  per  $\mu\text{C}$  of protons. First of all, the intensity of the proton current is limited by the radioactivity that developed over time in the spallation tungsten target; the inventory of radionuclides should not exceed the limits above which the source would be declared a Category 3 Nuclear Facility. This gives us an upper bound of  $4\mu\text{A}$  average proton current on the target. A tungsten rod with a 2 cm diameter is designed to fully receive the proton beam and also maximize the neutron leakage from the tungsten. The proton stopping length in tungsten is 17 cm, and thus we make it the length of the tungsten rod. In a new design with an improved cooling power, instead of conduction cooling through the surrounding Be bricks, the tungsten target would be cooled by circulating water. As for cold neutron moderators,

Isotope	$\sigma_{coh}(barns)$	$\sigma_{inc}(barns)$	$\sigma_a(barns)$	$\sigma_s/\sigma_a$	purity(%)	Debye T(K)
$^2D$	5.59	2.04	0.000519	$1.47 \times 10^4$	99.82	110
$^4He$	1.13	0	0	$\infty$	100	20
$^{15}N$	5.23	0.0005	0.000024	$2.1 \times 10^5$	99.9999	80
$^{16}O$	4.23	0	0.00010	$2.2 \times 10^4$	99.95	104
$^{208}Pb$	11.7	0	0.00049	$2.38 \times 10^4$	99.93	105

Table 7.1: Candidates for a superthermal source[27].

polyethylene at 4K is still found to be the best option compared with liquid hydrogen and liquid deuterium at 20K. A cylindrical design of 4K polyethylene to surround the inner 4K solid deuterium cryostat will be preserved. The optimum polyethylene thickness was determined to be 4 cm. One liter of solid deuterium will be placed into a volume with a 4 cm limiting height and a diameter of 15.6 cm.

With the new dimensions mentioned above, assuming good conditions for the S-D<sub>2</sub> (2% of para-D<sub>2</sub>, 0.2% of HD at 5K) the UCN density in the source will be slightly improved to 1280 UCN cm<sup>-3</sup> per  $\mu$ C of protons, and the total UCN yield will have increased by a factor of 2.7 compared with the prototype source.

The storage bottle will be coupled to a 3.3 m long vertical pump-out tube and a 6 m long horizontal tube which feeds UCN into the neutron decay spectrometer volume. The total storage volume will be 35 liters. The input valve is currently designed to be one meter above the solid deuterium. With a 100  $\mu$ C of protons on target and a repetition rate of 0.1 Hz, an equilibrium UCN density of 880 UCN/cm<sup>3</sup> should be achieved in the storage volume. This would give an UCN current of 90,850 UCN/s on the 2 cm diameter exit tube into the neutron decay spectrometer, where a 270 Hz  $\beta$ -decay rate is expected.

### 7.3 Other Superthermal Source Candidates

The figure of merit for a superthermal UCN source is:

$$\sigma_s/\sigma_a. \quad (7.1)$$

The total nuclear scattering cross section,  $\sigma_s$ , characterizes the UCN production power; the nuclear absorption cross section,  $\sigma_a$ , characterizes the UCN loss time which limits the production time. With this figure of merit, we screened several candidate materials. Their cross sections and solid Debye temperatures are listed in table 7.1. We have already discussed solid deuterium and solid oxygen which are also listed in this table. Investigations of the other materials have not yet been reported, and here we will give a brief overview of their potential.

While superfluid  $^4\text{He}$  makes a successful superthermal source, its solid phase has not yet been investigated. Even though it has the smallest Debye temperature of the materials in the table, the phonon dispersion curve in solid He imparts it with a higher UCN production rate than liquid He because there are more channels for coherent neutron downscattering (as discussed in chapter 2). Moreover, the neutron absorption rate is essentially zero and does not limit the source volume. Thus, a solid  $^4\text{He}$  source could be potentially better than its superfluid phase.

A small nuclear absorption cross section (20 times smaller than deuterium) makes  $^{15}\text{N}$  an interesting material. The fully filled neutron shell (8) reduces the possibility of further neutron absorption. Its Debye temperature is slightly lower than that of solid deuterium and its heavier mass further reduces the phonon coupling by a factor of 4. Nevertheless,  $^{15}\text{Ni}$  could produce 5 times more UCN than S-D<sub>2</sub>. On the other hand, a small contamination (one part in  $10^7$ ) of its isotopic partner  $^{14}\text{N}$  would strongly reduce the UCN residence time in a  $^{15}\text{N}_2$  solid because of  $^{14}\text{N}$ 's high nuclear absorption cross section. Thus ultra-high purity  $^{15}\text{N}$  is required for superthermal performance. This makes such a source more difficult to implement.

$^{208}\text{Pb}$  and solid deuterium have similar nuclear absorption cross sections and Debye

temperatures. The natural solid form of  $^{208}\text{Pb}$  would avoid the difficulties of growing cryogenic solids which we experienced with deuterium and oxygen. However, its heavy mass hinders the neutron momentum transfer to the solid phonon field. The heavy mass reduces the phonon creation cross section by  $1/M$ . As a result, one would naively expect its UCN yield to be less than S-D<sub>2</sub> by two orders of magnitude.

One might also imagine that mixtures or molecules consisting of the low  $Z$  elements considered above could be a superthermal source. A set of molecular rotational states with small excitation energies could provide additional energy exchange mechanism. In addition one might also consider a mixture of  $^{15}\text{N}$  with  $^4\text{He}$  which would have a large phonon coupling through  $^{15}\text{N}$  but less sensitivity to the  $^{14}\text{N}$  contamination. The mass difference between the atoms introduces additional incoherent scattering for UCN production. No doubt, as superthermal sources become more commonplace, new approaches to optimizing their performance will present themselves.

## Appendix A

# Neutron scattering from D<sub>2</sub> Molecules

Fermi's golden rule gives a general form for the neutron differential scattering cross section for condensed matter:[31]

$$\frac{d\sigma}{d\Omega dE} = \frac{1}{2\pi\hbar} \frac{k}{k_0} \sum_f \sum_i P_i \int_{-\infty}^{\infty} dt e^{i[\varepsilon - (E_i - E_f)]t/\hbar} \left| \langle \psi_f | \sum_m a_m e^{iQ \cdot x_m} | \psi_i \rangle \right|^2 \quad (\text{A.1})$$

where  $|\psi_i\rangle$  and  $|\psi_f\rangle$  are the initial and final wavefunction of the scatterer, and  $a_m$  is the neutron scattering length which characterizes the strength of the interaction between the incident neutron and the scatterer, labeled by the index  $m$  at position  $x_m$ .  $Q$  is the neutron momentum transfer. The interaction potential of this nuclear scattering is described by a  $\delta$ -function, which is a valid approximation for neutron scattering at the atomic scale. This cross section is evaluated by averaging over the scatterer's initial states, and summing over its available final states. The diagonal terms in the square of the scattering matrix can be selected out, leaving:

$$\begin{aligned} \frac{d\sigma}{d\Omega dE} = & \frac{1}{2\pi\hbar} \frac{k}{k_0} \sum_{f,i} P_i \int_{-\infty}^{\infty} dt e^{i[\varepsilon - (E_i - E_f)]t/\hbar} \sum_{m \neq l} \langle \psi_f | a_m^* e^{-iQ \cdot x_m} | \psi_i \rangle \langle \psi_i | a_l e^{iQ \cdot x_l} | \psi_f \rangle \\ & + \frac{1}{2\pi\hbar} \frac{k}{k_0} \sum_{f,i} P_i \int_{-\infty}^{\infty} dt e^{i[\varepsilon - (E_i - E_f)]t/\hbar} \sum_m \langle \psi_f | a_m^* e^{-iQ \cdot x_m} | \psi_i \rangle \langle \psi_i | a_m e^{iQ \cdot x_m} | \psi_f \rangle. \quad (\text{A.2}) \end{aligned}$$

We will consider only the diagonal terms (the second term in Eq.(A.2)), which represents the sum of self contributions from individual scatterers, and neglect the interference term of scattered waves from different scatterers (the first term).

A diatomic molecule  $m$  has two scatterers at coordinates  $x_{m1} = R_m + r_m/2$  and  $x_{m2} = R_m - r_m/2$ . Here  $R_m$  is the center of mass position vector of molecule  $m$ , and  $r_m$  is the separation vector of the two nuclei. If the internal wavefunction is not effected by the position of the scatterer, in the other words, the internal degrees of freedom commute with the scatterer's translational degree of freedom, i.e.,  $[R_m, r_m] = 0$ , then it is valid to separate the scatterers total wavefunction into a translational wavefunction times a molecular wavefunction i.e.,  $|\psi\rangle = |\psi_T\rangle|\psi_M\rangle$ . This is approximately true in the case of a deuterium molecular crystal[32]. The self-cross section can thus be represented as:

$$\begin{aligned} & \left( \frac{d\sigma}{d\Omega dE} \right)_{self} \\ &= \frac{1}{2\pi\hbar} \frac{k}{k_0} \int_{-\infty}^{\infty} dt e^{i[\varepsilon - (E_i - E_f)]t/\hbar} \sum_m \langle \psi_{iT} | e^{-iQ \cdot R_m} e^{iQ \cdot R_m} | \psi_{iT} \rangle \times \\ & \sum_{f,i} P_i \left| \langle \psi_{fM} | (a_{m1} e^{iQ \cdot r_m} + a_{m2} e^{-iQ \cdot r_m}) | \psi_{iM} \rangle \right|^2. \end{aligned} \quad (A.3)$$

The wavefunction for a molecule,

$$|\psi_M\rangle = |JJ_z, SS_z, n; \frac{1}{2}\sigma_z\rangle, \quad (A.4)$$

is characterized by an orbital angular momentum  $J$ , a total nuclear spin  $S$ , and a vibrational quantum number  $n$ . We explicitly include the spin  $\sigma$  of the scattering neutron because the nuclear strong force is spin-dependent. The spin-dependent nuclear scattering cross section for a neutron scattering from one nucleus with spin  $I$  is:

$$a = \frac{I+1+2\mathbf{I} \cdot \boldsymbol{\sigma}}{2I+1} a_+ + \frac{I-2\mathbf{I} \cdot \boldsymbol{\sigma}}{2I+1} a_-. \quad (A.5)$$

Here  $a_+$  and  $a_-$  represent the triplet and singlet scattering cross sections of the nuclei-neutron system with total spin  $S = \vec{1} + \vec{\frac{1}{2}} = \vec{\frac{3}{2}}$  (triplet) or  $\vec{\frac{1}{2}}$  (singlet). Combining the above



information, the molecular part of Eq.(A.3) can be evaluated:

$$\begin{aligned}
& \sum_{f,i} P_i \left| \langle \psi_{fM} | a_1 e^{iQ \cdot \frac{r}{2}} + a_2 e^{-iQ \cdot \frac{r}{2}} | \psi_{iM} \rangle \right|^2 \\
&= \left( \sum_{\sigma'_z = \pm \frac{1}{2}} \sum_{J', J'_z} \sum_{S', S'_z} \sum_{n'} \right) \left( \sum_{\sigma_z = \pm \frac{1}{2}} \sum_{J, J_z} \sum_{S, S_z} \sum_n \right) \frac{1}{2} \frac{1}{2J+1} \frac{1}{2S+1} P_{JS} P_n \\
& \left| \langle J' J'_z, S' S'_z, n'; \frac{1}{2} \sigma'_z | \{ 2a_{coh} \cos(Q \cdot \frac{r}{2}) + \frac{2}{\sqrt{I(I+1)}} a_{inc} [\vec{S} \cdot \vec{\sigma} \cos(Q \cdot \frac{r}{2}) \right. \right. \\
& \quad \left. \left. + i(\vec{I}_1 - \vec{I}_2) \cdot \vec{\sigma} \sin(Q \cdot \frac{r}{2}) \} | J J_z, S S_z, n; \frac{1}{2} \sigma_z \rangle \right|^2 \tag{A.6}
\end{aligned}$$

The index  $m$  drops out because molecules in every scattering site are the same. We introduce the coherent and incoherent scattering length of a deuterium nucleus,

$$\begin{aligned}
a_{coh} &= \frac{(I+1)a_+ + I a_-}{2I+1} \\
a_{inc} &= \frac{\sqrt{I(I+1)}(a_+ - a_-)}{2I+1}, \tag{A.7}
\end{aligned}$$

to replace the singlet and triplet scattering length. Between the bra and ket, the exponential operators are decomposed into even sine and odd cosine functions weighted by the spin operators.

For transitions between states with the same parity, only cosine terms,  $\cos(Q \cdot \frac{r}{2})$ , survive the scalar product in Eq.(A.6). The spinor wave function and the dynamical wave function can be further separated:

$$\begin{aligned}
& \frac{1}{2J+1} \sum_{J'_z, J_z} \left| \langle J' J'_z, n' | \cos(Q \cdot \frac{r}{2}) | J J_z, n \rangle \right|^2 \times \frac{1}{2S+1} \sum_{S', S} \sum_{\sigma'_z, \sigma_z} \sum_{S'_z, S_z} \\
& \left| \langle S' S'_z; \frac{1}{2} \sigma'_z | (a_{coh} + \frac{a_{inc}}{\sqrt{I(I+1)}} \vec{S} \cdot \vec{\sigma}) | S S_z, \frac{1}{2} \sigma_z \rangle \right|^2 \\
&= \frac{1}{2J+1} \sum_{J'_z, J_z} \left| \langle J' J'_z, n' | \cos(Q \cdot \frac{r}{2}) | J J_z, n \rangle \right|^2 \times \frac{1}{2S+1} \sum_{S', S} \sum_{\sigma_z} \sum_{S_z} \\
& \langle S S_z; \frac{1}{2} \sigma_z | (a_{coh} + \frac{a_{inc}}{\sqrt{I(I+1)}} \vec{S} \cdot \vec{\sigma})^2 | S S_z; \frac{1}{2} \sigma_z \rangle \\
&= \frac{1}{2J+1} \sum_{J'_z, J_z} \left| \langle J' J'_z, n' | \cos(Q \cdot \frac{r}{2}) | J J_z, n \rangle \right|^2 \times \frac{1}{2S+1} \sum_{S', S} \\
& \left[ 2(2S+1)a_{coh}^2 + (2S+1)\frac{a_{inc}^2}{I(I+1)} \frac{1}{2} S(S+1) \right]. \tag{A.8}
\end{aligned}$$

$\sum'$  stands for a summation over the allowable spin states, which are restricted by the rotational symmetry. In the above calculation, the completeness relation of spin states has been utilized when summing over  $\sigma'_z$  and  $S'_z$ . The cross term  $(\vec{S} \cdot \vec{\sigma})$  in Eq.(A.8) vanishes when summed over both neutron spin states, whereas the  $(\vec{S} \cdot \vec{\sigma})^2$  term can be evaluated:

$$\sum_{\sigma_z} \langle \sigma_z | (\vec{\sigma} \cdot \vec{I}_\nu) (\vec{\sigma} \cdot \vec{I}_\mu) | \sigma_z \rangle = \frac{1}{2} \vec{I}_\nu \cdot \vec{I}_\mu. \quad (\text{A.9})$$

Similarly, the  $\sin(Q \cdot \frac{r}{2})$  term couples rotational states with opposite parities and can be reduced to

$$\begin{aligned} & \frac{1}{2J+1} \sum_{J'_z, J_z} \left| \langle J' J'_z, n' | \sin(Q \cdot \frac{r}{2}) | J J_z, n \rangle \right|^2 \times \frac{1}{2S+1} \sum'_{S', S} \\ & \left[ (2S+1) \frac{a_{inc}^2}{I(I+1)} \frac{1}{2} (2(I_1(I_1+1) + I_2(I_2+1)) - S(S+1)) \right]. \end{aligned}$$

Note that this term accounts for ortho/para conversion and exists only when the target has a non-zero incoherent scattering length.  $a_{inc}$  results from interaction strength difference between the spin sub-states(Eq.(A.7)). Thus, a large incoherent scattering length leads to a higher spin flip probability.

The argument in the sine and cosine functions can be rewritten with a change of coordinate,  $\mu = \cos(\theta)$  and  $r = a + i \frac{1}{\sqrt{Mw}}(b - b^+)$ , where the internal motion in coordinate  $r$  is described by a simple harmonic oscillator to first order and  $b$  and  $b^+$  are the creation and annihilation operators of such oscillation modes. The dynamic part involving cosine in

Eq.(A.8) can be evaluated accordingly:

$$\begin{aligned}
& \sum_{J_z, J'_z} \left| \langle J' J'_z | \langle n' | \cos(Q \cdot \frac{r}{2}) | n \rangle | J J_z \rangle \right|^2 \\
&= \sum_{J_z, J'_z} \left| \frac{1}{2} \langle J' J'_z | \langle n' | \left\{ e^{i \frac{Q_a}{2} \mu} e^{-\frac{Q\mu}{2} \frac{1}{\sqrt{Mw}} (b-b^+)} + e^{-i \frac{Q_a}{2} \mu} e^{+\frac{Q\mu}{2} \frac{1}{\sqrt{Mw}} (b-b^+)} \right\} | n \rangle | J J_z \rangle \right|^2 \\
&= \sum_{J_z, J'_z} \left| \frac{1}{2} \langle J' J'_z | e^{-\frac{Q^2 \mu^2}{8Mw}} \sqrt{\frac{n!}{n'!}} \left( \frac{Q\mu}{2} \frac{1}{\sqrt{Mw}} \right)^{\Delta n} \left[ e^{i \frac{Q_a}{2} \mu} + (-1)^{\Delta n} e^{-i \frac{Q_a}{2} \mu} \right] | J J_z \rangle \right|^2 \\
&= \left( \frac{Q^2}{4Mw} \right)^{\Delta n} \frac{n!}{n'!} \sum_{J_z, J'_z} \left| \langle J' J'_z | \mu^{\Delta n} e^{-\frac{Q^2 \mu^2}{8Mw}} e^{i \frac{Q_a}{2} \mu} | J J_z \rangle \right|^2 \\
&= \left( \frac{Q^2}{4Mw} \right)^{\Delta n} \frac{n!}{n'!} \sum_{J_z, J'_z} \left| \int d\Omega \mu^{\Delta n} e^{-\frac{Q^2 \mu^2}{8Mw} + i \frac{Q_a}{2} \mu} Y_{J' J'_z}^*(\theta, \phi) Y_{J J_z}(\theta, \phi) \right|^2 \\
&= \left( \frac{Q^2}{4Mw} \right)^{\Delta n} \frac{n!}{n'!} \sum_{J_z, J'_z} \left| \int d\Omega \mu^{\Delta n} e^{-\frac{Q^2 \mu^2}{8Mw} + i \frac{Q_a}{2} \mu} \times \right. \\
&\quad \left. \delta_{J'_z J_z} (-1)^{J'_z} \sum_{l=|J'-J|}^{J'+J} \sqrt{\frac{(2J+1)(2J'+1)}{4\pi(2l+1)}} C(J J' l; 00) Y_{l, J_z - J'_z}(\theta, \phi) \right|^2 \\
&= \left( \frac{Q^2}{4Mw} \right)^{\Delta n} \frac{n!}{n'!} \frac{(2J+1)(2J'+1)}{4} \sum_{l=|J'-J|}^{J'+J} |A_{\Delta n l}|^2 C^2(J J' l; 00). \tag{A.10}
\end{aligned}$$

The function  $A_{nl}$  is defined as:

$$A_{nl} = \int_{-1}^1 2\pi d\mu \mu^n e^{-\frac{Q^2 \mu^2}{8Mw} + i \frac{Q_a}{2} \mu} P_l(\mu) \sqrt{\frac{2l+1}{4\pi}}. \tag{A.11}$$

When  $n = 0$  (the vibrational ground state),  $A_{nl}$  reduces to a spherical Bessel function:

$$A_{0l} = 2i^l j_l\left(\frac{Qa}{2}\right). \tag{A.12}$$

In Eq.(A.10), we expand the position operator  $x$  into normal modes of vibration, and apply the creation and annihilation operator algebra. The spherical harmonic solutions in a central force field are invoked for the final solid angle integration. The spherical harmonic functions reduce the angular integration into single Legendre polynomials which are left in the final form of  $A_{nl}$ . For this even cosine contribution, because  $J$  has the same parity before and after scattering, the change in  $n$ ,  $\Delta n$ , can only be even. The sine term can be similarly reduced. The self differential scattering cross section(Eq.(A.3)) of molecular deuterium is

thus summarized as:

$$\begin{aligned}
& \left( \frac{d\sigma}{d\Omega dE} \right)_{self}^{para} (J = odd; S = 1) \\
&= \frac{1}{2\pi\hbar} \frac{k}{k_0} \int_{-\infty}^{\infty} dt e^{i[\varepsilon - (E_{iT} - E_{fT})]t/\hbar} \sum_m \langle \psi_{iT} | e^{-iQ \cdot R_m(t)} e^{iQ \cdot R_m} | \psi_{iT} \rangle \times \\
& \sum_{J=1,3,5..} \frac{1}{2} P_{JS} \sum_{n,n'} P_n e^{i\Delta n \omega t} \left( \frac{Q^2}{4Mw} \right)^{\Delta n} \frac{n!}{n'!} \left[ \sum_{J'=0,2,4..; S'=0,2} 12a_{inc}^2 + \right. \\
& \left. \sum_{J'=1,3,5..; S'=1} (4a_{coh}^2 + a_{inc}^2) \right] \frac{(2J' + 1)}{4} e^{i(E'_J - E_J)t/\hbar} \sum_{l=|J'-J|}^{J'+J} |A_{\Delta nl}|^2 C^2(JJ'l; 00)
\end{aligned}$$

$$\begin{aligned}
& \left( \frac{d\sigma}{d\Omega dE} \right)_{self}^{ortho} (J = even; S = 0, 2) \\
&= \frac{1}{2\pi\hbar} \frac{k}{k_0} \int_{-\infty}^{\infty} dt e^{i[\varepsilon - (E_{iT} - E_{fT})]t/\hbar} \sum_m \langle \psi_{iT} | e^{-iQ \cdot R_m(t)} e^{iQ \cdot R_m} | \psi_{iT} \rangle \times \\
& \sum_{J=0,2,4..} \frac{1}{2} P_{JS} \sum_{n,n'} P_n e^{i\Delta n \omega t} \left( \frac{Q^2}{4Mw} \right)^{\Delta n} \frac{n!}{n'!} \left[ \sum_{J'=0,2,4..; S'=0,2} (4a_{coh}^2 + \frac{5}{2}a_{inc}^2) + \right. \\
& \left. \sum_{J'=1,3,5..; S'=1} (\frac{3}{2}a_{inc}^2) \right] \frac{(2J' + 1)}{4} e^{i(E'_J - E_J)t/\hbar} \sum_{l=|J'-J|}^{J'+J} |A_{\Delta nl}|^2 C^2(JJ'l; 00)
\end{aligned}$$

We expand the cross section presented above, given by Koppel and Young [31], to the case of neutron scattering in a crystal: The translational part  $\langle \psi_{iT} | e^{-iQ \cdot R_m(t)} e^{iQ \cdot R_m} | \psi_{iT} \rangle$  can be evaluated following the formal phonon expansions in the harmonic approximation. As a result, for incoherent elastic scattering, we come to the following expressions:

$$\begin{aligned}
& \left( \frac{d\sigma}{d\Omega dE} \right)_{para}^{incoherent, elastic} (J = odd; S = 1) \\
&= \frac{1}{2\pi\hbar} \frac{k}{k_0} \frac{1}{N} \sum_i e^{-2W_i(Q)} \sum_{\Delta E} \delta(E - \Delta E) \times \\
& \sum_{J=1,3,5..} \frac{1}{2} P_{JS} \sum_{n,n'} P_n \left( \frac{Q^2}{4Mw} \right)^{\Delta n} \frac{n!}{n'!} \left[ \sum_{J'=0,2,4..; S'=0,2} (12a_{inc}^2) + \right. \\
& \left. \sum_{J'=1,3,5..; S'=1} (4a_{coh}^2 + a_{inc}^2) \right] \frac{(2J' + 1)}{4} \sum_{l=|J'-J|}^{J'+J} |A_{\Delta nl}|^2 C^2(JJ'l; 00)
\end{aligned}$$

$$\begin{aligned}
& \left( \frac{d\sigma}{d\Omega dE} \right)_{ortho}^{incoherent, elastic} (J = \text{even}; S = 0, 2) \\
&= \frac{1}{2\pi\hbar} \frac{k}{k_0} \frac{1}{N} \sum_i e^{-2W_i(Q)} \sum_{\Delta E} \delta(E - \Delta E) \times \\
& \sum_{J=0,2,4..} \frac{1}{2} P_{JS} \sum_{n,n'} P_n \left( \frac{Q^2}{4Mw} \right)^{\Delta n} \frac{n!}{n'!} \left[ \sum_{J'=0,2,4..; S'=0,2} (4a_{coh}^2 + \frac{5}{2}a_{inc}^2) + \right. \\
& \left. \sum_{J'=1,3,5..; S'=1} \left( \frac{3}{2}a_{inc}^2 \right) \right] \frac{(2J'+1)}{4} \sum_{l=|J'-J|}^{J'+J} |A_{\Delta nl}|^2 C^2(JJ'l; 00)
\end{aligned}$$

These two are transitions with internal rotational and vibrational excitations, but without phonon excitations. For scattering process with one phonon exchange, the cross sections become:

$$\begin{aligned}
& \left( \frac{d\sigma}{d\Omega dE} \right)_{para}^{incoherent, \pm 1 \text{ phonon}} (J = \text{odd}; S = 1) \\
&= \frac{k}{k_0} \left( \frac{\hbar Q^2}{2M} \right) \frac{1}{4\pi} e^{-2W(Q)} \sum_{\Delta E} \frac{\langle n+1 \rangle}{E} Z(E) \times \\
& \sum_{J=1,3,5..} \frac{1}{2} P_{JS} \sum_{n,n'} P_n \left( \frac{Q^2}{4Mw} \right)^{\Delta n} \frac{n!}{n'!} \left[ \sum_{J'=0,2,4..; S'=0,2} (12a_{inc}^2) + \right. \\
& \left. \sum_{J'=1,3,5..; S'=1} (4a_{coh}^2 + a_{inc}^2) \right] \frac{(2J'+1)}{4} \sum_{l=|J'-J|}^{J'+J} |A_{\Delta nl}|^2 C^2(JJ'l; 00) \\
\\
& \left( \frac{d\sigma}{d\Omega dE} \right)_{ortho}^{incoherent, \pm 1 \text{ phonon}} (J = \text{even}; S = 0, 2) \\
&= \frac{k}{k_0} \left( \frac{\hbar Q^2}{2M} \right) \frac{1}{4\pi} e^{-2W(Q)} \sum_{\Delta E} \frac{\langle n+1 \rangle}{E} Z(E) \times \\
& \sum_{J=0,2,4..} \frac{1}{2} P_{JS} \sum_{n,n'} P_n \left( \frac{Q^2}{4Mw} \right)^{\Delta n} \frac{n!}{n'!} \left[ \sum_{J'=0,2,4..; S'=0,2} (4a_{coh}^2 + \frac{5}{2}a_{inc}^2) + \right. \\
& \left. \sum_{J'=1,3,5..; S'=1} \left( \frac{3}{2}a_{inc}^2 \right) \right] \frac{(2J'+1)}{4} \sum_{l=|J'-J|}^{J'+J} |A_{\Delta nl}|^2 C^2(JJ'l; 00)
\end{aligned}$$

The phonon density of state,  $Z(E)$ , and the phonon occupation number,  $n$ , are introduced into the above expressions. The cross sections are numerically integrated. The cross sections of ortho-deuterium are comparable to those of para-deuterium for thermal neutrons ( $\sim 3$  barns), but, for neutron with energies below .003eV the ortho-deuterium cross section drops to 1 barn due to intermolecular interference[102].

## Appendix B

# Para-D<sub>2</sub> Neutron Upscattering

In this section, we demonstrate that even very small concentrations of para-D<sub>2</sub> (with total nuclear spin 1) can dominate the UCN upscattering rate, overwhelming the usual phonon annihilation mechanism. This results in a greatly reduced UCN lifetime in the solid and a two order of magnitude reductions in the achievable UCN density.

The deuterium molecule is a two-body system with the quantum properties of identical bosons. Its nuclear spin wavefunction couples to molecular rotational states of the same parity to preserve the symmetry of the wavefunction under permutation of identical particles. Koppel and Young [31] calculated the neutron scattering cross-section of this molecular system, taking into consideration induced transitions between molecular rotational and vibrational states (presented in appendix A, too). They used an incoherent approximation and assumed that translational coordinates commute with inter-molecular degrees of freedom. The derived double differential cross-section which neglects the interference term has

Table B.1: The intrinsic scattering cross-sections  $\mathcal{S}_{JJ'}$  associated with different rotational transitions [93].

$\mathcal{S}_{JJ'}$	Even-J(Ortho)	Odd-J(Para)
Even-J'	$a_{coh}^2 + \frac{5}{8}a_{inc}^2 = 6.687/4\pi$	$\frac{3}{4}a_{inc}^2 = 1.530/4\pi$
Odd-J'	$\frac{3}{8}a_{inc}^2 = 0.765/4\pi$	$a_{coh}^2 + \frac{1}{4}a_{inc}^2 = 6.102/4\pi$

the form, for UCN with incident wavenumber  $k$  and final wavenumber  $k'$ :

$$\begin{aligned}
\frac{d^2\sigma}{d\Omega d\epsilon} &= \frac{1}{2\pi\hbar} \frac{k'}{k} \int_{-\infty}^{\infty} dt \\
&\sum_l \langle \phi_{it} | e^{-i\kappa \cdot r_l(0)} e^{i\kappa \cdot r_l(t)} | \phi_{it} \rangle_{Trans} \\
&\times \sum_J P_{JS} \sum_{J'} \mathcal{S}_{JJ'} (2J' + 1) e^{i(E_{J'} - E_J)t/\hbar} \\
&\times \sum_{n=0} \frac{e^{in\omega t}}{n!} \left( \frac{\hbar^2 \kappa^2}{2M_{D_2} \hbar\omega} \right)^n \sum_{l=|J'-J|}^{J'+J} |A_{nl}|^2 C^2(JJ'l; 00). \tag{B.1}
\end{aligned}$$

Where  $\hbar\kappa$  is the momentum transfer of the scattered neutron,  $P_{JS}$  is the population of the initial molecular state with a total nuclear spin  $S$  and rotational quantum number  $J$ ,  $E_J = 7\text{meV} \times J(J+1)/2$  is the rotational spectrum,  $\hbar\omega$  is the inter-molecular vibrational energy with  $n$  characterizing the number of vibrational energy quanta, and  $C(JJ'l; 00)$  is a Clebsh-Gordon coefficient.  $A_{nl}$  is defined as an integral over the orientation of a molecule, i.e.,

$$A_{nl} = \int_{-1}^1 d\mu \mu^n \exp\left(-\frac{\hbar\kappa^2 \mu^2}{4M_{D_2}\omega} + \frac{i\kappa a \mu}{2}\right) P_l(\mu), \tag{B.2}$$

with  $a = 0.74\text{\AA}$  the equilibrium separation distance of the D-D bond,  $\mu$  the cosine of the inclination angle of the molecular axis from the  $z$  axis of a reference Euclidean coordinate system, and  $P_l$  a Legendre polynomial of order  $l$ .

Koppel and Young also deduced input parameter  $\mathcal{S}_{JJ'}$  (in units of barns) in (B.1) for transitions between different rotational states (listed in table B.1). Note that only the incoherent scattering length  $a_{inc}$  of a bound nuclide contributes to the ortho(even  $J$ )/para(odd  $J$ ) conversion.

In a D<sub>2</sub> solid, the population of the even- $J$ (ortho state) and the odd- $J$ (para state) are

determined by the ortho/para population of the gas phase before the D<sub>2</sub> is frozen into the solid. The self-conversion of these two species in the solid phase is extremely slow compared with the time scale of an experiment. For example, a room temperature equilibrium D<sub>2</sub> is a mixture of 67% ortho-D<sub>2</sub> and 33% para-D<sub>2</sub>. The conversion rate in the solid is measured to be 0.06%/hr [94]. 7 months are required to reduce the para concentration from 33.3% to 1.65%. On the other hand, relaxation to thermal distributions in the rotational states is rapid within ortho- and para- families. Consequently, in low temperature circumstances relevant to super-thermal solid deuterium source (T < 20K), only ground states ( $J = 0$  for ortho;  $J = 1$  for para) are present.

In the case of neutrons scattered from a low temperature crystal with well-defined lattice structures, harmonic solid correlation functions should be applied to the translational part of (B.1). Following the standard treatment of lattice dynamics [33], we perform a phonon expansion

$$\begin{aligned} & \langle \exp\{-i\kappa \cdot r_l\} \exp\{i\kappa \cdot r_{l'}(t)\} \rangle_{Trans} \\ &= \exp\{-2W(\kappa)\} \exp\{\langle \kappa \cdot u_l \kappa \cdot u_{l'}(t) \rangle\} \\ &= \exp\{-2W(\kappa)\} \left[ 1 + \langle \kappa \cdot u_l \kappa \cdot u_{l'}(t) \rangle + O(\langle \kappa \cdot u_l \kappa \cdot u_{l'}(t) \rangle^2) \right]. \end{aligned}$$

An overall Debye-Waller factor is extracted in front, and only the first two terms are left for discussion, yielding the zero and one phonon exchange processes, respectively.

Unlike the conventional applications of elastic solid correlation functions, the first term in the phonon expansion (zero phonon term) coupled to molecular internal energy states not only gives rise to UCN energy transitions (mainly upscattering), but overwhelms any phonon contributions when para-D<sub>2</sub> is present. The conversion of para- into ortho- molecules provides direct energy transfer to UCN. This scattering cross-section without phonon couplings has the simple form:

$$\begin{aligned} \left( \frac{d\sigma}{d\Omega} \right)_{J=1 \rightarrow 0}^{0 \text{ phonon}} &= \frac{3}{4} a_{inc}^2 \frac{k'}{k} e^{-2W(\kappa)} \\ &\times \left[ 4j_1^2 \left( \frac{\kappa a}{2} \right) C^2(101; 00) \right], \end{aligned} \quad (\text{B.3})$$



where  $j_1(\frac{\kappa a}{2})$  is a spherical Bessel function of order one[74]. The increase of the neutron momentum is definite, i.e.,

$$k' = \sqrt{2m_n \Delta E_{10}} / \hbar. \quad (\text{B.4})$$

A conversion energy  $\Delta E_{10}$  of 7 meV gives  $k'$  a value of  $1.84 \times 10^{10} \text{ m}^{-1}$ . The momentum transfer  $\kappa$  can be well-approximated by  $k'$  for UCN ( $k' \gg k_{ucn} = 1.27 \times 10^8 \text{ m}^{-1}$ ), and the above differential cross-section is isotropic, making the integration of (B.3) straightforward. A Debye-Waller factor originating from uncertainty in the positions of lattice sites reduces the amplitude by a factor of 0.76. The temperature independent<sup>1</sup> total cross section of UCN upscattering  $\sigma_{10}$  from para-D<sub>2</sub> is calculated to be 31 barns. This is at least an order of magnitude larger than the phonon annihilation cross-section in a 4K solid.

The rate of UCN loss in the solid is

$$\dot{\rho}_{ucn} = \rho_{ucn} (\sigma_{10} v_{ucn} \rho'). \quad (\text{B.5})$$

Here  $\rho'$  is the density of para-D<sub>2</sub>, taken to be  $3 \times 10^{22} \text{ cm}^{-3}$ . The corresponding upscattering time  $\tau_{up}$  of UCN in a pure para-D<sub>2</sub> molecular solid is therefore

$$\begin{aligned} \tau_{up} &= \frac{1}{\sigma_{10} v_{ucn} \rho'}, \\ &= 1.5 \quad \text{msec.} \end{aligned}$$

For normal-D<sub>2</sub> which retains the room temperature equilibrium ortho/para ratio, the up-scattering time due to the spin relaxation of the para species is 4.6 msec.

To estimate the phonon upscattering rates, we approximate the S-D<sub>2</sub> hcp/fcc lattice as a cubic lattice to simplify the treatment of polarization anisotropies. The expression for the

---

<sup>1</sup>The only temperature dependence comes from a roughly 5% decrease in the Debye-Waller factor between 4 and 18K.

incoherent double differential cross-section involving one phonon exchange is

$$\begin{aligned}
& \left( \frac{d^2\sigma}{d\Omega dE'} \right)_{J \rightarrow J'}^{1 \text{ phonon}} = \frac{k'}{k} \frac{\hbar^2 \kappa^2}{2M_{D_2}} e^{-2W(\kappa)} \mathcal{S}_{JJ'}(2J' + 1) \\
& \times \sum_n \left( \frac{\hbar \kappa^2}{2M_{D_2} \omega} \right)^n \frac{1}{n!} \sum_{l=|J'-J|}^{J'+J} |A_{nl}|^2 C^2(JJ'l; 00) \\
& \times \frac{Z(E_{ph})}{E_{ph}} \begin{cases} n(E_{ph}) + 1 & \text{if } E_{ph} \geq 0 \\ n(E_{ph}) & \text{if } E_{ph} < 0, \end{cases} \tag{B.6}
\end{aligned}$$

where the phonon energy is determined by the energy conservation law, giving  $E_{ph} = \epsilon + \Delta E(J' \rightarrow J) + n\hbar\omega$ . Positive and negative values of  $E_{ph}$  correspond to single phonon creation and annihilation, respectively.  $Z(E)$  represents the normalized phonon density of states and  $n(E)$  represents the occupation number of phonons with energy  $E$ .

In a simple Debye model, in which,

$$Z(E) = \frac{3E^2}{(k_B T_\Theta)^3}, \tag{B.7}$$

and the Debye temperature  $T_\Theta$  (110K for D<sub>2</sub>) is the only parameter, a double integration of (B.6) with the initial energy of UCN (see Figure 2.6) reproduces the upscattering cross-sections in ortho-deuterium calculated by Yu, Malik and Golub [26], who did not consider rotational transitions. In an ortho-D<sub>2</sub> solid, the  $J = 0 \rightarrow 0$  process dominates the upscattering. Even though the  $J = 0 \rightarrow 1$  transition is energetically allowed through coupling to a phonon, the cross-section is kinematically suppressed by the smaller final phase space of upscattered neutrons. Para-D<sub>2</sub> has a distinguishably larger one-phonon annihilation cross-section than the ortho species. The origin of this difference is again related to the  $J = 1 \rightarrow 0$  relaxation channel. This provides UCN with additional energy to scatter into a larger volume of phase space, and it couples UCN to high energy phonons with a large density of states, and thus, is less restricted by the availability of phonon modes than the  $J = 1 \rightarrow 1$  process. However, it is still suppressed by its small coupling to the phonon field, as opposed to the zero phonon term.

In summary, para-deuterium has a spin relaxation channel in which its conversion energy of 7 meV can be released to UCN, resulting in a temperature-independent short UCN

lifetime of 4.6 msec in a normal-D<sub>2</sub> solid. Elimination of para-D<sub>2</sub> is necessary in order to achieve UCN lifetimes comparable to the nuclear absorption time in solid D<sub>2</sub>.

## Appendix C

# The Incoherent Approximation

Here we present an estimation of the coherent cross section Eq.(2.18) in the case of polycrystal scattering or  $4\pi$  neutron flux scattering. We analyze the allowed momentum phase space, incorporating the effect of the inverse lattice momentum, and develop an analytical form for the density of states for coherent inelastic phonon scattering. The total coherent cross section is thus approximated by a single energy integration, which is compared with the results of the incoherent approximation results. Even though a precise calculation can be easily performed by an integration routine (see Sec. 5.2.2) with the computation power of modern computers, the practice presented here helps one develop an intuitive physics picture for coherent processes.

Bloch's theorem states that the periodic structure of a crystal lattice introduces a gauge transformation, which leaves the physics unchanged under translations to any lattice site. This introduces the inverse lattice momentum,  $\boldsymbol{\tau}$ , which is integer multiple of the inverse lattice vectors, into the momentum conservation law in the process of neutron scattering, i.e.,

$$\mathbf{k}_i = \mathbf{k}_f + \mathbf{q}_{phonon} \pm \boldsymbol{\tau}, \quad (\text{C.1})$$

where  $\mathbf{k}_i$  and  $\mathbf{k}_f$  are the initial and final momentum of neutron, and  $\mathbf{q}_{phonon}$  is the momentum of the created phonon.

Because of the inverse lattice momentum, more phonon modes are accessible for coherent

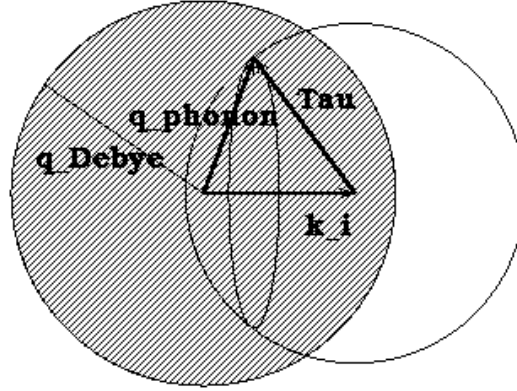


Figure C.1: A schematic of scattering vectors in a coherent process.

scattering than momentum conservation in free space would suggest. Moreover, in the case of polycrystals with random crystal orientations, even more phonon mode are accessible because  $\tau$  can points to any direction. The inverse lattice momentum becomes a radial vector pointing isotropically onto a spherical surface with a radius of the inverse lattice constant. The phonon coupling can be maximized as illustrated in Fig.C.1. In the case of UCN production,  $\mathbf{k}_f$  is neglected, and Eq.(C.1) becomes

$$\mathbf{k}_i + \boldsymbol{\tau} = \mathbf{q}_{phonon} \quad (\text{C.2})$$

The vector sum of  $\mathbf{k}_i$  and  $\boldsymbol{\tau}$  must fall within the phonon momentum sphere which has a radius of Debye momentum  $q_\Theta$ . The intersection of a spherical shell with radius  $\tau$  and a sphere with radius  $q_\Theta$  each separated by  $k_i$  defines a surface on the  $\tau$  sphere. Phonons on this surface satisfy conditions of the momentum conservation (Eq.(C.2)). By further imposing energy conservation, which requires a full energy transfer from the incident neutron to the created phonon, we limit the values of  $q_{phonon}$  and identify a circle of phonons in the three dimensional momentum space. This is the familiar representation of the scattering cone of a polycrystal sample. The resultant phonon states satisfy the kinematics of the neutron scattering, and their momentum is not necessarily the same as the initial neutron momentum  $\mathbf{k}_i$ .

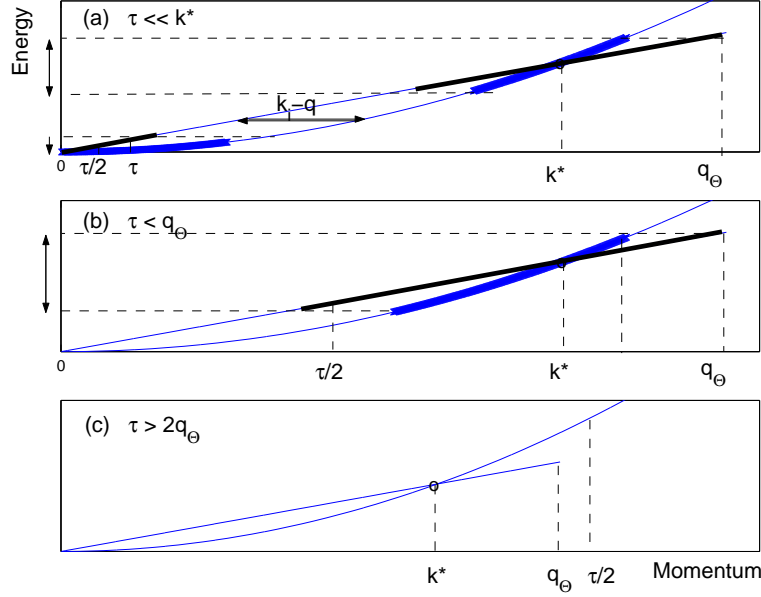


Figure C.2: A schematic of different crystal parameters. (a) Small lattice constant  $\tau \ll k^*$ . (b) lattice constant  $\tau < q_\Theta$ . (c) Large lattice constant  $\tau > 2q_\Theta$ .

As shown in Fig.C.1, the accessible phonon momentum ranges over

$$|k_i - \tau| \leq q_{phonon} \leq \min(k_i + \tau, q_\Theta), \quad (C.3)$$

which can be converted into the difference between the neutron and phonon momenta:

$$k_i - \min(k_i + \tau, q_\Theta) \leq k_i - q_{phonon} \leq \begin{cases} \tau & \forall k_i \geq \tau \\ 2k_i - \tau & \forall k_i < \tau. \end{cases} \quad (C.4)$$

This is the momentum displacement between the two dispersion curves at a fixed energy,  $E = \hbar^2 k_i^2 / 2m_n = \omega(q_{phonon})$ . In the limit of small inverse lattice momentum  $\tau$  (Fig.C.2(a)), only sections of the phonon dispersion curve fall within the kinematic boundary, Eq.(C.4). However, higher multiples of  $\tau$  can further expand the allowed energy regime to a full energy coverage up to the Debye temperature. In the limit of large  $\tau$  or a small Debye momentum (Fig.C.2(c)), the inverse lattice momentum does not create significant additional phase space for coherent single phonon creation. For typical  $\tau$ 's with a value near the Debye momentum (Fig.C.2(b)), a large portion of the phonon modes can contribute to the coherent

scattering process, especially the high energy phonon modes. For coherent processes, the error in applying the incoherent approximation in calculating the total cross section can be estimated by performing an integration over this allowed range. The contribution of the missing low energy phonons is minimal because of their relatively small density of states.

In addition to momentum space, the density of states is also different in the coherent scattering. Assuming a continuum of phonon modes, the sum over momentum,  $\mathbf{q}$ , in the incoherent approximation Eq.(2.19) can be transformed into an integral over the energy space weighted by the density of states  $Z(\omega)$ ,

$$\sum_{j,\mathbf{q}} = 3N \int_0^{\omega_\Theta} d\omega Z(\omega), \quad (\text{C.5})$$

where  $j$  is the phonon polarization<sup>1</sup> and  $q$  is the phonon momentum. The density of states is a measure of the number of accessible phonon states within the energy  $\omega \sim \omega + d\omega$ . In the Debye model, it is

$$Z(\omega)d\omega = 3\omega^2 d\omega / \omega_\Theta^3. \quad (\text{C.6})$$

In the case of coherent scattering from polycrystals, given an incident neutron energy, there exists a ring in the phonon momentum space inside the Debye sphere satisfying the kinematic conditions as shown before. A rigorous analysis could express the radius of this ring in terms of  $\tau$ , the incident neutron energy and phonon dispersion relation ( $\omega = cq$  in the Debye model). For our purpose, an approximation which lets the radius equal half the phonon momentum is adequate. The sum in momentum is thus reduced to

$$\sum_{\mathbf{q}} = N \int_0^{\omega_\Theta} \omega / \omega_\Theta^2 d\omega, \quad (\text{C.7})$$

giving a one dimensional density of states, which reflects the fact that the momentum conservation exhausts one degree of freedom.

---

<sup>1</sup>A phonon has one longitudinal and two transverse polarizations. The longitudinal mode corresponds to the pressure wave (which creates density variations in the direction of propagation), and the transverse modes generate displacement variations perpendicular to the direction of propagation. A phonon represents a massive particle which propagates in a solid at the speed of sound.

In coherent scattering, the phonon itself has to carry away the neutron momentum if there is no inverse lattice momentum involved in assigning the phonon momentum (forward scattering), and thus, only longitudinally polarized phonons can contribute. This selects only one  $j$  in the sum  $\sum_j$ , and leaves  $|k \cdot \sigma^{long}|^2 = k^2$  in Eq.(2.18). In the case involving the inverse lattice momentum, transverse phonons can also contribute[33], however, the sum of the projections of the momentum transfer,  $k$ , onto the complete basis of the phonon polarization,  $\sigma^j$ , still gives the same value of  $|k \cdot \sigma|^2 = k^2$ .

To calculate the total cross section of UCN production, we need to perform a double integration of (2.18) and (2.19) over the initial neutron energy from  $E_{ucn}$  to  $\hbar\omega_\Theta$ , and over the final energy from 0 to  $E_{ucn}$ . In the coherent cross-section integral, the lower bound of the initial neutron energy is determined from (C.4), which assigns the phonon momentum  $q_{phonon} = \hbar^2 k_i^2 / 2mc$ , and becomes

$$\begin{aligned} k_i^{lower} - \tau &= 2k_i^{lower} - q_{phonon} \\ \Rightarrow k_i^{lower} &= \frac{-1 + \sqrt{1 + 2\hbar\tau/mc}}{\hbar/mc}. \end{aligned} \quad (C.8)$$

Taking into account these modifications, our estimated coherent cross-section is compared with its incoherent approximation,

$$\sigma_{coherent}/\sigma_{inc.approx.} = S_{coh}/S_{inc}. \quad (C.9)$$

Here we define

$$\begin{aligned} S_{coh} &= \int_{\omega_{lower}}^{\omega_\Theta} \sqrt{\omega} e^{-2W(\kappa)} \frac{1}{\omega_\Theta^2} \frac{1}{1 - e^{-\omega/T}} d\omega \\ S_{inc} &= \int_0^{\omega_\Theta} \sqrt{\omega} e^{-2W(\kappa)} \frac{3\omega}{\omega_\Theta^3} \frac{1}{1 - e^{-\omega/T}} d\omega. \end{aligned} \quad (C.10)$$

Where  $T$  is the temperature of the solid, and  $\omega_{lower}$  is defined as the lower neutron energy bound  $\hbar^2(k_i^{lower})^2/2m$ . In the low temperature limit, the Debye-Waller factor can also be represented as  $3\omega/(4M\omega_\Theta)$ , where  $M$  is the ratio of the mass of the scatterer to the mass of neutron. Taking  $M$  to be 4 for  $D_2$ , we can calculate the ratio of these two cross-sections as a function of the lower limit  $\omega_{lower}$ . The result is plotted in Fig.C.3.



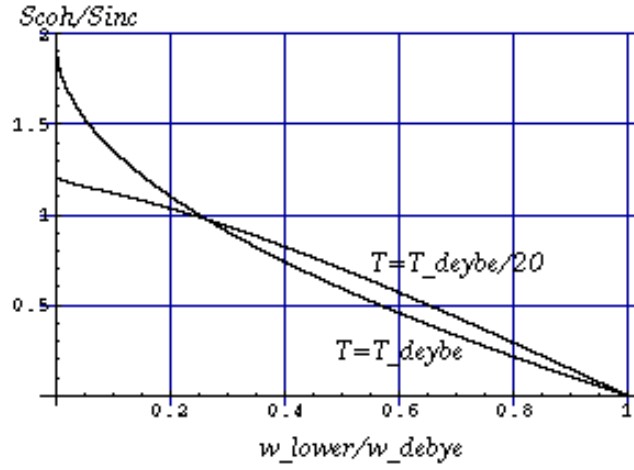


Figure C.3: Validity of incoherent approximation.

There are three fundamental parameters in this calculation: the intersection momentum  $k^*$  of the phonon and neutron dispersion curves, the Debye momentum  $q_\Theta$ , and the minimum lattice momentum  $\tau$ :

$$k^* = \frac{2mc}{\hbar}, \quad q_\Theta = \frac{\omega_\Theta}{\hbar c}, \quad \tau = \frac{2\pi}{d}. \quad (\text{C.11})$$

With these, we can re-express the x-axis variable of Fig.C.3,

$$x = \frac{\omega_{lower}}{w_\Theta} = (-1 + \sqrt{1 + 4\tau/k_i^*})^2 \frac{k^*}{4q_\Theta}, \quad (\text{C.12})$$

which is further simplified when  $\tau \ll k^*$ :

$$x \approx \frac{\tau^2}{k^* q_\Theta} = \frac{1}{f}. \quad (\text{C.13})$$

Thus,  $x$  is the inverse of the material parameter,  $f$ , defined by Placzek and Van Hove[30]. For a deuterium solid, the  $f$  number is 3.7. Thus, at solid temperature of roughly 6K (as shown by the  $T_\Theta/20 = 6K$  curve in Fig.C.3), the incoherent approximation gives a 15% smaller cross section than the coherent cross section we developed. This correction varies slowly with temperatures smaller than Debye temperature of solid deuterium. As pointed

out by Placzek and Van Hove, most of materials have a  $f$  number  $\sim 4$ , which happens to make the incoherent approximation satisfactory for the coherent scattering cross-section evaluations in the long neutron wavelength limit.

## Appendix D

# Polyethelene Scattering Kernel

In order to simulate the behavior of this prototype with the Monte Carlo methods using MCNP, it was necessary to develop a scattering kernel in ENDF-6 format[95] for incoherent neutron scattering from hydrogen in polyethylene at cryogenic temperatures, values of which are not yet available in the official neutron scattering database. This appendix describes the development of such a kernel in the form of  $S(\alpha, \beta)$  tables for polyethylene at 296 K, 77 K, and 4 K, temperatures relevant to the different cooling stages of the experiment.

### D.1 Density of States in Polyethylene

A scattering kernel for neutron scattering from the hydrogen in room temperature polyethylene was developed a number of years ago by Sprevak and Koppel[96] in the incoherent approximation<sup>1</sup> using the GASKET[97, 98] code. The frequency spectrum of polyethylene used for this scattering kernel calculation was derived from the work of Lin and Koenig[99], who calculated explicit force constants inside the molecular structure assuming polyethylene is an infinite chain of  $\text{CH}_2$  radicals (methylene). The force matrix is then simplified into a finite dimension by using the relative phases between adjacent methylene groups. This covers the intra-molecular excitations (i.e, optical modes), which can be classified into modes

---

<sup>1</sup>The incoherent approximation is particularly justified here since the coherent cross accounts for only 2.2% of the total scattering cross section( $\sigma_{tot} = 81.67$  barn) for H.

of symmetric and antisymmetric bond stretching, wagging, bending and rocking.[100] The direct excitation of bond stretching requires an energy of about 0.36 eV, and the other relative motions between bonds results in the structures between 0.08 and 0.19 eV seen in the energy spectrum shown in Fig. D.1. For sub-thermal energies the spectrum originates from the collective excitations of the solid lattice, which was approximated by the simple Debye spectrum[96] for the phonon contribution. A number of years later, Swaminathan and Tewari[101] developed a more accurate sub-thermal frequency distribution for polyethylene as part of their efforts to explore the use of cold polyethylene as a source of cold neutrons and to study the effect of the degree of crystallinity on neutron scattering. To do this they developed an anisotropic dispersive continuum model for the acoustic phonons in crystalline polyethylene.

Our UCN source involves spallation energy neutrons(several tens of MeV) being cooled to low energies (meV), so we require an accurate spectrum over the entire energy range. We have therefore combined the epithermal part of the the Sprevak and Koppel[96] spectrum with the low energy part of the Swaminathan and Tewari[101] spectrum for amorphous polyethylene. This combined spectrum was then run through the LEAPR[102] module of the NJOY[103] code package to obtain scattering kernels at various temperatures in ENDF-6 format. The density of states  $\rho(\omega)$  (derived from the energy spectrum),

$$\rho(\omega) = \sum_s \int \frac{d\vec{k}}{(2\pi)^3} \delta(\omega - \omega_s), \quad (\text{D.1})$$

used for generating the new polyethylene kernel is shown in Fig.D.1. The low energy (< 30 meV) component of the spectrum, due solely to the acoustic phonons, can be normalized to

$$\int_0^{T_\Theta} d\omega \rho(\omega) = N/V, \quad (\text{D.2})$$

to account for the correct number of degree of freedom(3 translational for each of the N scatterers( $\text{CH}_2$ ) in a volume V). Here  $T_\Theta$  is the Debye temperature of the polyethylene. An expanded plot showing the sub-thermal region of the spectrum is shown in Fig.D.2.

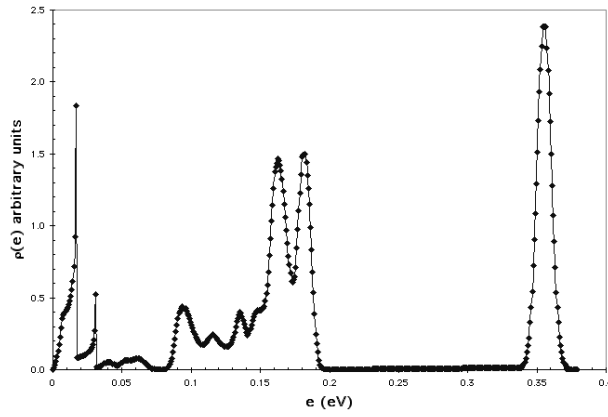


Figure D.1: Frequency distribution of polyethylene used for the scattering kernel.

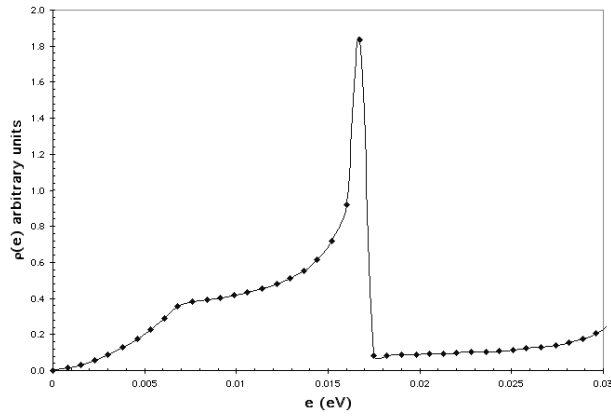


Figure D.2: Sub-thermal region of the frequency distribution for polyethylene.

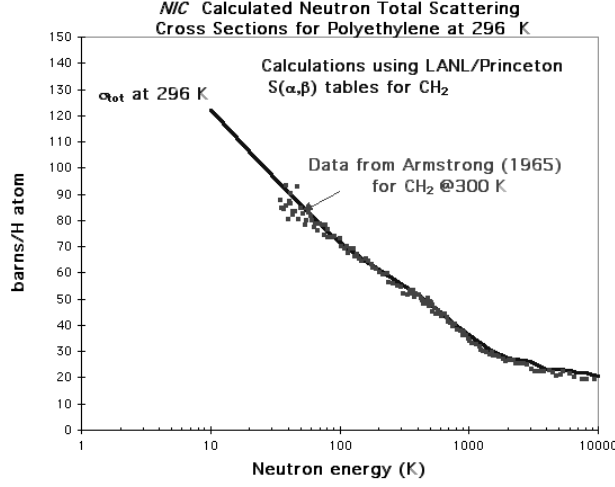


Figure D.3: Total neutron scattering cross section from room temperature polyethylene, calculated using the density of states presented in Fig.D.1

## D.2 Comparison of the Scattering Kernel with Experimental Data

A comparison of the calculated and measured[104] total scattering cross section for room temperature polyethylene is shown in Fig.D.3.

The experimental data have been adjusted by subtracting a  $1/v$  hydrogen absorption cross section (equal to 0.334 b/H atom at 0.0253 eV) and a constant 4.74 barns for scattering from the carbon nucleus. The agreement between theory and measurements is excellent.

The calculated inelastic component was obtained by integrating the double-differential cross sections obtained from the scattering kernel; i.e. the  $S(\alpha, \beta)$  tables, over energy and angle (Eq.(D.3)).

$$\frac{d^2 \sigma(T, E_i \rightarrow E_f, \theta)}{dE_f d\Omega} = \frac{\sigma_b}{4\pi T} \sqrt{\frac{E_f}{E_i}} e^{-\beta/2} S(\alpha, \beta), \quad (\text{D.3})$$

where  $\sigma_b$  is the bound scattering cross section. The unit-less momentum transfer  $\alpha$  and

energy transfer  $\beta$  are defined as

$$\begin{aligned}\alpha &\equiv \frac{E_i + E_f - 2\sqrt{E_i E_f} \cos \theta}{AT} \\ \beta &\equiv \frac{E_f - E_i}{T},\end{aligned}$$

where A is the atomic weight. The incoherent elastic component was obtained, using Eq.(D.4), from the Debye-Waller coefficient ( $\lambda$ ) calculated by LEAPR.

$$\sigma(E) = \sigma_b \frac{1 - e^{-4EW}}{4EW} \quad \text{where } W = \frac{\lambda}{AT}. \quad (\text{D.4})$$

A direct comparison of these double-differential cross sections with experimental data[105] at three different angles for an incident neutron energy of 232 meV ( $T_n = 2700$  K) is given in Fig.D.4. This data were taken from figures in the Sprevak and Koppel paper[96]. The structure built into the  $S(\alpha, \beta)$  tables from the  $\rho(e)$  matches well the structure observed in the neutron scattering. Note that in this situation, where  $T_n \gg T$  and the scattering is almost entirely inelastic (shown in the following section), there is little up-scattering and the angular distribution is strongly forward peaked. The peaks at low energy corresponds to the excitations of the energy states around 0.16 eV and 0.095 eV that are seen in Fig.D.1.

### D.3 Effect of Polyethylene Temperature on Cold Neutron Scattering

The effect of polyethylene temperature on incoherent elastic scattering is shown in Fig.D.5. It is clear that the elastic scattering of cold neutrons ( $T_n < 10$  K, or 1 meV) is independent of the temperature of the polyethylene and that as  $E \rightarrow 0$ ,  $\sigma(e) \rightarrow \sigma_b$ , as implied by Eq.( D.4). The high momentum transfer is suppressed as shown in the high energy part of the curve.

For incoherent inelastic scattering, however, Fig. D.6 shows that low energy neutron scattering is strongly dependent on polyethylene temperature while epithermal neutron ( $T_n > 1000$  K or 100 meV) scattering is temperature independent. Comparing the total scattering cross section in Fig. D.3 and the inelastic scattering cross section in Fig.D.6

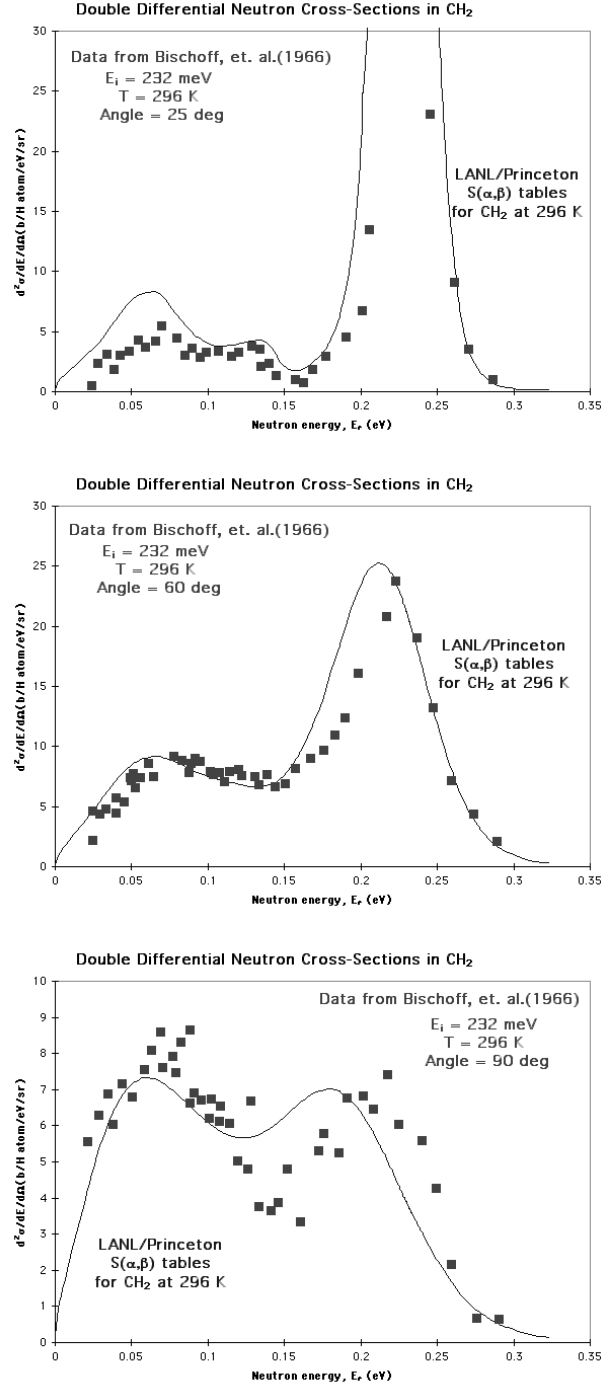


Figure D.4: Double differential cross sections for 232 meV incident neutron at 25, 60 and 90 degree scattering off of room temperature(296K) polyethylene.



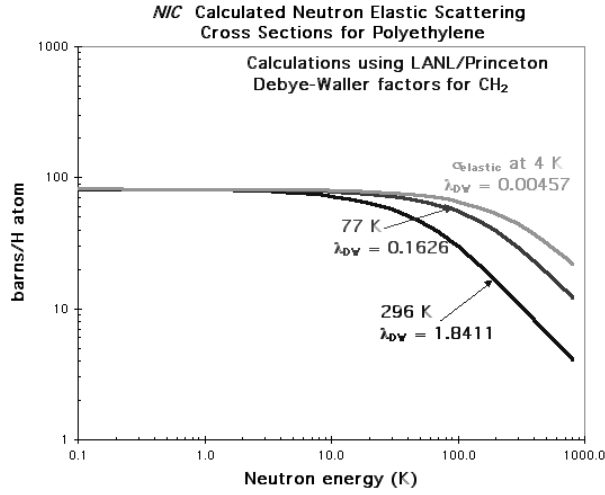


Figure D.5: Calculated neutron elastic scattering cross section for polyethylene temperatures of 296, 77 and 4 K. Also shown are the Debye-Waller coefficients at each temperature. (See Eq. (D.4).)

it can be seen that the inelastic contribution dominates and as neutron energies increase above several hundreds of meV, the scattering becomes almost entirely inelastic. In this region of strong down-scattering, the temperature independence is due to the fact that the inelastic cooling results from the excitation of internal states of the material which are intrinsic and whose availability depends very little on temperature. At lower energies, on the other hand, up-scattering begins to play a more important role and that depends on the availability of phonons with which the neutrons can collide and gain energy. The phonon density is suppressed by cooling the material producing the observed temperature dependence of the inelastic cross section. It should be noted that the usefulness of CH<sub>2</sub> at 4 K as a moderator is limited by absorption which has a larger cross section than inelastic scattering for neutron energies below about 70 K. Inelastic scattering is larger than absorption at all neutron energies for CH<sub>2</sub> temperatures above about 40 K. For the LANL UCN source, where substantial quantities of neutrons with energies below 40 K are desirable, the absorption losses are kept acceptable by using 4K CH<sub>2</sub> thicknesses in the

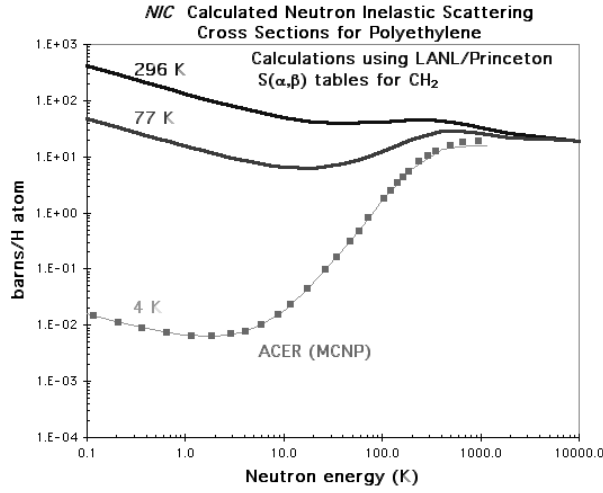


Figure D.6: The calculated neutron inelastic scattering cross section for polyethylene temperatures of 296, 77 and 4 K.

10-20 mm range.

The effect of polyethylene temperature on neutron scattering dynamics is illustrated in detail in Fig. D.7 which presents the differential scattering cross sections for a 10 meV (116 K) neutron from polyethylene at 296, 77 and 4 K. At 296 K, where  $T_n < T$ , most of the scattering is up-scattering and the angular distribution peaks at 90 degrees. As the temperature is lowered, more down-scattering occurs and the angular distribution becomes backward peaked. At 4 K, where  $T_n \gg T$  and the scattering is predominately elastic, there is almost no up-scattering and the down-scattering is backward peaked. This variation in up and down-scattering is to be expected for systems tending towards thermal equilibrium.

This new temperature dependent scattering kernel for polyethylene gives a good quantitative fit to the neutron scattering data available at room temperature and has a temperature dependence that is qualitatively consistent with thermodynamics.

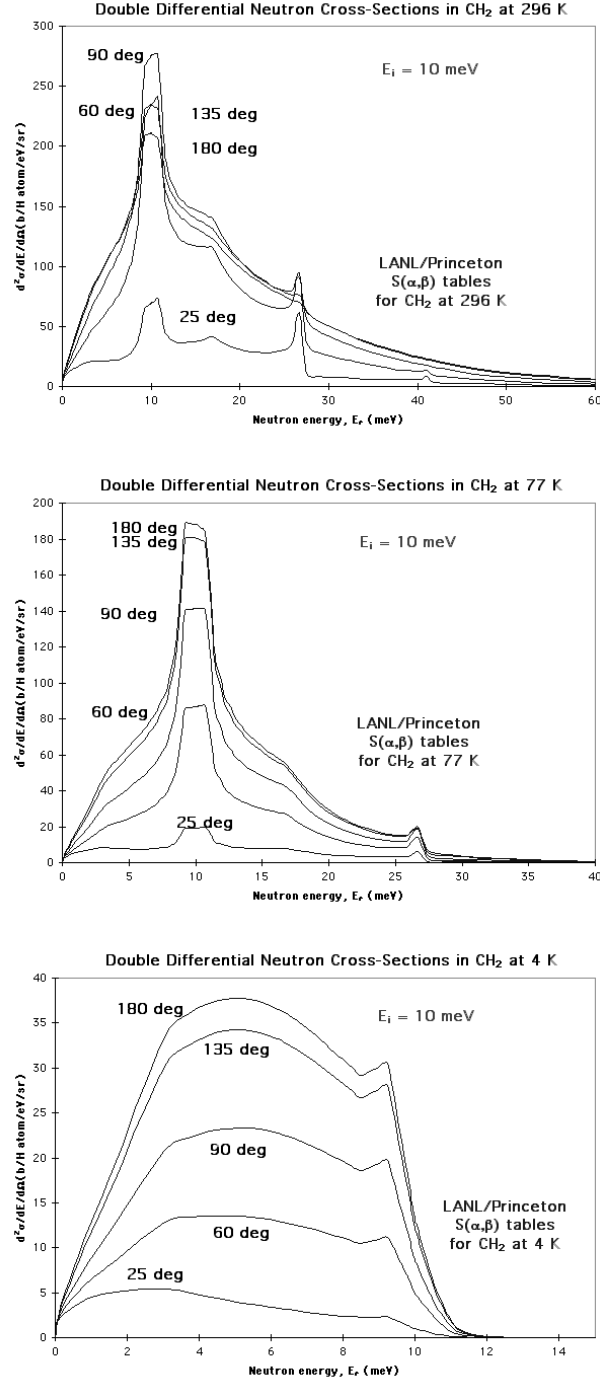


Figure D.7: The calculated differential cross section for scattering of a 10 meV (116 K) neutron from polyethylene at 296 K, 77K and 4K.

## Appendix E

# Proton Source – LANSCE Proton Accelerator

The UCN source uses protons from the LANSCE proton accelerator. It is a high intensity 1-MW proton linac, which can accelerate either  $H^+$  or  $H^-$ . The protons are accelerated to 800 MeV in this 800 m side-coupled R.F. cavities linac. It is capable of providing  $H^+$  beam with an average current of up to 1 mA with a repetition rate of 100 Hz and a peak current of 17 mA; and  $H^-$  beam with an average current up to 100  $\mu A$  with a repetition rate of 20 Hz and a peak current of 20 mA.

The structure of the proton pulses is illustrated in Fig.E.2. One requests protons from the linac by specifying three parameters: MPEG, MP width and the count-down number. MPEG is the duration of time (measured in micro-seconds) during which the linac sends protons into our experiment. It is a series of macro-pulses whose duration is adjusted by the “MP width” in the unit of nano-seconds, and these macro-pulses are separated by a time period of 180 ns times the “count-down number”. The linac runs at a default rate of 201.25 MHz, constantly producing micro-pulses spaced by 5 ns. Each micro-pulse has  $2 \times 10^8$  protons. A macro-pulse is a package of such micro-pulses, with the first two micro-pulses missing.

During our tests, we put the prototype source into Area C, the target II (blue room)

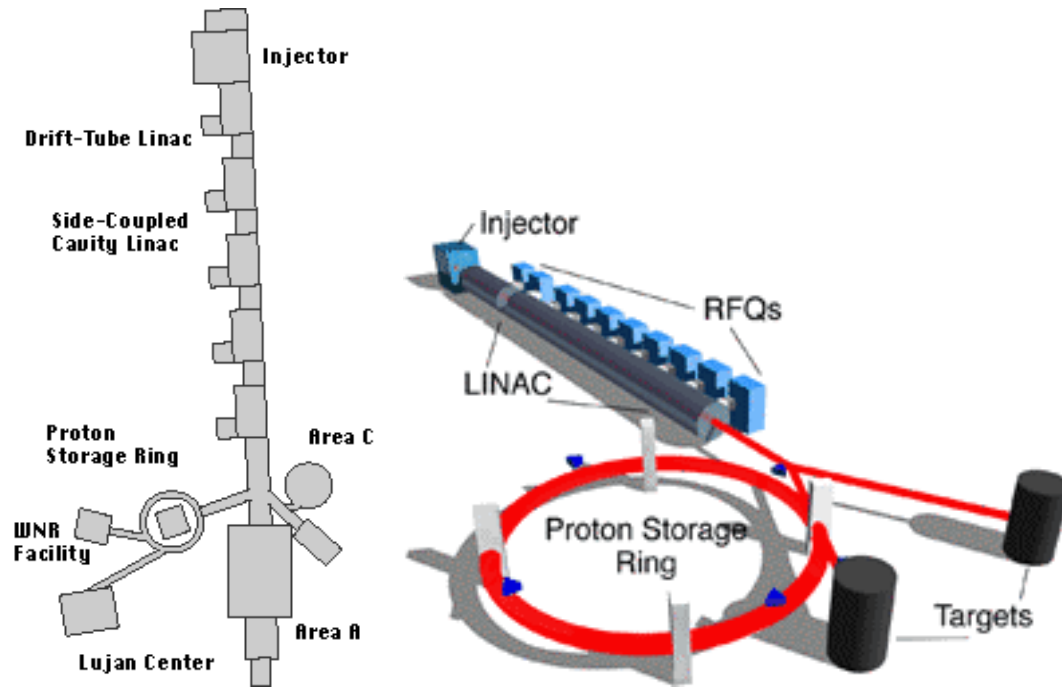


Figure E.1: LANSCE accelerator facility.

after the proton storage ring, and in line B (as shown in Fig.E.1).

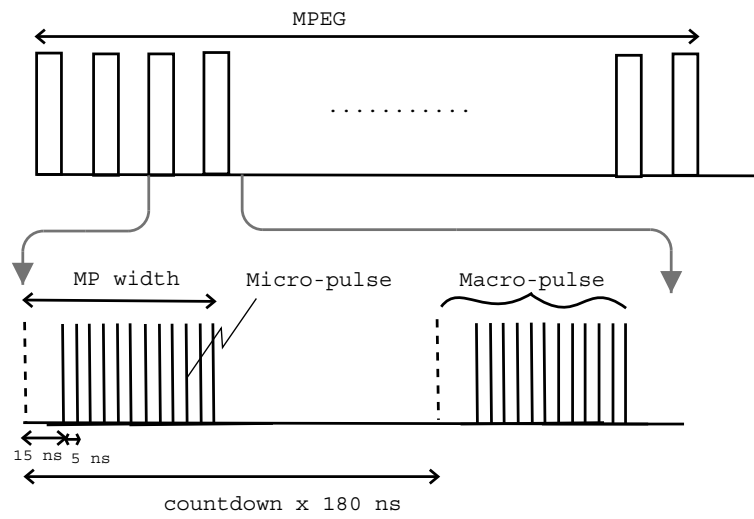


Figure E.2: Proton beam structure.

## Appendix F

# Bird Cage Field Profile

To understand the measured near field profile and further gain knowledge for the optimization of the bird cage resonator design, we developed a current model and solved the field strength by straightforward integration of the Biot-Savart law,

$$B = \frac{\mu_0}{4\pi} \mathbf{I} \int \frac{d\vec{l} \times \hat{r}}{r^2}. \quad (\text{F.1})$$

In the bird cage, sinusoidally distributed currents flow in the rungs and returning currents flow in the end rings. We approach this problem by decomposing this networked structure into a sum of single loops as shown in Fig.F.1. A pair of two rungs spaced  $180^\circ$  apart carry opposite current flow which then return through the end rings to form a closed current loop. The current flowing in the end rings from each rung is split in half. Consequently, a bird cage is a superposition of  $N/2$  loops of this kind which are oriented at  $\theta_n = n\frac{2\pi}{N}$ . One notices that the field generated by the loop with normal vector pointing towards  $\theta = 0$  carries the maximum current  $I_0$  and defines the principle transverse field direction of the resonator. Subsequent contributions from sets of loops at  $\theta$  and  $-\theta$  (with a smaller current  $I_0 \cos \theta$ ) also add up to this principle direction. Thus, we only need calculate the field generated by a single loop to solve this problem.

The edge of the resonator is defined as the origin of the coordinates. The symmetry axis of the cylindrical bird cage lies on the z-axis. The positive z direction lies outside of the resonator. One can analytically solve for the on-axis field strength using Eq.(F.1). The

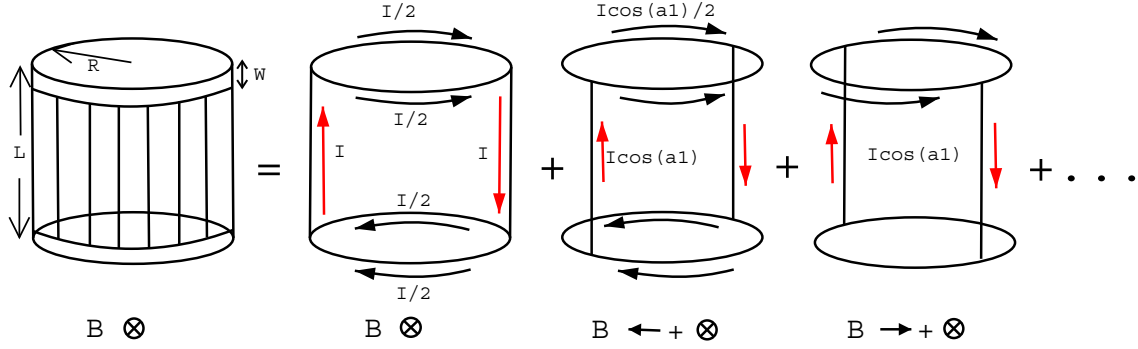


Figure F.1: A decomposition of the bird cage resonator into current loops. The direction of the magnetic field from each loop is also specified.

field generated by currents flowing in an end ring of a zero radius wire is solved with the choice of coordinates,

$$\begin{aligned}
 \hat{r} &= \left( -R \cos \phi, -R \sin \phi, z \right) \frac{1}{\sqrt{R^2 + z^2}} \\
 d\vec{l} &= (-\sin \phi R d\phi, \cos \phi R d\phi, 0) \\
 d\vec{l} \times \hat{r} &= \left[ \frac{zR \cos \phi d\phi}{\sqrt{R^2 + z^2}} \right] \hat{i} + \left[ \frac{zR \sin \phi d\phi}{\sqrt{R^2 + z^2}} \right] \hat{j} + \frac{R^2 d\phi}{\sqrt{R^2 + z^2}} \hat{k},
 \end{aligned}$$

and knowledge of the current flow,

$$\mathbf{I} = \begin{cases} I/2 & \phi : 0 \sim \pi \\ -I/2 & \phi : \pi \sim 2\pi. \end{cases} \quad (\text{F.2})$$

The integration gives a field which points in the y direction.

$$\begin{aligned}
 B_x^{ring} &= \frac{\mu_0 I}{4\pi} \frac{zR}{(R^2 + z^2)^{3/2}} \left[ \int_0^\pi \cos \phi d\phi - \int_\pi^{2\pi} \cos \phi d\phi \right] = 0 \\
 B_y^{ring} &= \frac{\mu_0 I}{4\pi} \frac{zR}{(R^2 + z^2)^{3/2}} \left[ \int_0^\pi \sin \phi d\phi - \int_\pi^{2\pi} \sin \phi d\phi \right] = \frac{\mu_0 I}{4\pi} \frac{zR \times 4}{(R^2 + z^2)^{3/2}} \quad (\text{F.3}) \\
 B_z^{ring} &= \frac{\mu_0 I}{4\pi} \frac{R^2}{(R^2 + z^2)^{3/2}} \left[ \int_0^\pi d\phi - \int_\pi^{2\pi} d\phi \right] = 0
 \end{aligned}$$



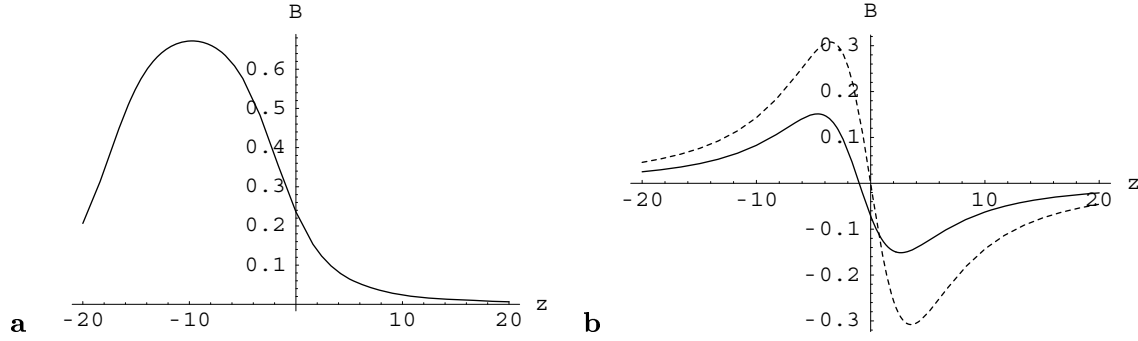


Figure F.2: The field generated by the rungs (subplot **a**) and the end rings (subplot **b**). In subplot **b** is plotted field profiles of end rings of zero radius wire (dashed curve) and flat conducting tape of width 2 cm (solid curve).

The field generated by a current flowing in a single rung can be readily solved as:

$$\begin{aligned}
 \hat{r} &= (-R, 0, -z) \frac{1}{\sqrt{R^2 + z^2}} \\
 d\vec{l} &= (0, 0, dz) \\
 d\vec{l} \times \hat{r} &= \frac{-Rdz}{\sqrt{R^2 + z^2}} \hat{j} \\
 B^{rung} &= \frac{\mu_0}{4\pi} I \int \frac{-Rdz}{(R^2 + z^2)^{3/2}} \hat{j} \\
 (\text{set } z &= R \cot \theta) \\
 &= \frac{\mu_0}{4\pi} I \frac{1}{R} \int_{\theta_1}^{\theta_2} -\sin \theta d\theta = \frac{\mu_0}{4\pi} I \frac{1}{R} \cos \theta \Big|_{\theta_1}^{\theta_2} \\
 &= \frac{\mu_0}{4\pi} I \frac{1}{R} \left[ \frac{z}{\sqrt{R^2 + z^2}} - \frac{L + z}{\sqrt{R^2 + (L + z)^2}} \right] \hat{j} \tag{F.4}
 \end{aligned}$$

and also points in the y direction.

As plotted in Fig.F.2, a current in a rung generates a Gaussian shaped profile, centered in the middle of the resonator (shown in subplot **a**); currents in an end ring produce a field shown in subplot **b** whose direction reverses when it passes through the ring. Outside of the bird cage, this out-of-phase field cancels the contribution from the central field generated by currents flowing in the rungs, reproducing the observed peak in the field profile. Moreover, we need to incorporate the finite dimensions of the current elements to make a satisfactory fit to the measured profile. The end rings are made of flat conducting tape with a width

$W$ , which is relatively large ( $\sim 40\%$ ) compared with the radius of the resonator. The approximation of a zero radius wire is inadequate in this case. We thus calculate the transverse field generated by the end ring of a flat conductor:

$$\begin{aligned}
B^{ring} &= \frac{\mu_0}{4\pi} 4\mathbf{I} \frac{zR}{(R^2 + z^2)^{3/2}} \hat{j} \\
(\mathbf{I} &= I \frac{dz}{W}) \\
&= \frac{\mu_0}{4\pi} 4I \int_{z_0}^{z_0+W} \frac{zR}{(R^2 + z^2)^{3/2}} \frac{dz}{W} \hat{j} \\
&= \frac{\mu_0}{4\pi} 2I \frac{1}{W} \left[ \frac{-1}{\sqrt{1 + (\frac{z+W}{R})^2}} + \frac{1}{\sqrt{1 + (\frac{z}{R})^2}} \right] \hat{j}.
\end{aligned} \tag{F.5}$$

This reduces the canceling effect and results in a smaller peak (as shown in the subplot **b** in Fig.F.2).

A sum of fields generated by these segments gives the field  $B_0$  from the contribution of a single closed current loop:

$$B_0 = B^{ring}(z) + B^{ring}(z + L) + B^{rung}(z) \times 2. \tag{F.6}$$

The total transverse field is obtained by summing the field of the  $N/2$  loops, taking into account the sinusoidal current distribution and the projection of the field vectors,

$$\begin{aligned}
B^{tot} &= \sum_{n=1}^{N/2} \frac{I_0 \cos \theta_n}{I_0} B_0 \times [\sin \theta_n \hat{i} + \cos \theta_n \hat{j}] \\
&= B_0 \sum_{n=1}^{N/2} \cos^2 \left( n \frac{2\pi}{N} \right) \hat{j}.
\end{aligned} \tag{F.7}$$

With the above analytical model, we can carry out a study of the parameter dependence: First, the far field behavior from contributions in rungs and end rings using Eq.(F.4) and Eq.(F.5) is:

$$\begin{aligned}
\lim_{z \rightarrow \infty} B^{rung} &= \frac{3L}{R} \frac{1}{z} - \frac{L^2}{R} \frac{1}{z^2} + O\left(\frac{1}{z^3}\right) \\
\lim_{z \rightarrow \infty} B^{ring} &= \frac{R}{z^2} + O\left(\frac{1}{z^3}\right).
\end{aligned} \tag{F.8}$$

We thus conclude that the overall RF field falls off as  $1/z$ , which is dominated by the field generated by currents flowing in rungs. We then vary the length and the radius of the

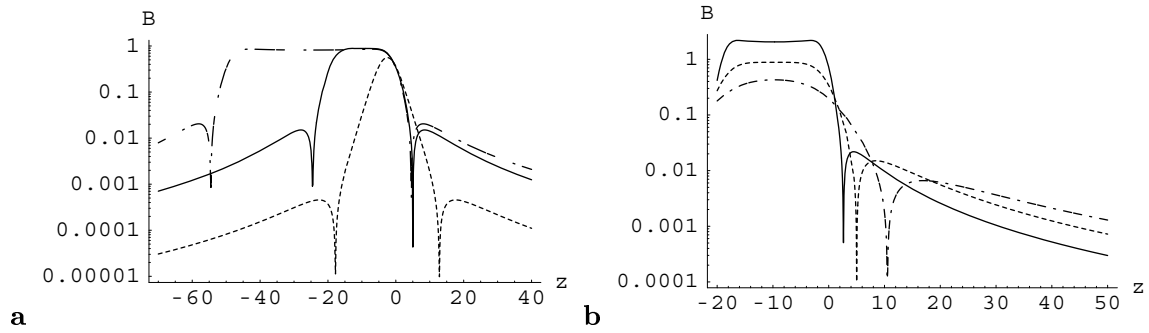


Figure F.3: Comparison of the field profiles generated by two geometry of the end rings. The default dimension of the resonator is  $L = 19.5$  cm,  $R = 5$  cm and  $W = 2$  cm. **a.** The length of the resonator is 5 cm, 19.5 cm and 50 cm for the three curves plotted. **b.** The radius of the resonator is 2 cm, 5 cm and 10 cm for the solid, dashed and dash-dotted curve, respectively.

bird cage as shown in subplots in Fig.F.3. It seems that the length of the rungs does not significantly alter the center field strength, but it scales up the residual field outside the resonator, until the dimension of the length becomes comparable of the radius, and then the canceling effect from current flowing in the end rings dominates, resulting in a rapid fall-off in the field strength with the trade-off of a narrow full power resonance region. The position of the valley before the peak is correlated with the radius of the end ring and the field strength ratio of the center field to the peak height reduces as the radius increases. Nevertheless, the near field is decaying faster for smaller radius resonators as indicated by Eq.(F.8). These observations favor a small bird cage resonator (small  $L/R$  and small  $R$ ) for a fast decaying field profile.

The effect of the metal shielding can be calculated using the trick of image currents flowing on a surface mirrored by the grounding shielding metal. With a cylindrical shield geometry, to the first order, we consider only the nearest image currents and assume that the induced opposite current flowing in the shield has the same magnitude as the current flowing in the bird cage resonator. This results in a virtual bird cage with radius  $d + (d - R) = 2d - R$ ,

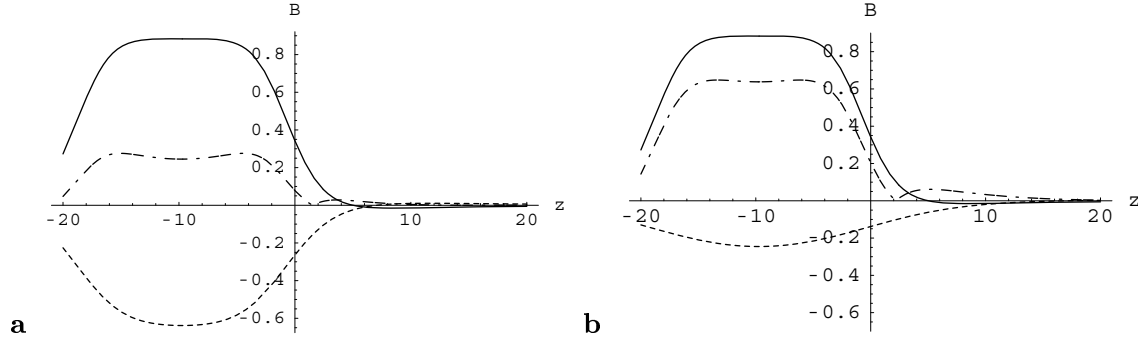


Figure F.4: Field under the shielding. The metal shield has a radius of 7 cm and 15 cm in subplot **a** and **b**, respectively. The bird cage resonator has a radius of 5 cm, length of 19.5 cm, and 2 cm wide end rings.

where  $d$  and  $R$  are the radius of the shielding and the bird cage resonator, respectively. We then superimpose this shield contribution onto the resonator field in free space to estimate the total field profile. Fig.F.4 demonstrates the shielding effect of metal cylinders with different radii. A nearby shielding cylinder (subplot **a**) largely reduces the center field strength, while a distant shielding cylinder (subplot **b**) generates a larger residual field outside of the resonator but has a higher center field to residual field ratio.

Fig. 6.6 presents the measured effect of the field profile under the presence of a near shield. It resembles the calculation illustrated in subplot **a** in Fig. F.4 and follows predictions discussed above.

# Bibliography

- [1] J. Chadwick, M. Goldhaber, *Nature* **134**, 237 (1934).
- [2] The European Physical Journal C **15**, No. 1-4, 54 (2000).
- [3] K.S. Krane, *Introductory Nuclear Physics* (John Wiley & Sons, New York 1987), chapter 9.
- [4] B.R. Holstein, *Weak Interactions in Nuclei* (Princeton University Press, Princeton, NJ, 1989)
- [5] J.D. Jackson, S.B. Treiman and H.W. Wyld, Jr., *Phy. Rev.* **106**, No. 3, 517 (1957).
- [6] P. Herczeg, *Conference Proceedings in Precession Tests of the Standard Electroweak Model* (World Scientific, Singapore, 1995) p.786.
- [7] M. Kobayashi, T. Maskawa, *Proc. Theor. Phys.* **49**, 652 (1973).
- [8] R.N. Mohapatra and R.E. Marshak, *Phys. Lett.* **91B**, 222 (1980).
- [9] Yu. Abov, F. Djeparov, J. Okun, *JETP Lett* **39**, 493 (1984).
- [10] Y. Kamyshev, *Surv. High Energy Phys.* **13**, No. 1-3, 2 (1998).
- [11] S. Marsh, K.W. McVoy, *Phys. Rev. D* **28**, 2793 (1983).
- [12] Ye.S. Golubeva, A.S. Iljinov and L.A. Kondratyuk, *Yadernaya Fizika* (Phys. At. Nucl. (translation)) **60**, No. 12, 2188 (1997).
- [13] C.B. Dover, A. Gal, and J.M. Richard, *Phys. Rev. C* **31**, No. 4, 1423 (1985).

- [14] M. Balso-Ceolin *et al.*, Z. Phys. C **63**, 409 (1994).
- [15] F. Glück, I. Joó and J. Lasts, Nuc. Phys. A **593i** 125 (1995).
- [16] I.B. Khriplovich, A.R. Zhitnitsky, Phys. Lett B **109**, 490 (1982).
- [17] A.D. Sakharov, JETP Lett. **5**, 24 (1967).
- [18] I.I. Bigi, N.G. Uraltsev, Nucl. Phys. B **353**, 321 (1991).
- [19] I.B. Khriplovich and S.K. Lamoreaux, *CP Violation Without Strangeness: Electrical Dipole Moments of Particles, Atoms and Molecules* (Springer, New York, 1997).
- [20] N.F. Ramsey, *In Discovery of Weak Neutral Currents: The Weak Interaction Before and After*, eds. A.K. Mann, D.B. Cline (AIP, New York 1993); N.F. Ramsey, Phys. Rev. **109**, 222 (1958).
- [21] Y.N. Pokotilovski, Nucl. Instr. and Meth. A **356**, 412 (1995).
- [22] F.L. Shapiro, *Pro. Int. Conf. on Nuclear Structure Study with Neutrons*(Budapest) ed. J. Ero and J. Szucs (Plenum, New York, 1972) p.259.
- [23] R. Golub, Phy. Lett. **38A**, No. 3, 117 (1972).
- [24] R. Golub and J.M. Pendlebury, Phys. Lett. **A53**, 133 (1975).
- [25] R. Golub and K. Boning, Z. Phys. **B51**, 95 (1983).
- [26] Z.-C. Yu, S.S. Malik and R. Golub, Z. Phys. **B62**, 137 (1986).
- [27] V.F. Sears, *Method of experimental physics – solid state nuclear methods*, **21**, 5.
- [28] P.R. Huffman *et al.*, Nature **403**, 62 (2000).
- [29] C. Morris *et al.*, submitted to PRL, september, 2001.
- [30] G. Placzek and L. Van Hove, Nuovo cimento **1**, No. 1, 233 (1955).
- [31] J.A. Young and J. Koppel, Phy. Rev. **135**, No. 3A, A603 (1964)

- [32] Jan Van Kranendonk, *Solid Hydrogen*, 1982.
- [33] S.W. Lovesey, *Theory of neutron scattering from condensed matter* (Clarendon press, Oxford, Oxford, 1984), Vol I.
- [34] A.P. Serebrov *et al.*, J. Phys. Soc. Jpn. **65**, Suppl. **A**, 259 (1996).
- [35] C.-Y. Liu, A.R. Young and S.K. Lamoreaux, Phys. Rev. B **62**, R3581 (2000).
- [36] Silvera, Rev. Mod. Phys. **52**, No. 2, Part I, 393 (1980).
- [37] D.D. Eley, *Advances in catalysis and related subjects* (Academic Press Inc., New York, 1948), vol I, p174.
- [38] P.W. Selwood, *Advances in catalysis and related subjects* (Academic Press Inc., New York, 1951), vol III, p27.
- [39] H.B. Weiser, *Inorganic colloid chemistry* (Jhon Wiley & sons, London, 1935), Vol II, *The hydrous oxides and hydroxides*.
- [40] A.N. Bazhenov, V.I. Medvedev, and A.N. Pirozhkov, Priboiy i Tekhnika Eksperimenta, No. 4, 63 (1992).
- [41] R.A. Buyanov, Kinetika i Kataliz **1**, No. 2, 306 (1960).
- [42] D.H. Weitzel and O.E. Park, Rev. Sci. Inst. **26**, 57 (1955).
- [43] D.H. Weitzel, W.V. Loebenstein and J.W. Draper, J. Res. Nat. Bur. Stand. **60** (3), 221 (1958).
- [44] G. Baym, *Lectures on quantum mechanics* (The Benjamin/Cummings publishing company, Massachusetts, 1969), p289.
- [45] D.K. Walter, W.M. Griffith and W. Happer, PRL **86**, No 15, 3264 (2001).
- [46] A. Compaan, A. Wagoner and A. Aydinli, Am. J. Phys. **62** (7), 639 (1994).

- [47] N.V. Tsederberg, *Thermal conductivity of gases and liquids* (The M.I.T. Press, Cambridge, Massachusetts, 1965).
- [48] M. Devoret, N.S. Sullivan, D. Esteve, and P. Deschamps, Rev. Sci. Instrum. **51** (9), 1220 (1980).
- [49] A. Farkas, *Orthohydrogen, Parahydrogen and heavy hydrogen* (Cambridge University, Cambridge, England, 1935).
- [50] A.T. Stewart, *et al.*, J. Sci. Instrum. **32**, 26 (1955).
- [51] E.R. Grilly, Rev. Sci. Instrum. **24**, 72 (1953).
- [52] G.W. Collins, *et al.*, Phys. Rev. B **53**, No. 1, 102 (1996).
- [53] J.W. Haarman, Physica **52** 605 (1971).
- [54] C.A. Nieto de Castro and W.A. Wakeham, *Thermal conductivity 15* (Plenum Press, New York, 1981), 235.
- [55] A. Steyerl, Phys. Lett. **B29**, 23 (1969).
- [56] A. Steyerl, Nucl. Instr. Meth. **125**, 461 (1975).
- [57] <http://lansce.lanl.gov/overview/neutrons.htm>
- [58] S.K. Lamoreaux, private communications.
- [59] <http://www-xdiv.lanl.gov/XCI/PROJECTS/MCNP/>
- [60] <http://www-xdiv.lanl.gov/XCI/PROJECTS/LCS/lahtet-doc.html>
- [61] R. Hill, private communications.
- [62] C. Morris, private communications.
- [63] K. Klaus, private communications.
- [64] A. Steyerl *et al.*, Phys. Lett. **A116**, 347 (1986).



- [65] K. Kirch *et al.*, CAARI Conference proceedings (2000).
- [66] M. Daum, the third International UCN workshop conference proceedings (2001).
- [67] S. Paul, the third International UCN workshop conference proceedings (2001).
- [68] I. N. Krupskii, A. I. Prokhvatilov, Yu. A. Freiman and A. I. Frenburg, Fiz. Nizk. Temp. **5**, 271 (1979) [Sov. J. Low Temp. Phys. **5**, 130 (1979)].
- [69] A. Jezowski, P. Stachowiak, V.V. Sumarokov, and J. Mucha, Phys. Rev. Lett. **71**, No.1, 97 (1993).
- [70] P.W. Stephens and C.F. Majkrzak, Phys. Rev. B **33**, 1 (1986).
- [71] The scattering law  $S(\kappa, \omega)$  defined here is slightly different from that defined in ref [70] which only retains the dynamical structure factor.
- [72] W. H. Kleiner, Phy. Rev. **97**, No. 2, 411 (1955).
- [73] E.J. Wachtel and R.G. Wheeler, J. Appl. Phys. **42**, No 4, 1581 (1971).
- [74] N.M. Temme, *Special functions – An introduction to the classical functions of mathematical physics* (John Wiley & Sons, New York, 1996), 399.
- [75] A theoretical calculation and an analysis of lifetime measurements on UCN in SD<sub>2</sub> bottle from Los Alamos collaboration, to be published.
- [76] R.E. Hill *et al.*, Nucl. Instr. Meth. **440**, No. 3, 674 (2000).
- [77] V.F. Sears, *Neutron optics: an introduction to the theory of neutron optical phenomena and their applications* (Oxford University Press, New York, 1989).
- [78] Baragiola, *et al.*, Nucl. Instr. Meth. **B**, 233 (1999).
- [79] Giaque and Johnston, J. Am. Chem. Soc. **51**, 2300 (1929).
- [80] Fagerstroem and Hallet, JLTP **1**, 3 (1969).

- [81] J.D. Bowman, S.I. Penttilä and W.B. Tipples, Nucl. Instr. Meth. A **369**, 195 (1996).
- [82] F. Bloch, Phys. Rev. **70**, 460 (1946).
- [83] A.I. Egorov *et al.*, Yadernaya Fizika **19**, 300 (1974).
- [84] A. Abragam, *The Principles of Nuclear Magnetism* (Clarendon, Oxford, 1961).
- [85] J. Tropp, J. Magn. Reson. **82**, 51 (1989); J. Magn. Reson. **126**, 9 (1997).
- [86] L. Brillouin, *Wave propagation in periodic structures* (MacGraw Hill Book, New York, 1946).
- [87] H. Weinfurter and G. Badurek, Nucl. Instr. Meth. A **275**, 233 (1989).
- [88] F.W. Grover, *Inductance calculations, working formulas and tables*, (Instrument society of America, New York, 1973).
- [89] C.E. Hayes, *et al.*, J. Mag. Res. **63**, 622 (1985).
- [90] A. Serebrov *et al.*, Nucl. Instr. Meth. A **440**, 717 (2000).
- [91] <http://quasar.phys.vt.edu/makela/ucn.html>
- [92] R. Golub, D.J. Richardson, and S.K. Lamoreaux, *Ultra-cold neutrons* (Adam Hilger, Bistol, 1991), 66.
- [93] These scattering lengths reproduce the calculation presented by R.E. MacFarlane, Los Alamos National Laboratory Report No. LA-12639-Ms (ENDF 356), 1994.
- [94] I.F. Silvera, Rev. Mod. Phys. **52**, No. 2, Part I, 393-452 (1980).
- [95] P.Rose and C.L. Dunford, Technical Report No. BNL-NCS-44945, Brookhaven National Laboratory (July, 1990).
- [96] D. Sprevak and J.U. Koppel, Nucleonik **12**, 87 (1969).

- [97] J. Koppel, J.R. Triplett and Y. Naliboff, Technical Report No. GA-7417 (Rev.), Gulf General Atomic, Inc. (March 10, 1967).
- [98] J. Koppel and D. Houston, Technical Report No. GA-8774 (Revised and reissued as ENDF-269 by the National Nuclear Data Center at the Brookhaven National Laboratory in July, 1978), Gulf General Atomic, Inc., (December 31, 1969).
- [99] T. Lin and J. Koenig, J. Mol. Spectrosc. **9**, 228ff (1962).
- [100] M. Tasumi, T. Shimanouchi and T. Miyazawa, J. Mol. Spec. **9**, 261 (1962).
- [101] K. Swaminathan and S. P. Tewari, Nucl. Sci. Eng. **91**, 95 (1985).
- [102] R. MacFarlane, Technical Report No. LA-12639-MS (ENDF-356), Los Alamos National Laboratory, Los Alamos, NM (March, 1994).
- [103] R. MacFarlane and D.W. Muir, Technical Report No. PSR-355, Radiation Safety Information Computation Center - Oak Ridge National Laboratory (July, 1990); <http://t2.lanl.gov/codes/njoy99/index.html>.
- [104] S.B. Armstrong, Nucl. Sci. Eng. **23**, 192 (1965).
- [105] F. Bischoff, W.A. Bryant, L.J. Esch, C. Lajeunesse, W.E. Moore, S.S. Pan, S.N. Purohit and M.L. Yeater, R.P.I. Annual Technical Report, July 1966 through September 1996, Linear Accelerator Project, Technical report, Rensselaer Polytechnic Institute.

# List of Figures

2.1	Dispersion curves of free neutrons (black curve) and the superfluid $^4\text{He}$ (red curve). The intersecting point (Q,E) of these two curves sets the condition for inelastic one phonon neutron scattering for UCN production. . . . .	14
2.2	The Maxwell-Boltzmann energy distribution of 30K neutrons. This depicts the fact that only a narrow window in the energy spectrum is open for UCN production. The inset illustrates the energy transitions in the two-state model which describes the coherent superthermal UCN source, i.e., superfluid $^4\text{He}$ . . . . .	15
2.3	Time evolution of the states in the modified three-state model. The inset illustrates the transitions between the initial cold neutron state, UCN state and the thermal-equilibrium state. . . . .	18
2.4	(a) The directionally dependent dispersion curve, illustrated on a normal plane. (b) The intersection of the free neutron dispersion curve (black curve) with the phonon dispersion curve at three scattering angles. . . . .	21
2.5	A schematic of energy and momentum conservations for phonon creation. .	23
2.6	The UCN upscattering cross-section vs. the temperature of solid $\text{D}_2$ . The one-phonon annihilation cross-section in an ortho- $\text{D}_2$ solid(solid curve) and in a para- $\text{D}_2$ solid(dashed curve) are plotted. The dashed-dagger line is the temperature independent UCN upscattering cross-section involving $J=1 \rightarrow 0$ relaxation not coupled to phonons in a para- $\text{D}_2$ solid. . . . .	25
3.1	The rotational energy spectrum of ortho- and para- $\text{D}_2$ . . . . .	31

3.2	A schematic of the para/ortho-D <sub>2</sub> converter. . . . .	35
3.3	A schematic of the gas handling system used for the S-D <sub>2</sub> UCN source preparation. . . . .	37
3.4	The first Raman spectrum of normal (non-converted) H <sub>2</sub> and D <sub>2</sub> with approximately 600 Torr partial pressure each. The power from the argon ion laser is 15 W. The primary laser wavelength is 515 nm. The dashed and solid peaks are spectrum of H <sub>2</sub> and D <sub>2</sub> , respectively. . . . .	40
3.5	A schematic of the D <sub>2</sub> Raman spectroscopy setup. . . . .	41
3.6	Rotational Raman spectrum with and without a Raman filter. . . . .	42
3.7	The Raman spectrum of converted and unconverted D <sub>2</sub> . Slit widths are set to 400 $\mu$ m. The ‘+’ curve is the reference normal D <sub>2</sub> . The ‘ $\times$ ’ curve is a converted D <sub>2</sub> with $(1.54\% \pm 0.21\%)$ of para-D <sub>2</sub> , and $(1.27\% \pm 0.12\%)$ of HD. The square-dotted curve is purified converted D <sub>2</sub> with $(1.42\% \pm 0.20\%)$ of para-D <sub>2</sub> , and a reduced HD contamination of $(0.26\% \pm 0.06\%)$ . . . . .	43
3.8	Relaxation in the Raman cell: The para-D <sub>2</sub> concentration grows from 4.2% (‘+’ set), converted at 23.6K, to 7.3% (dotted set) over a 5 day period. . . . .	45
3.9	Raman spectrum taken with the double grating spectrometer . . . . .	46
3.10	The thermal conductivity cell. . . . .	47
3.11	The performance of the hot wire cell. <b>a.</b> The ‘+’ data set is taken with a unpurified D <sub>2</sub> sample (with a high HD concentration of $2.05\% \pm 0.16\%$ ) The knowledge of the para-D <sub>2</sub> concentration obtained from the Raman spectroscopy. The “ $\times$ ” set of data is taken with gas mixtures with known volume ratio of the converted D <sub>2</sub> at 17 K and the normal D <sub>2</sub> . HD contamination is approximately 0.3%. <b>b.</b> Scatter of data (“ $\times$ ” data set in <b>a</b> ) in the voltage measurements. . . . .	53

3.12	The stability in time of the converter and the measuring cell. Both sets of data are $D_2$ from a converter operated at 17 K. From the Raman spectroscopy measurement, the ‘+’ data set has an average para- $D_2$ concentration of $1.54\% \pm 0.21\%$ and the HD concentration of $1.2\% \pm 0.55\%$ , while the ‘×’ data set is taken with unpurified $D_2$ of an averaged para- $D_2$ concentration of $1.42\% \pm 0.2\%$ and an HD impurity of $0.26\% \pm 0.06\%$ . . . . .	54
3.13	The performance of converter over a time course of 9 months during the on and off operations in the year 2000. . . . .	54
3.14	(a) The para- $D_2$ fraction of $D_2$ (measured with Raman spectroscopy) converted at different temperatures. (b) The hot wire voltage measurement of converted $D_2$ from converter operated at temperature from 17 K to 25 K. The arrows indicate the time order of measurements. . . . .	55
3.15	Vapor pressure of $D_2$ in an environment with catalyst, hydrous ferric oxide, compared with vapor pressure in the free space. . . . .	56
4.1	A picture and a schematic of the prototype UCN source. . . . .	58
4.2	The cold neutron time-of-flight spectra compared with the MCNP simulation. The green curve is measured with 400 c.c. cryogenic solid deuterium, and the red curve is measured without the deuterium. The effect of the solid $D_2$ on the cold neutron spectrum is indistinguishable within our statistical limits[76].	65
4.3	A schematic of our UCN run setup. . . . .	66
4.4	Time of flight spectrum. . . . .	68
4.5	Electronic efficiency. Here shows the linearity of the detector response to the discriminator threshold. . . . .	69
4.6	UCN production vs. S- $D_2$ volume. The experimental data (solid dots) is compared with the results of a Monte-Carlo simulation (hollow dots). . . .	70
4.7	Decay curves of UCN in contact with solid deuterium with different para- $D_2$ concentrations. . . . .	73

4.8	A measured UCN time-of-flight spectrum and Monte-Carlo simulated spectrum with different wall specularities. . . . .	74
4.9	$\chi^2$ minimization of the fit. . . . .	75
4.10	UCN lifetime dependence on the solid temperature and the para-D <sub>2</sub> fraction.[29]	77
4.11	A TOF spectrum for the UCN bottle run. . . . .	78
4.12	Stored UCN density in the S.S. bottle. The dependence of UCN production on the proton current. The volume of S-D <sub>2</sub> is approximately 200 c.c. and the para-D <sub>2</sub> fraction in the source is approximately 6%, with a 0.2% HD contamination. . . . .	79
5.1	Neutron scattering law in a 5K solid $\alpha$ -O <sub>2</sub> : A contour plot of $S(\kappa, \omega)$ is presented here. The upper half plane( $\omega > 0$ ) describes the case of downscattering, and the $\omega < 0$ describes the case of upscattering. The importance of the contribution from different $(\kappa, \omega)$ is illustrated by the density of the contours. The area of integration is bounded by the dotted lines for incident neutrons with an initial energy $E_i=0.03\text{eV}$ , and solid lines, dashed lines and dash-dotted lines, for $E_i=0.01\text{eV}$ , $3\times 10^{-3}\text{eV}$ and $10^{-5}\text{eV}$ , respectively. . . .	86
5.2	A schematic of the lattice structure of solid $\alpha$ -O <sub>2</sub> .[70] . . . . .	87
5.3	The dispersion relation of magnons in solid $\alpha$ -O <sub>2</sub> ((5.9)): Note the presence of one acoustic and one optical mode. The dispersion relations are plotted for momentum transfer along three principle axes, (1,0,0), (0,1,0) and (0,0,1). Different periodicities originate from different lattice constants on those axes. Momentum transfers along a non-symmetrical direction introduce a non-periodic dispersion relation, which is illustrated by (1,1,1). Intersections with the parabolic free neutron dispersion set the condition for UCN production. . . . .	88
5.4	The density of states of solid $\alpha$ -O <sub>2</sub> lattice excitations: The dark and light histogram represents the magnon density of states for acoustic and optical branch, respectively. . . . .	89

5.5	Neutron scattering law $\mathcal{S}(\kappa, \omega)$ of a 5K solid $\alpha$ -O <sub>2</sub> : $\mathcal{S}(\kappa, \omega)$ is plotted as a function of the energy transfer $\omega$ for momentum transfer $Q=0.1, 0.3, 0.5, 2.1, 4.1$ and $6.1 \text{ \AA}^{-1}$ . Distinct energy dependences are shown for $\omega > 0$ downscattering and $\omega < 0$ upscattering parts. At low $\kappa$ 's, there exists two dominant contributions at 0.7 meV and 3 meV, which correspond to the self-energy of the acoustic and optical modes, respectively. As $\kappa$ increases, the significance shifts to a high energy peak centered at 10meV, which is clearly the BZ boundary energy. . . . .	90
5.6	The total cross-section(Eq.(5.5)) for a neutron scattering from a solid $\alpha$ -O <sub>2</sub> at temperatures of 1K, 2K, 3K and 5K with an exchange of a single magnon, compared with neutron-phonon scattering(dashed curve) and nuclear absorption cross-section per <sup>16</sup> O <sub>2</sub> molecule(dotted curve). The circled curve at the high incident neutron energy shows the neutron downscattering cross-section via the creation of single magnon, which is nearly temperature independent. The solid curves represent UCN-magnon upscattering cross-sections at various solid temperatures. . . . .	92
5.7	UCN density vs. temperature of incident cold neutron flux with Maxwell-Boltzmann spectrum. The UCN production in S-O <sub>2</sub> peaks with cold neutrons at 12K, whereas in S-D <sub>2</sub> the UCN production is optimized using cold neutron flux with a higher temperature of 30K. . . . .	95
5.8	UCN lifetime run with S-O <sub>2</sub> . . . . .	96
6.1	An electrical diagram of the lumped LC circuit in a bird cage resonator. . .	101
6.2	A schematic of a 16-rung bird cage resonator and a current distribution when driven in the fundamental resonant mode. . . . .	103
6.3	A picture of the bird cage resonator. . . . .	104
6.4	The frequency spectrum of the bird cage resonator. . . . .	105



6.5	The transverse field profile of the bird cage resonator. The resonance frequency is 27.4 MHz. Blue and green curves are data sets with input power of 0.3W and 3.6W, respectively. One edge of the resonator is set at the origin.	106
6.6	A measurement of RF field strength inside the shielding. The metal shield has an O.D. of 14 cm and wall thickness of 0.625 cm. The presence of the shield shifts the resonance frequency from 27.4 MHz to 33.9 MHz. The input power in the resonator is 0.3 W.	107
6.7	A schematic of the experimental setup at ILL.	109
6.8	UCN counts in the PNPI detector with 40 seconds of AFP spin flipper on. The green curve is with the spin flipper operated at 50% of the power of that in the red curve.	112
6.9	UCN counts in the PNPI detector with different AFP on times. Time of trapping for the red, green and blue data sets are 10, 20 and 40 seconds, respectively.	113
6.10	The efficiency dependence on the parameter $n$ and $A$ . The efficiency $\epsilon$ for the solid, dash-dotted and dashed curves are 0.97, 0.99 and 0.996, respectively.	115
C.1	A schematic of scattering vectors in a coherent process.	138
C.2	A schematic of different crystal parameters. (a) Small lattice constant $\tau \ll k^*$ . (b) lattice constant $\tau < q_\Theta$ . (c) Large lattice constant $\tau > 2q_\Theta$ .	139
C.3	Validity of incoherent approximation.	142
D.1	Frequency distribution of polyethylene used for the scattering kernel.	145
D.2	Sub-thermal region of the frequency distribution for polyethylene.	145
D.3	Total neutron scattering cross section from room temperature polyethylene, calculated using the density of states presented in Fig.D.1	146
D.4	Double differential cross sections for 232 meV incident neutron at 25, 60 and 90 degree scattering off of room temperature(296K) polyethylene.	148

D.5	Calculated neutron elastic scattering cross section for polyethylene temperatures of 296, 77 and 4 K. Also shown are the Debye-Waller coefficients at each temperature. (See Eq.( D.4).)	149
D.6	The calculated neutron inelastic scattering cross section for polyethylene temperatures of 296, 77 and 4 K.	150
D.7	The calculated differential cross section for scattering of a 10 meV (116 K) neutron from polyethylene at 296 K, 77K and 4K.	151
E.1	LANSCCE accelerator facility.	154
E.2	Proton beam structure.	155
F.1	A decomposition of the bird cage resonator into current loops. The direction of the magnetic field from each loop is also specified.	158
F.2	The field generated by the rungs (subplot <b>a</b> ) and the end rings (subplot <b>b</b> ). In subplot <b>b</b> is plotted field profiles of end rings of zero radius wire (dashed curve) and flat conducting tape of width 2 cm (solid curve).	160
F.3	Comparison of the field profiles generated by two geometry of the end rings. The default dimension of the resonator is $L = 19.5$ cm, $R = 5$ cm and $W = 2$ cm. <b>a</b> . The length of the resonator is 5 cm, 19.5 cm and 50 cm for the three curves plotted. <b>b</b> . The radius of the resonator is 2 cm, 5 cm and 10 cm for the solid, dashed and dash-dotted curve, respectively.	161
F.4	Field under the shielding. The metal shield has a radius of 7 cm and 15 cm in subplot <b>a</b> and <b>b</b> , respectively. The bird cage resonator has a radius of 5 cm, length of 19.5 cm, and 2 cm wide end rings.	163

# List of Tables

3.1	Ortho/para conversion with different parameters. The listed pressure readings are in mbar. The para-D <sub>2</sub> fraction is measured with Raman spectroscopy using the double grating spectrometer. The spectra are shown in Fig.3.9. . . . .	51
4.1	The critical velocity of different material used for the UCN guide.[27] . . . .	62
6.1	The scheme of the AFP spin flipping experiment. The time order of events follows the increment of the rows. The trap region is divided into $V_1$ and $V_2$ by the position of the AFP spin flipper. . . . .	111
6.2	Measurements of the spin flip efficiency with different time of trapping (AFP on). The numbers under $N_2$ and $N_3$ are the peak counts minus the background counts. . . . .	114
7.1	Candidates for a superthermal source[27]. . . . .	121
B.1	The intrinsic scattering cross-sections $\mathcal{S}_{JJ'}$ associated with different rotational transitions [93]. . . . .	132